Doctoral Dissertation

Characterization and Utilization of Perovskite as Advanced Anode Materials for Solid Oxide Fuel Cells

Ohhun Kwon

Department of Energy Engineering
(Energy Engineering)

Graduate School of UNIST

2020

Characterization and Utilization of Perovskite as Advanced Anode Materials for Solid Oxide Fuel Cells

Ohhun Kwon

Department of Energy Engineering
(Energy Engineering)

Graduate School of UNIST

Characterization and Utilization of Perovskite as Advanced Anode Materials for Solid Oxide Fuel Cells

A dissertation
submitted to the Graduate School of UNIST
in partial fulfillment of the
requirements for the degree of
Doctor of Philosophy

Ohhun Kwon

12/05/2019
Approved by

_____

Advisor
Guntae Kim

Characterization and Utilization of Perovskite as Advanced Anode Materials for Solid Oxide Fuel Cells

Ohhun Kwon

This certifies that the dissertation of Ohhun Kwon is approved.

12/05/2019

_____

Advisor: Guntae Kim

_____

Sang-Young Lee

_____

Jong-Beom Baek

_____

Hu Young Jeong

_____

Jeong Woo Han

Abstract

With increasing energy demand and growing interest in environmental issues, the demand for renewable and clean energy devices such as fuel cells, solar cells, geothermal generators, and wind generators is increasing. Among the renewable energy conversion devices, solid oxide fuel cells (SOFCs) have been considered as promising electrochemical energy conversion devices because of their low environmental pollution, high energy conversion efficiencies, and excellent fuel flexibility. However, a composite of nickel metal and yttria-stabilized zirconia (YSZ), which is commonly used as SOFC anode, is less stable in direct hydrocarbon fuels due to carbon coking and sulfur poisoning on the anode surface. Therefore, the development of advanced anode materials with high tolerance to carbon coking and sulfur poisoning is required to use hydrocarbon fuels directly.

In this regard, the integration of functional catalyst nanoparticles with perovskite oxide supports has been extensively researched as an alternative anode material. The composite materials can be prepared by conventional deposition methods such as chemical vapor deposition and infiltration. Although these techniques are used widely, the materials prepared by the conventional deposition methods suffer from agglomeration and coarsening of the nanoparticles in the SOFC operating conditions due to weak bonding strength between the catalyst nanoparticles and the perovskite supports, which causes severe performance degradation. To overcome these problems, *in-situ* fabrication of catalysts on the anode surface has been received extensive attention. With a purpose to enhance the stability and the electrochemical performance in the hydrocarbon fuels, this dissertation focuses on the understanding and utilization of perovskites for the development of advanced anode materials. A brief overview of the dissertation follows.

1. Characterization and utilization of exsolution on the $PrBaMn_2O_{5+\delta}$ layered double perovskite to improve the catalytic activity of the SOFC anode material
2. Design self-assembled alloy nanoparticles on the anode surface for direct hydrocarbon utilization in the SOFC and dry reforming of methane.
3. Preparation by selective exsolution through topotactic ion exchange to increase the number of exsolved nanoparticles.
4. *In-situ* surface modification of NiO-YSZ anode with $BaZrO_3$ for enhancing the sulfur tolerance of the conventional NiO-YSZ anode.

Contents

List of Figures

power densities of the $PrBaMn_{1.7}Co_{0.3}O_{5-\delta}$ (L-PBMCO) and $PrBaMn_{1.7}Ni_{0.3}O_{5-\delta}$ (L-PBMNO) electrode using C_3H_8 as fuel and ambient air as the oxidant at 800 °C. (c) Electrochemical performances of L-PBMNO anode in C_3H_8 at 700 °C under a constant voltage of 0.6V. (d) Comparison of the maximum power density at 800 °C in H_2 of the present work and other studies in the literature[31-37].

Figure 2.16. (a) I-V curve and the corresponding power densities of the L-PBMCO and L-PBMNO electrode using C_3H_8 as fuel and ambient air as the oxidant at 800 °C. Electrochemical performances of L-PBMNO anode in (b) H_2 and (c) C_3H_8 at 700 °C under a constant voltage of 0.6 V.

Figure 3.1 Schematic illustration for DFT-calculated energetics at each elementary step. (a) The alloy segregation energy was defined by the total energy difference between the systems with Co-O_v-Ni alloy located at surface and in bulk. (b) To compare the segregation energy of Co-O_v-Ni alloy with the separate segregation of Co-O_v-Co and Ni-O_v-Ni, we used the normalized segregation energies of Co-O_v-Co and Ni-O_v-Ni. The alloy formation energies (c) in the bulk and (d) at the surface were defined by the total energy difference between the systems where two different B-site metals are separated and aggregated. (e) The oxygen vacancy formation energy was defined by total energy difference of the supercells with and without an oxygen vacancy.

Figure 3.2. X-ray diffraction patterns of (a) $Pr_{0.5}Ba_{0.5}Mn_{0.85}Co_{0.05}Ni_{0.1}O_3$ sintered at 950 °C for 4h in air and (b) PBMCNO after reduction at 850 °C for 4h in humidified (3% H_2O) H_2. Scanning electron microscope images of (c) $Pr_{0.5}Ba_{0.5}Mn_{0.85}Co_{0.05}Ni_{0.1}O_3$ and (d) PBMCNO; scale bar 400 nm. In the SEM image of PBMCNO, the black triangles indicate the exsolved nanoparticles.

Figure 3.3. Transmission electron microscopy analysis. (a) High-angle annular dark-field (HAADF) image of the PBMCNO with the EDS elemental map of Pr, Ba, Mn, Co, Ni, and O; scale bar 100 nm. (b) A bright-field (BF) TEM image; scale bar, 50 nm and (c) high-resolution (HR) TEM image of PBMCNO; scale bar 10 nm. (d) Magnified HR TEM image of exsolved Co-Ni alloy nanoparticle; scale bar 1 nm.

Figure 3.4. High-angle annular dark-field (HADDF) image of the $PrBaMn_{1.7}Co_{0.1}Fe_{0.2}O_{5+}$ with the EDS elemental map of Pr, Ba, Mn, Co, Fe, and O; scale bar 25 nm.

Figure 3.5. Schematic illustrations and energetics of (a) bulk alloy formation and (b) surface alloy formation for the exsolution of alloy nanoparticles. (c) In situ XRD patterns of PBMCNO in humidified (3% H_2O) H_2 at various temperatures. (d) Optimized alloy structures of Co_3Ni, CoNi, and $CoNi_3$ that we used for DFT calculations in this study.

Figure 3.6. Oxygen vacancy formation energies (a)-(c) at the surface or (d)-(f) in the bulk of Co, Ni, and Co-Ni doped PBMO, respectively. Pr, Ba, Mn, Co, Ni, and O atoms are shown as dark blue, green, purple, blue, grey, and red, respectively. The Ov in red rectangular indicates an oxygen vacancy.

List of Tables

Chapter 1. Introduction

1.1 Motivation and Research Objective

With the exponential growth in energy consumption and the limitation of fossil fuels, interest in environmentally friendly energy is increasing.[1–4] Among the renewable energy conversion devices, a fuel cell has been received much attention as promising energy conversion devices because it exhibits fuel flexibility, high energy conversion efficiency, and zero emissions of greenhouse gases. In principle, fuel cells convert chemical energy directly into electrical energy without undesirable products such as NO_x, SO_x, and particulate emissions. As shown in table 1.1, fuel cells are classified as proton exchange membrane fuel cell (PEMFC)[5–7], phosphoric acid fuel cell (PAFC)[8,9], molten carbonate fuel cell (MCFC)[10,11], and solid oxide fuel cell (SOFC)[12,13] depending on their operating temperatures and electrolyte materials. Among all types of fuel cells, SOFCs provide the highest energy conversion efficiency and the utilization of various fuels such as hydrogen, natural gas, biogas, syngas, and coal gas.

In order to utilize the variety of fuels in SOFC, the optimization of an anode material directly affected by the fuels are important. The conventional SOFC anode, Ni-YSZ, has high electrochemical performance when hydrogen is used as fuel but it is deactivated in hydrocarbon fuels due to carbon coking and sulfur poisoning.[14,15] To overcome the stability problems, research on the development of alternative anode materials has been actively conducted. In this regard, alternative anode materials for the SOFC should satisfy three major requirements. First, the materials should have high electronic and ionic conductivity in a reducing atmosphere. Second, the materials should have good mechanical and chemical compatibility with an electrolyte material under the anode operating conditions. Third, the materials should be stable in a hydrocarbon atmosphere that can cause carbon coking and sulfur poisoning. However, it is difficult to find the materials with both high catalytic properties and stability. Therefore, the development of alternative materials for the SOFC anode is challenging.

The major research objective of the dissertation is to develop an advanced perovskite anode and to obtain a fundamental understanding of exsolution in layered double perovskite.

Chapter 1 provides the theoretical backgrounds of the SOFC and introduces various SOFC anode materials.

In chapter 2, exsolution trends on the $PrBaMn_2O_{5+\delta}$ were investigated to design the SOFC anode material with excellent catalytic activity.

In chapter 3, self-assembled alloy nanoparticle on the $PrBaMn_2O_{5+\delta}$ was reported to enhance the catalytic activity for fuel oxidation in the SOFC and dry reforming of methane.

In chapter 4, the preparation by selective exsolution through topotactic ion exchange was reported to increase the number of exsolved nanoparticles.

In chapter 5, $BaZrO_3$ modified NiO-YSZ anode supported cell was reported to enhance sulfur tolerance of the conventional NiO-YSZ anode.

Type	PEMFC	PAFC	MCFC	SOFC
Electrolyte	Polymer	Phosphoric acid	Molten carbonate	Ceramic
Operating temperature	<100 ºC	<200 ºC	~650 ºC	500~1000 ºC
Catalyst Price	Pt	Pt	NiO	NiO
Efficiency	35 ~ 40 %	35 ~ 42 %	45 ~ 50 %	45 ~ 65 % (CHP*: >85 %)

Table 1.1. Type of fuel cells. *CHP (Combining heat-power)

1.2 Solid Oxide Fuel Cell (SOFC)

A solid oxide fuel cell (SOFC) is an electrochemical device that converts the chemical energy of fuel directly into electrical energy. The SOFC operates at high temperatures over 500 ºC, allowing the use of inexpensive metal oxides or metals as a catalyst instead of expensive metal such as noble metals. As shown in Figure 1.1, the SOFC consists of three major components including the electrolyte, the cathode, and the anode. The solid electrolyte blocks gas diffusion between the electrodes and it is ionically conductive but electronically insulating. Meanwhile, to be used as an electrolyte material, it must be stable in a redox atmosphere and chemically and physically compatible with the electrode materials.

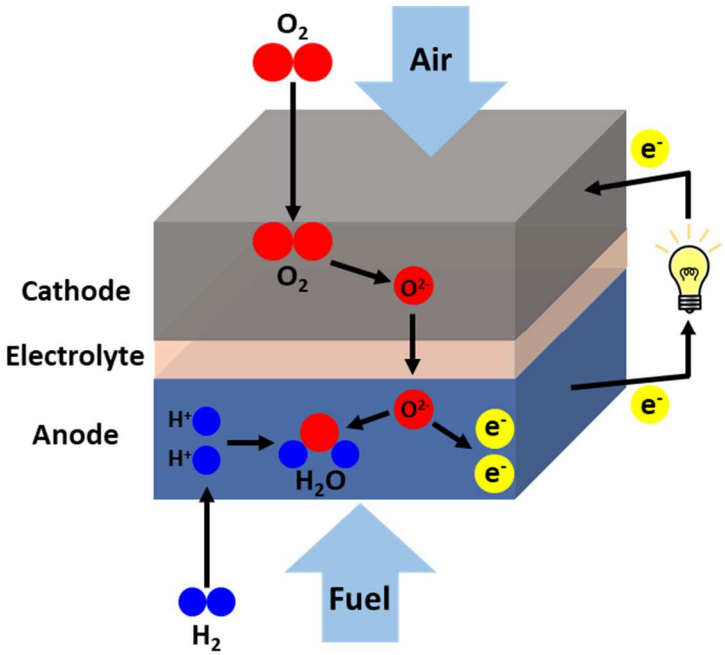

Figure 1.1. Schematic diagram of solid oxide fuel cell

In the SOFC operating environment, the cathode exposed to air undergoes the oxidizing condition, while the anode exposed to fuel withstands the highly reducing atmosphere. Thus, the SOFCs are mainly driven by the chemical potential difference between two atmospheres.

In detail, oxygen ions (O^{2-}) are produced by oxygen reduction reaction (ORR) at the cathode as expressed in equation 1.1.

$$\frac{1}{2}O_2 + 2e^- \rightarrow O^{2-} \quad (1.1)$$

The generated oxygen ions move to the anode through the oxygen ion conducting dense electrolyte. At the anode, the oxygen ions participate in the hydrogen oxidation reaction (HOR), which generates water and electrons as in equation 1.2.

$$H_2 + O^{2-} \rightarrow H_2O + 2e^- \quad (1.2)$$

Both ORR and HOR reactions occur at the triple-phase boundary (TPB) of electronic phase (e^-), ionic phase (O^{2-}), and gas phase (H_2/O_2) as shown in Figure 1.2.

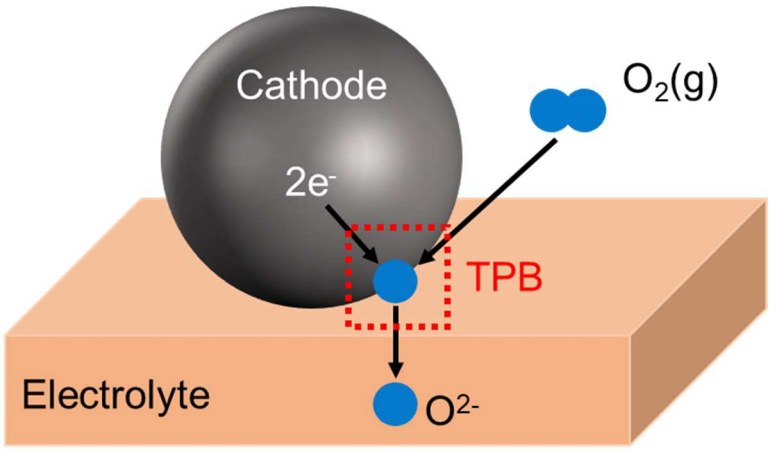

Figure 1.2. Schematic diagram of the oxygen reduction reaction at triple phase boundary (TPB)

Furthermore, Adler *et al.* summaries a continuum model of the ORR mechanism at a porous mixed ionic-electronic conductor.[16] As shown in Figure 1.3 (a), reduction of the oxygen molecule (gas phase) occurs at the interface between MIEC and gas phases, and then, the oxygen ion diffuses through the MIEC by solid state diffusion. The chemical exchange of oxygen at the interface between gas and mixed conductor was considered as a non-charge transfer process.

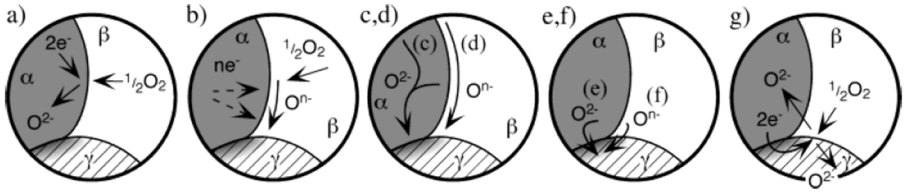

Figure 1.3. Some mechanisms thought to govern oxygen reduction in SOFC cathodes. Phases α, β, and γ refer to the electronic phase, gas phase, and ionic phase, respectively: (a) Incorporation of oxygen into the bulk of the electronic phase (if mixed conducting); (b) adsorption and/or partial reduction of oxygen on the surface of the electronic phase; (c) bulk or (d) surface transport of O^{2-} or O^{n-}, respectively, to the α/γ interface, (e) Electrochemical charge transfer of O^{2-} or (f) combinations of O^{n-} and e^-, respectively, across the α/γ interface, and (g) rates of one or more of these mechanisms wherein the electrolyte itself is active for generation and transport of electroactive oxygen species.[16]

1.3 Theoretical Background

1.3.1 Thermodynamic of SOFC

In the SOFC, the Gibbs free enthalpy of the combustion reaction by fuel and oxygen is directly converted into electricity. The first and the second law of thermodynamics provide the description of a reversible fuel cell. The first law of the thermodynamics presents in equation (1.3).[17]

$$q + w = \Delta H \tag{1.3}$$

The molar reaction enthalpy (ΔH) of the oxidation is comprised of work and heat energy. The second law of thermodynamics governs the reversibility of the transport processes and applies to reversible processes yields

$$\oint \Delta S = 0 \;\rightarrow\; q = q_{rev} = T\Delta S \tag{1.4}$$

We can rewrite as equation 1.5 because the reversible heat exchange with the environment equalizes the generated reaction entropy,

$$q_{rev} + w_{rev} = \Delta H \tag{1.5}$$

The reaction entropy is a result of the different opportunities of the species to save thermal energy between the absolute zero level of temperature and temperature level of the reactor.

Equations (1.4) and (1.5) provide the molar reversible work, w_{rev}

$$w_{rev} = \Delta H - T\Delta S \tag{1.6}$$

The reversible work of the reaction is identical with the Gibbs free energy of the reaction with the ambient temperature as a reference for the calculation of the Gibbs free energy.

$$w_{rev} = \Delta G = \Delta H - T\Delta S \tag{1.7}$$

Thermodynamic potentials can be used to identify the energy transfer from one form to another on the basis of the first and second laws of thermodynamics. Using the first and second law of thermodynamics, internal energy can be described by the variation of two independent variables of entropy (*S*) and volume (*V*) where *p* is the pressure and *T* is the temperature.[18]

$$dU = TdS - pdV \tag{1.8}$$

In equation 1.8, TdS is the reversible heat transfer and pdV represents the mechanical work. The following equations present how the dependent variables (*T* and *p*) are related to variations in the independent variables (*S* and *V*):

$$(\frac{dU}{dS})_V = T \tag{1.9}$$

$$(\frac{dU}{dV})_S = -p \tag{1.10}$$

U can be rewritten by a Legendre transform with defining the new thermodynamic potential *G* (*T*, *p*) as follows:

$$G = U - (\frac{dU}{dS})_V S - (\frac{dU}{dV})_S V \tag{1.11}$$

From equation (1.9) and equation (1.10), we obtain

$$G = U - TS + pV \tag{1.12}$$

The variation of *G* results in

$$dG = dU - TdS - SdT + pdV + Vdp \tag{1.13}$$

Since $dU = T\,dS - p\,dV$,

$$dG = -SdT + Vdp \tag{1.14}$$

Similar to equation (1.11), the new thermodynamic potential *H* can be described as

$$H = U - (\frac{dU}{dV})_S V \quad (1.15)$$

From equation (1.10), we get

$$H = U + pV \quad (1.16)$$

Where *H* stands for enthalpy. Through differentiation, *H* is defined as a function of *S* and *p*:

$$dH = dU + pdV + Vdp \quad (1.17)$$

$$dH = TdS + Vdp \quad (1.18)$$

The overall reaction of SOFCs presents as follow:

$$H_2 + \frac{1}{2}O_2 \rightarrow H_2O \quad (1.19)$$

the difference of Gibbs free energy (ΔG) can be written as

$$\Delta G = \Delta G_{H_2O} - \Delta G_{H_2} - \frac{1}{2}\Delta G_{O_2} \quad (1.20)$$

Assume all the Gibbs free energy is consumed to electrical work, then

$$\Delta G = -nFE \quad (1.21)$$

where *n*, *F*, and *E* indicate the number of electrons involved in the chemical reaction and the Faraday constant, and the reversible potential, respectively. The reversible standard potential (E^0) of the electrochemical reaction can be defined as equation 1.24 when the reactants and products are all in their standard states,[19]

$$E^0 = -\frac{\Delta G^0}{nF} \quad (1.22)$$

Here, the Gibbs free energy is dependent on the temperature by the relation

$$\Delta G = \Delta H - T\,\Delta S \quad (1.23)$$

Substitute the standard condition values of T = 273.15 K, p = 1 atm into equation (1.22),

$$E^0 = \frac{2379000\ J\ mol^{-1}}{2\times 96485\ C\ mol^{-1}} = 1.23\ \text{V} \quad (1.24)$$

The theoretical reversible potential (E_{th}) is derived by the Nernst equation,

$$E_{th} = E^0 - (\frac{RT}{2F}) \ln\left(\frac{P_{H_2O}}{P_{H_2} P_{O_2}^{\frac{1}{2}}}\right) \quad (1.25)$$

where *R* is the gas constant, *T* is the absolute temperature, and *p* is the partial pressure of each gas.

1.3.2 Electrochemical performance of SOFC

The performance of SOFC can be represented by a graph of current-voltage characteristics. An ideal SOFC would maintain a constant voltage determined by thermodynamics while applying any amount of current. However, the actual cell potential decreases from its ideal cell potential due to irreversible losses as shown in Figure 1.4. This reduction in actual cell voltage is affected by various factors such as electrode microstructure, electrolyte thickness, operating temperature, and gas flow rate. The difference between the theoretical potential and actual cell potential can be defined as polarization loss. These factors consist of three contributions. There are several types of polarization losses in fuel cell systems and consists of three contributions: activation, ohmic, and concentration polarization.[20]

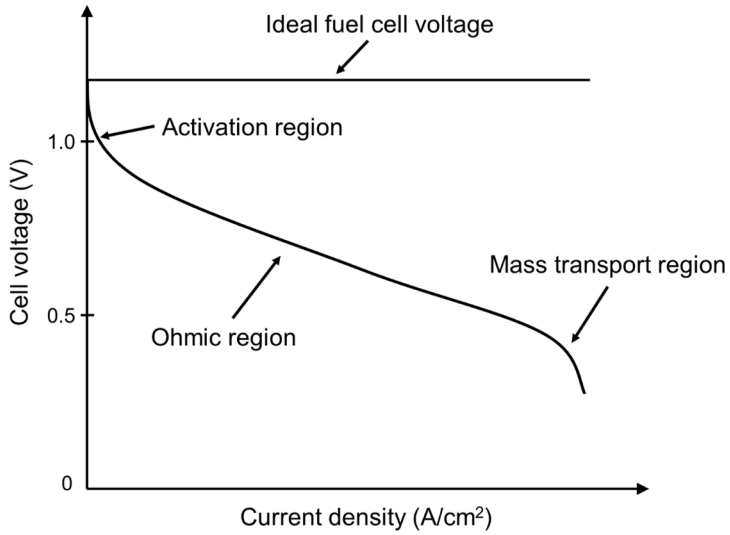

Figure 1.4. The graph of fuel cell *i-V* curve

■ **Activation polarization**

Activation polarization is directly related to the rate-determining step, charge transfer or surface exchange reaction at the electrode. The activation polarization can be explained by the over-potential consumed to supply the activation energy for the electrode reactions. The relationship between activation polarization and current density can be expressed by the Butler-Volmer equation as

$$i = i_0 \left[e^{\frac{(1-\alpha)nF\eta_{act}}{RT}} - e^{-\frac{-\alpha nF\eta_{act}}{RT}} \right] \quad (1.26)$$

where i is the current density, i_0 is the exchange current density, α is the charge transfer coefficient, and η_{act} is the activation polarization.

In equation 1.26, One of the terms in the parentheses can be ignored for large values of η, and then the equation 1.26 can be described as the Tafel equation

$$\eta_{act} = a \pm b \log i \quad (1.27)$$

Parameters a and b are constants associated with the applied electrode material, electrode reaction type, and temperature.

- **Ohmic polarization**

Resistance to electron flow through the electrode and ion flow in the electrolyte causes ohmic loss. The dominant ohmic loss through the electrolyte can be reduced by reducing electrode separation and increasing the ion conductivity of the electrolyte.

- **Concentration polarization**

As a reactant is consumed at the electrode during the electrochemical reaction, a loss of potential occurs owing to the incapability of the surrounding material to retain the initial concentration of the bulk fluid. This is how concentration gradients are obtained. Various processes may contribute 1) slow diffusion in the gas phase within the electrode pores, 2) solution/dissolution of reactants/products into and out of the electrolyte, or 3) diffusion of reactants and products into the electrochemical reaction through the electrolyte. At practical current densities, slow transport of reactants and products to/from electrochemical reaction sites is a major cause of concentration polarization.

1.4 Anode Materials for SOFC

Conventional SOFCs use hydrogen as fuel obtained through external reforming which causes the reduction of efficiency by ~20%. Above all, the hydrogen is expensive to transport and store and lacks infrastructure. In order to solve these problems, hydrocarbons should be used directly as fuel in the SOFC system.[21–23] Direct hydrocarbon SOFCs can use existing infrastructure and reduce additional processes such as reforming and purification. In this context, the optimization of anode materials affected by the fuel is necessary for the direct use of hydrocarbon as fuel. Material selection for SOFC anodes is determined by a number of factors. First, sufficient electrical conductivity is required in the reducing atmosphere to transfer electrons from the anode material to the external circuit. Second, the anode material should have catalytic activity for fuel oxidation. Third, the anode material should have a high tolerance to carbon coking and sulfur tolerance in hydrocarbon fuels.

1.4.1 Conventional anode in SOFC

In the conventional SOFCs, Ni-YSZ cermet is used as the anode material because of its high electrical conductivity in reducing atmosphere, excellent catalytic activity for fuel oxidation, and low cost. However, when the hydrocarbon is directly used as fuel, the Ni-YSZ anode is deactivated by the carbon coking of Ni.[1,24,25] As shown in Figure 1.5, an excessive amount of carbon fiber is formed on the surface of electrode due to the high reactivity between Ni and carbon, which reduces the catalytic activity of Ni-YSZ anode. Meanwhile, the sulfur poisoning is also stability issue when using hydrocarbon fuels. Reformed hydrocarbon fuels possess a hydrogen sulfide (H_2S) that deactivates the Ni-YSZ anode even in parts per million (ppm) levels.[14,26] Under SOFC operating conditions, the sulfur adsorbs on the Ni surface, which hinders the electrochemically active sites and results in a degradation of performance. Therefore, in order to replace the conventional Ni-YSZ anode, it is necessary to develop an alternative anode material having a high tolerance to carbon coking and sulfur poisoning.

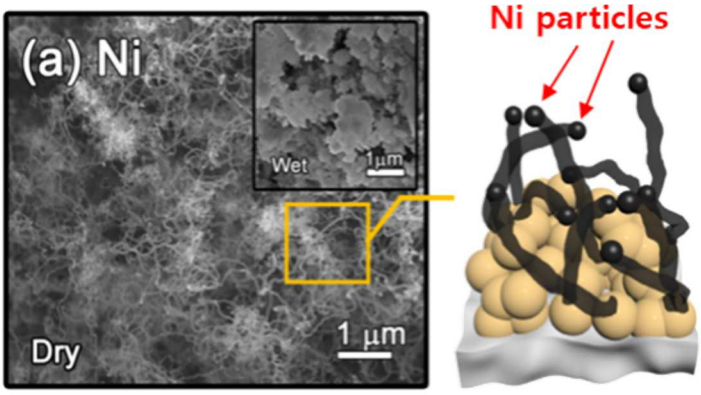

Figure 1.5. Scanning electron microscopy image and schematic illustration of carbon coking in Ni[27]

1.4.2 Ceramic anode materials

The development of Ni-free ceramic anode materials has been conducted due to the drawbacks of Ni-based cermet anodes in the utilization of direct hydrocarbon fuels. In early studies, ceramic anodes presented high tolerance to carbon coking and sulfur poisoning but low electronic conductivity under reducing conditions. To improve the electrochemical performance, perovskite-based anode materials with mixed oxide-ion and electron conductors (MIECs) have been explored.[28–31] The perovskite structures have a general formula of ABO_3, where A is alkaline earth or rare-earth elements and B is transition metal elements, and O is oxygen. As shown in Figure 1.6, the coordination numbers of A-site and B-site are 12 and 6, respectively, in the cubic perovskite structure. The perovskite structure can accommodate a variety of dopants in the A- and B-sites due to its excellent compositional and structural flexibility. By doping with lower valance cations on the A or B sites, oxygen vacancies are formed in the perovskite lattice to match the charge neutrality, which provides pathways for oxygen ion transport. In addition, the B-site transition metal cations have multi-valence states depending on the atmospheres, exhibiting high electronic conductivity.

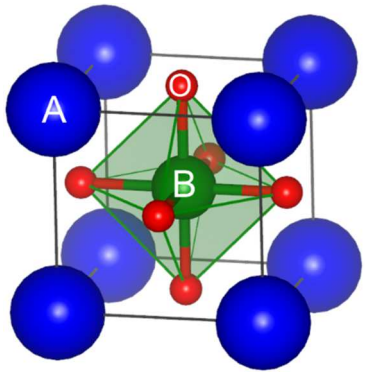

Figure 1.6. Unit cell of the cubic perovskite structure.

Based on the attractive characteristics of the perovskites, various perovskites such as Sr_2MgMoO_6 (SMMO), $La_{0.8}Sr_{0.2}Sc_xMn_{1-x}O_{3-\delta}$, $La_{0.33}Sr_{0.67}Ti_xMn_{1-x}O_{3-\delta}$, and $Pr_{0.8}Sr_{1.2}(Co, Fe)_{0.8}Nb_{0.2}O_4$ (K-PSCFN) have been proposed as an anode material to replace the conventional SOFCs anode.[32–35] These anode materials showed stable performance in anodic operating conditions but electrochemical performances of the anodes were still lower than those of conventional Ni-YSZ anode. Recently, Sengodan *et al.* reported a new layered double perovskite structure, $PrBaMn_2O_{5+\delta}$ (PBMO), to obtain both high stability and excellent electrochemical performance.[36] As shown in Figure 1.7, the layered perovskite has a structural formula of $AA`B_2O_{5+\delta}$ with a stacking sequence of [A`O]-[$BO_2$]-[$AO_\delta$]-[$BO_2$], where A is lanthanide elements and A` is alkaline earth and B is transition metal elements, and O is oxygen.[37–39] It is well noted that most oxygen vacancies are located on AO layer, improving the mobility of oxygen ion. Therefore, the layered double perovskite exhibits excellent catalytic properties

such as fast surface oxygen exchange and oxygen ion diffusion because of its oxygen vacancy channel. Moreover, the electrical conductivity of PBMO (8.16 S cm^{-1}) was higher than that of previous ceramic anodes such as SMMO (4.21 S cm^{-1}) and $La_{0.75}Sr_{0.25}Cr_{0.5}Mn_{0.5}O_3$ (0.96 S cm^{-1}) at 800 ºC in 5% H_2. And the PBMO showed excellent SOFC anode performance in various fuels such as H_2, H_2-50 ppm H_2S, C_3H_8, and CH_4 (Figure 1.8. a and b). Especially, no degradations were observed in both sulfur poisoning fuel and hydrocarbon fuel (Figure 1.8. c and d).

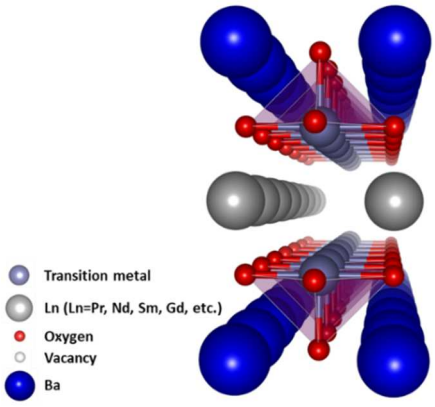

Figure 1.7. The unit cell of the layered double perovskite structure.

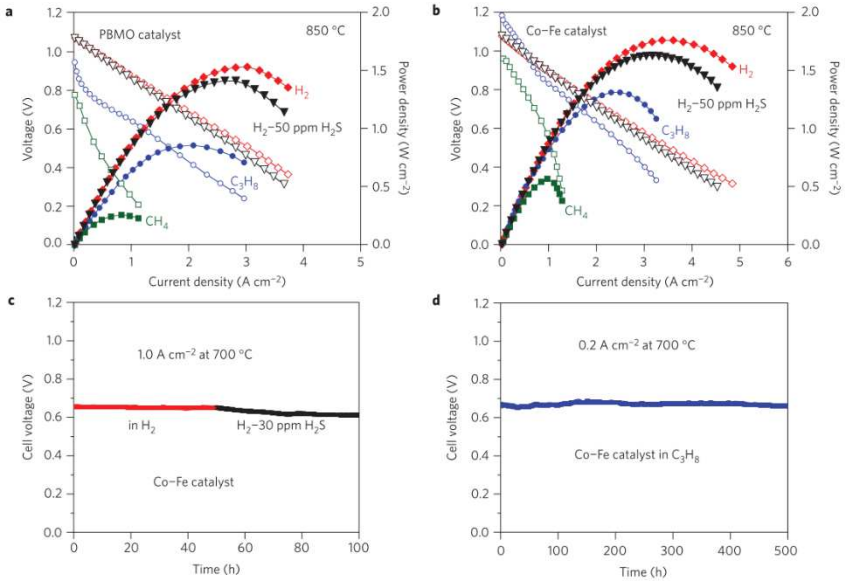

Figure 1.8. *I-V* curves and the corresponding power densities of the layered PBMO anode with (a) layered PBMO catalyst and (b) Co–Fe catalyst using different humidified (3% H_2O) fuels and ambient air as the oxidant at 850 ºC. (c) Electrochemical performance for a layered PBMO with Co–Fe catalyst under a constant current load of 1.0 A cm^{-2} at 700 ºC in H_2 and H_2–30ppm H_2S. (d) Electrochemical performance of layered PBMO with Co–Fe catalyst under a constant current load of 0.2 A cm^{-2} at 700 ºC in C_3H_8.[36]

1.4.3 Exsolution in the Perovskite

Composite materials consisting of catalytic nanoparticles and perovskite oxide supports have been mainly utilized as ceramic electrodes for SOFCs due to their multi-functional properties.[27, 40, 41] Generally, the composite materials are prepared by depositing catalytic nanoparticles on the surface of the perovskite support via chemical vapor deposition (CVD) and infiltration methods.[42–44] Although these composite materials present high electrochemical performance, the materials fabricated by the conventional deposition methods undergo agglomeration and coarsening of the catalytic nanoparticles in the SOFC operating conditions, resulting in significant performance degradation. To overcome these problems, exsolution has been adopted as a new strategy for designing composite materials.[45–48]

The exsolution is a phenomenon in which the metal catalysts in the perovskite oxide lattice exsolve to the oxide surface in a reducing atmosphere.[49] This process is time-efficient because there is no additional process for catalyst addition. Moreover, the exsolved metal nanoparticles are socketed on the oxide surface, improving cohesion between the metal and the support.[50] As shown in Figure 1.9, tip growth and base growth of carbon fiber in the hydrocarbon atmosphere occur from the conventional deposition method and exsolution, respectively. In the tip growth of carbon fiber, the Ni catalyst detaches from the oxide support, reducing the electrochemically active site. In the base growth, exsolved Ni metal has a high carbon coking tolerance because Ni is strongly attached to oxide support. Therefore, even and stable catalysts can be formed on the surface through the exsolution process. The key requirements to utilize the exsolution are the stability of the perovskite oxide support and reducibility of metal catalysts in the reducing atmosphere.

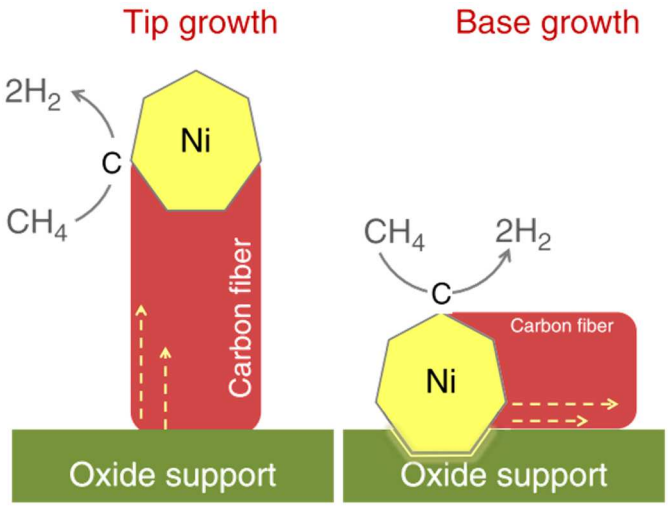

Figure 1.9. Schematic of possible carbon fiber growth mechanisms based on conventional deposition method and exsolution.[50]

To date, single perovskite (ABO_3)[51–55], double perovskite ($A_2B_2O_{5+\delta}$)[56–59] and Ruddlesden Popper (RP, $A_{n+1}B_nO_{3n+1}$)[60–62] based materials have been mainly studied as the support perovskite oxides because it is possible to withstand some lattice mismatch between A-O and B-O bonds, thus allowing doping of different types of cations at each site.[63, 64] Early exsolution research was applied to stoichiometric single perovskite with A/B = 1, where only easily reducible cations (*e.g.*, Ni^{2+}, Ru^{2+}, Rh^{4+}, Pd^{4+}, and Pt^{4+}) could be exsolved to metal nanoparticles.[65] In this case, most cations remain in the bulk, so the number of nanoparticles available on the surface is limited. In addition, undesirable A-site cation was segregated after the exsolution process. Therefore, A-site deficient single perovskite (A/B < 1) has been adopted as a method to solve these problems.[45] In this system, the exsolution of B-site cation causes a more stable defect-free perovskite, inhibiting the segregation of A-site cation. And harder-to-reduce cations also can be exsolved in this condition.

In the double and RP perovskites, phase transitions in the reducing atmosphere lead to exsolution without external processing such as the A-site defect of perovskites. According to the density functional theory (DFT) calculations using the Vienna ab initio simulations package (VASP), the double perovskite structure (-3.62 eV) has a much lower energy barrier for exsolution of B-site cations than the single perovskite (-4.82 eV).[66] That is, the crystal reconstruction from single perovskite to double perovskite is the thermodynamically favorable process for the exsolution. Although the double perovskite has received much attention as support oxide for exsolution, a comprehensive understanding is lacking because of its structural complexity compared to single perovskite. In this regard, the next chapter describes the exsolution trends in the double perovskite based on a fundamental understanding of the double perovskite structure.

References

(1) Atkinson, A.; Barnett, S.; Gorte, R. J.; Irvine, J. T. S.; McEvoy, A. J.; Mogensen, M.; Singhal, S. C.; Vohs, J. Advanced Anodes for High-Temperature Fuel Cells. *Nat Mater* **2004**, *3*, 17–27.

(2) Kim, J.; Jun, A.; Gwon, O.; Yoo, S.; Liu, M.; Shin, J.; Lim, T. H.; Kim, G. Hybrid-Solid Oxide Electrolysis Cell: A New Strategy for Efficient Hydrogen Production. *Nano Energy* **2018**, *44*, 121–126.

(3) Choi, Y.; Cha, S. K.; Ha, H.; Lee, S.; Seo, H. K.; Lee, J. Y.; Kim, H. Y.; Kim, S. O.; Jung, W. C. Unravelling Inherent Electrocatalysis of Mixed-Conducting Oxide Activated by Metal Nanoparticle for Fuel Cell Electrodes. *Nat. Nanotechnol.* **2019**, *14*, 245–251.

(4) Kim, C.; Kim, J.; Joo, S.; Yang, Y.; Shin, J.; Liu, M.; Cho, J.; Kim, G. Highly Efficient CO2 Utilization via Aqueous Zinc– or Aluminum–CO_2 Systems for Hydrogen Gas Evolution and Electricity Production. *Angew. Chemie - Int. Ed.* **2019**, 9506–9511.

(5) Curtin, D. E.; Lousenberg, R. D.; Henry, T. J.; Tangeman, P. C.; Tisack, M. E. Advanced Materials for Improved PEMFC Performance and Life. *J. Power Sources* **2004**, *131*, 41–48.

(6) Sharma, S.; Pollet, B. G. Support Materials for PEMFC and DMFC Electrocatalysts - A Review. *J. Power Sources* **2012**, *208*, 96–119.

(7) Roen, L. M.; Paik, C. H.; Jarvi, T. D. Electrocatalytic Corrosion of Carbon Support in PEMFC Cathodes. *Electrochem. Solid-State Lett.* **2004**, *7*, 19–22.

(8) Choudhury, S. R.; Deshmukh, M. B.; Rengaswamy, R. A Two-Dimensional Steady-State Model for Phosphoric Acid Fuel Cells (PAFC). *J. Power Sources* **2002**, *112*, 137–152.

(9) Stonehart, P. Development of Alloy Electrocatalysts for Phosphoric Acid Fuel Cells (PAFC). *J. Appl. Electrochem.* **1992**, *22*, 995–1001.

(10) Cherepy, N. J.; Krueger, R.; Fiet, K. J.; Jankowski, A. F.; Cooper, J. F. Direct Conversion of Carbon Fuels in a Molten Carbonate Fuel Cell. *J. Electrochem. Soc.* **2005**, *152*, 80–87.

(11) Cavallaro, S.; Mondello, N.; Freni, S. Hydrogen Produced from Ethanol for Internal Reforming Molten Carbonate Fuel Cell. *J. Power Sources* **2001**, *102*, 198–204.

(12) Zhou, W.; Jiao, Y.; Li, S.-D.; Shao, Z. Anodes for Carbon-Fueled Solid Oxide Fuel Cells. *ChemElectroChem* **2016**, *3*, 193–203.

(13) Ge, X. M.; Chan, S. H.; Liu, Q. L.; Sun, Q. Solid Oxide Fuel Cell Anode Materials for Direct Hydrocarbon Utilization. *Adv. Energy Mater.* **2012**, *2*, 1156–1181.

(14) Kwon, O.; Sengodan, S.; Lim, C.; Jeong, H. Y.; Shin, J.; Ju, Y.-W.; Kim, G. In Situ Surface Modification of Ni-YSZ with $BaZrO_3$ for Enhancing the Sulfur Tolerance of Ni-YSZ Anode. *J. Electrochem. Soc.* **2016**, *163*, F1055–F1058.

(15) Liu, M.; Choi, Y.; Yang, L.; Blinn, K.; Qin, W.; Liu, P.; Liu, M. Direct Octane Fuel Cells: A Promising Power for Transportation. *Nano Energy* **2012**, *1*, 448–455.

(16) S. B. Adler, *Chem. Rev.* **2004**, 104, 4791-4843.

(17) R. Bove, S. Ubertini, *Modeling Solid State Fuel Cells: Chapter 2. Thermodynamics of Fuel Cell*, Springer, **2008**.

(18) C. M. A. Brett, A. M. O. Brett, *Electrochemistry: Principles, Methods, and Applications*, Oxford University Press Inc., New York, **1993**.

(19) A. J. Bard, L. R. Faulkner, *Electrochemical Methods: Fundamentals and Applications*, John Wiley & Sons, New York, **2000**

(20) W. G. C. Ryan O'hayre, Suk-Won Cha, *Wiley*, **2016**, 603.

(21) Shin, T. H.; Ida, S.; Ishihara, T. Doped CeO_2-$LaFeO_3$ Composite Oxide as an Active Anode for Direct Hydrocarbon-Type Solid Oxide Fuel Cells. *J. Am. Chem. Soc.* **2011**, *133*, 19399–19407.

(22) Choi, Y.; Brown, E. C.; Haile, S. M.; Jung, W. Electrochemically Modified, Robust Solid Oxide Fuel Cell Anode for Direct-Hydrocarbon Utilization. *Nano Energy* **2016**, *23*, 161–171.

(23) Park, S.; Vohs, J. M.; Gorte, R. J. Direct Oxidation of Hydrocarbons in a Solid-Oxide Fuel Cell. *Nature* **2000**, *404*, 265–267.

(24) Liu, M.; Lynch, M. E.; Blinn, K.; Alamgir, F. M.; Choi, Y. Rational SOFC Material Design: New Advances and Tools. *Mater. Today* **2011**, *14*, 534–546.

(25) Cheng, Z.; Wang, J.-H.; Choi, Y.; Yang, L.; Lin, M. C.; Liu, M. From Ni-YSZ to Sulfur-Tolerant Anode Materials for SOFCs: Electrochemical Behavior, in Situ Characterization, Modeling, and Future Perspectives. *Energy Environ. Sci.* **2011**, *4*, 4380.

(26) Sengodan, S.; Liu, M.; Lim, T.-H.; Shin, J.; Kim, G. Enhancing Sulfur Tolerance of a Ni-YSZ Anode through $BaZr_{0.1}Ce_{0.7}Y_{0.1}Yb_{0.1}O_{3-\delta}$ Infiltration. *J. Electrochem. Soc.* **2014**, *161*, F668–F673.

(27) Kim, S.; Kim, C.; Lee, J. H.; Shin, J.; Lim, T.-H.; Kim, G. Tailoring Ni-Based Catalyst by Alloying with Transition Metals (M=Ni, Co, Cu, and Fe) for Direct Hydrocarbon Utilization of Energy Conversion Devices. *Electrochim. Acta* **2017**, *225*, 399–406.

(28) Choi, S.; Kucharczyk, C. J.; Liang, Y.; Zhang, X.; Takeuchi, I.; Ji, H.-I.; Haile, S. M. Exceptional Power Density and Stability at Intermediate Temperatures in Protonic Ceramic Fuel Cells. *Nat. Energy* **2018**.

(29) Park, J.; Zou, J.; Yoon, H.; Kim, G.; Chung, J. S. Electrochemical Behavior of $Ba_{0.5}Sr_{0.5}Co_{0.2-x}Zn_xFe_{0.8}O_{3-\delta}$ (x = 0–0.2) Perovskite Oxides for the Cathode of Solid Oxide Fuel Cells. *Int. J. Hydrogen Energy* **2011**, *36*, 6184–6193.

(30) Kim, J.; Choi, S.; Jun, A.; Jeong, H. Y.; Shin, J.; Kim, G. Chemically Stable Perovskites as Cathode Materials for Solid Oxide Fuel Cells: La-Doped $Ba_{0.5}Sr_{0.5}Co_{0.8}Fe_{0.2}O_{3-\delta}$. *ChemSusChem* **2014**, *7*, 1669–1675.

(31) Li, Y.; Zhang, W.; Zheng, Y.; Chen, J.; Yu, B.; Chen, Y.; Liu, M. Controlling Cation Segregation in Perovskite-Based Electrodes for High Electro-Catalytic Activity and Durability. *Chem. Soc. Rev.* **2017**.

(32) Huang, Y.-H.; Dass, R. I.; Xing, Z.-L.; Goodenough, J. B. Double Perovskites as Anode Materials for Solid-Oxide Fuel Cells. *Science* **2006**, *312*, 254–257.

(33) Corre, G.; Kim, G.; Cassidy, M.; Vohs, J. M.; Gorte, R. J.; Irvine, J. T. S. Activation and Ripening of Impregnated Manganese Containing Perovskite Sofc Electrodes under Redox Cycling. *Chem. Mater.* **2009**, *21*, 1077–1084.

(34) Sengodan, S.; Yeo, H. J.; Shin, J. Y.; Kim, G. Assessment of Perovskite-Type $La_{0.8}Sr_{0.2}Sc_xMn_{1-x}O_{3-\delta}$ Oxides as Anodes for Intermediate-Temperature Solid Oxide Fuel Cells Using Hydrocarbon Fuels. *J. Power Sources* **2011**, *196*, 3083–3088.

(35) Yang, C.; Yang, Z.; Jin, C.; Xiao, G.; Chen, F.; Han, M. Sulfur-Tolerant Redox-Reversible Anode Material for Direct Hydrocarbon Solid Oxide Fuel Cells. *Adv. Mater.* **2012**, *24*, 1439–1443.

(36) Sengodan, S.; Choi, S.; Jun, A.; Shin, T. H.; Ju, Y.; Jeong, H. Y.; Shin, J.; Irvine, J. T. S.; Kim, G. Layered Oxygen-Deficient Double Perovskite as an Efficient and Stable Anode for Direct Hydrocarbon Solid Oxide Fuel Cells. *Nat. Mater.* **2015**, *14*, 205–209.

(37) Choi, S.; Yoo, S.; Kim, J.; Park, S.; Jun, A.; Sengodan, S.; Kim, J.; Shin, J.; Jeong, H. Y.; Choi, Y.; *et al.* Highly Efficient and Robust Cathode Materials for Low-Temperature Solid Oxide Fuel Cells: $PrBa_{0.5}Sr_{0.5}Co_{2-x}Fe_xO_{5+\delta}$. *Sci. Rep.* **2013**, *3*, 2426.

(38) Kim, J. H.; Manthiram, A. Layered $LnBaCo_2O_{5+\delta}$ Perovskite Cathodes for Solid Oxide Fuel Cells: An Overview and Perspective. *J. Mater. Chem. A* **2015**, *3*, 24195–24210.

(39) Yoo, S.; Jun, A.; Ju, Y.; Odkhuu, D.; Hyodo, J.; Jeong, H. Y.; Park, N.; Shin, J.; Ishihara, T.; Kim, G. Development of Double-Perovskite Compounds as Cathode Materials for Low-Temperature Solid Oxide Fuel Cells **. *Angew. Chem. Int. Ed.* **2014**, *53*, 13064 –13067.

(40) Choi, S.; Sengodan, S.; Park, S.; Ju, Y.-W.; Kim, J.; Hyodo, J.; Jeong, H. Y.; Ishihara, T.; Shin, J.; Kim, G. A Robust Symmetrical Electrode with Layered Perovskite Structure for Direct Hydrocarbon Solid Oxide Fuel Cells: $PrBa_{0.8}Ca_{0.2}Mn_2O_{5+\delta}$. *J. Mater. Chem. A* **2016**, *4*, 1747–1753.

(41) Kim, S.; Lee, S.; Kim, J.; Shin, J.; Kim, G. Self-Transforming Configuration Based on Atmospheric-Adaptive Materials for Solid Oxide Cells. *Sci. Rep.* **2018**, *8*, 17149.

(42) Schlupp, M. V. F.; Evans, A.; Martynczuk, J.; Prestat, M. Micro-Solid Oxide Fuel Cell Membranes Prepared by Aerosol-Assisted Chemical Vapor Deposition. *Adv. Energy Mater.* **2014**, *4*, 1–7.

(43) Gorte, R. J.; Vohs, J. M. Nanostructured Anodes for Solid Oxide Fuel Cells. *Curr. Opin.*

Colloid Interface Sci. **2009**, *14*, 236–244.

(44) Kim, S.; Jun, A.; Kwon, O.; Kim, J.; Yoo, S.; Jeong, H. Y.; Shin, J.; Kim, G. Nanostructured Double Perovskite Cathode With Low Sintering Temperature For Intermediate Temperature Solid Oxide Fuel Cells. *ChemSusChem* **2015**, *8*, 3153–3158.

(45) Neagu, D.; Tsekouras, G.; Miller, D. N.; Menard, H.; Irvine, J. T. *In Situ* Growth of Nanoparticles through Control of Non-Stoichiometry. *Nat Chem* **2013**, *5*, 916–923.

(46) Du, Z.; Zhao, H.; Yi, S.; Xia, Q.; Gong, Y.; Zhang, Y.; Cheng, X.; Li, Y.; Gu, L.; Świerczek, K. High-Performance Anode Material $Sr_2FeMo_{0.65}Ni_{0.35}O_{6-\delta}$ with in Situ Exsolved Nanoparticle Catalyst. *ACS Nano* **2016**, *10*, 8660–8669.

(47) Sun, Y. F.; Zhang, Y. Q.; Chen, J.; Li, J. H.; Zhu, Y. T.; Zeng, Y. M.; Amirkhiz, B. S.; Li, J.; Hua, B.; Luo, J. L. New Opportunity for in Situ Exsolution of Metallic Nanoparticles on Perovskite Parent. *Nano Lett.* **2016**, *16*, 5303–5309.

(48) Ye, L.; Zhang, M.; Huang, P.; Guo, G.; Hong, M.; Li, C.; Irvine, J. T. S.; Xie, K. Enhancing CO2 Electrolysis through Synergistic Control of Non-Stoichiometry and Doping to Tune Cathode Surface Structures. *Nat. Commun.* **2017**, *8*, 14785.

(49) Nishihata, Y.; Mizuki, J.; Akao, T.; Tanaka, H.; Uenishi, M.; Kimura, M.; Okamoto, T.; Hamada, N. Self-Regeneration of a Pd-Perovskite Catalyst for Automotive Emissions Control. *Nature* **2002**, *418*, 164–167.

(50) Neagu, D.; Oh, T.-S.; Miller, D. N.; Ménard, H.; Bukhari, S. M.; Gamble, S. R.; Gorte, R. J.; Vohs, J. M.; Irvine, J. T. S. Nano-Socketed Nickel Particles with Enhanced Coking Resistance Grown in Situ by Redox Exsolution. *Nat. Commun.* **2015**, *6*, 8120.

(51) Neagu, D.; Irvine, J. T. S. Structure and Properties of $La_{0.4}Sr_{0.4}TiO_3$ Ceramics for Use as Anode Materials in Solid Oxide Fuel Cells. *Chem. Mater.* **2010**, *22*, 5042–5053.

(52) Wei, T.; Jia, L.; Zheng, H.; Chi, B.; Pu, J.; Li, J. LaMnO3-Based Perovskite with in-Situ Exsolved Ni Nanoparticles: A Highly Active, Performance Stable and Coking Resistant Catalyst for CO_2 Dry Reforming of CH4. *Appl. Catal. A Gen.* **2018**, *564*, 199–207.

(53) Zhu, T.; Troiani, H.; Mogni, L. V.; Santaya, M.; Han, M.; Barnett, S. A. Exsolution and Electrochemistry in Perovskite Solid Oxide Fuel Cell Anodes: Role of Stoichiometry in $Sr(Ti,Fe,Ni)O_3$. *J. Power Sources* **2019**, *439*, 227077.

(54) Neagu, D.; Papaioannou, E. I.; Ramli, W. K. W.; Miller, D. N.; Murdoch, B. J.; Ménard, H.; Umar, A.; Barlow, A. J.; Cumpson, P. J.; Irvine, J. T. S.; *et al.* Demonstration of Chemistry at a Point through Restructuring and Catalytic Activation at Anchored Nanoparticles. *Nat. Commun.* **2017**, *8*, 1855.

(55) Cui, S.-H.; Li, J.-H.; Zhou, X.-W.; Wang, G.-Y.; Luo, J.-L.; Chuang, K. T.; Bai, Y.; Qiao, L.-J. Cobalt Doped $LaSrTiO_{3-\delta}$ as an Anode Catalyst: Effect of Co Nanoparticle Precipitation on

SOFCs Operating on H2S-Containing Hydrogen. *J. Mater. Chem. A* **2013**, *1*, 9689–9696.

(56) Sengodan, S.; Ju, Y. W.; Kwon, O.; Jun, A.; Jeong, H. Y.; Ishihara, T.; Shin, J.; Kim, G. Self-Decorated MnO Nanoparticles on Double Perovskite Solid Oxide Fuel Cell Anode by in Situ Exsolution. *ACS Sustain. Chem. Eng.* **2017**, *5*, 9207–9213.

(57) Kwon, O.; Sengodan, S.; Kim, K.; Kim, G.; Jeong, H. Y.; Shin, J.; Ju, Y.-W.; Han, J. W.; Kim, G. Exsolution Trends and Co-Segregation Aspects of Self-Grown Catalyst Nanoparticles in Perovskites. *Nat. Commun.* **2017**, *8*, 15967.

(58) Kwon, O.; Kim, K.; Joo, S.; Jeong, H. Y.; Shin, J.; Han, J. W.; Sengodan, S.; Kim, G. Self-Assembled Alloy Nanoparticles in Layered Double Perovskite as a Fuel Oxidation Catalyst for Solid Oxide Fuel Cells. *J. Mater. Chem. A* **2018**, *6*, 15947.

(59) Joo, S.; Kwon, O.; Kim, K.; Kim, S.; Kim, H.; Shin, J.; Jeong, H. Y.; Sengodan, S.; Han, J. W.; Kim, G. Cation-Swapped Homogeneous Nanoparticles in Perovskite Oxides for High Power Density. *Nat. Commun.* **2019**, *10*, 697.

(60) Yang, C.; Li, J.; Lin, Y.; Liu, J.; Chen, F.; Liu, M. In Situ Fabrication of CoFe Alloy Nanoparticles Structured $(Pr_{0.4}Sr_{0.6})_3(Fe_{0.85}Nb_{0.15})_2O_7$ Ceramic Anode for Direct Hydrocarbon Solid Oxide Fuel Cells. *Nano Energy* **2015**, *11*, 704–710.

(61) Du, Z.; Zhao, H.; Yi, S.; Xia, Q.; Gong, Y.; Zhang, Y.; Cheng, X.; Li, Y.; Gu, L.; Świerczek, K. High-Performance Anode Material $Sr_2FeMo_{0.65}Ni_{0.35}O_{6-\delta}$ with *In Situ* Exsolved Nanoparticle Catalyst. *ACS Nano* **2016**, acsnano.6b03979.

(62) Wu, N.; Wang, W.; Zhong, Y.; Yang, G.; Qu, J.; Shao, Z. Nickel-Iron Alloy Nanoparticle-Decorated K_2NiF_4-Type Oxide as an Efficient and Sulfur-Tolerant Anode for Solid Oxide Fuel Cells. *ChemElectroChem* **2017**, *4*, 2378–2384.

(63) Glazer, A. M. Simple Ways of Determining Perovskite Structures. *Acta Crystallogr. Sect. A* **1975**, *31*, 756–762.

(64) Grabowska, E. Selected Perovskite Oxides: Characterization, Preparation and Photocatalytic Properties-A Review. *Appl. Catal. B Environ.* **2016**, *186*, 97–126.

(65) Katz, M. B.; Zhang, S.; Duan, Y.; Wang, H.; Fang, M.; Zhang, K.; Li, B.; Graham, G. W.; Pan, X. Reversible precipitation/dissolution of precious-metal clusters in perovskite based catalyst materials: Bulk versus surface re-dispersion. *J. Catal.* **2012**, *293*, 145–148.

(66) Sun, Y-F.; Zhang, Y-Q.; Chen, J.; Li, J-H.; Zhu, Y-T.; Zeng, Y-M.; Amirkhiz, B. S.; Li, J.; Hua, B.; Luo, J-L. New Opportunity for in Situ Exsolution of Metallic Nanoparticles on Perovskite Parent. Nano Lett. **2016**, *16*, 5303-5309.

Chapter 2. Exsolution trends and co-segregation aspects of self-grown catalyst nanoparticles in perovskites

This chapter has been published

Reproduced from Kwon, O.; Sengodan, S.; Kim, K.; Kim, G.; Jeong H. Y.; Shin, J.; Ju, Y. -W.; Kim, G. Exsolution trends and co-segregation aspects of self-grown catalyst nanoparticles in perovskites. *Nat. Commun.* **2017**, *8*, 15967 DOI: 10.1038/ncomms15967.

2.1 Introduction

Perovskites, a class of metal oxides with well-defined structures, have recently occupied a predominant position within the portfolio of compounds that have been explored as the electrode materials for fuel cells, electronic devices, heterogeneous catalysis in syngas production and components for solar cells[1–4]. This wide variety of properties originates from the exceptional structural and compositional flexibility of the perovskite structures. In recent years, composite materials realized by integration of functional catalyst nanoparticles with perovskite oxide supports have received rising attention. The nanoparticle-supported perovskite oxide materials can be prepared by conventional deposition methods, such as wet impregnation or vapor deposition[5–7]. Although these techniques are applied widely, controllable anchoring still encounters many challenges. For example, a wet impregnation technique always suffers from coarsening and agglomeration of the catalyst nanoparticles on the surface of the perovskite, leading to severe cell degradation. Therefore, an advanced approach to prepare well-defined nanoparticle-supported perovskites is required to overcome the drawbacks of conventional methods.

Exsolution based on *in situ* growth of metal nanoparticles from the parent perovskite is an attractive approach for designing nanoparticle-supported perovskite materials. The catalytically active transition metals, such as Pd, Ru, Pt, Co and Ni, are incorporated on the B site of perovskite oxide (ABO_3) during material synthesis in air, and then the transition metals are exsolved from the perovskite backbone as highly dispersed nanoparticles under a reducing atmosphere[8–11]. The exsolved nanoparticles are socketed on the surface of the perovskite, preventing agglomeration and coarsening of the nanoparticles during operation conditions[12]. Furthermore, the Irvine group used a different strategy through the control of non-stoichiometry (A-site deficiency in the ABO_3 stoichiometry) to promote exsolution[13]. Well-defined nanoparticle-supported perovskites have been obtained in these reports; however, the exsolution trends of transition metals is still scarce and has been focused on simple perovskites.

Recently, layered perovskite structures have received considerable attention because of their interesting properties, such as high electrical conductivity, fast surface oxygen exchange and easy oxygen ion

diffusion[14–17]. However, there have been very few reports focused on exsolution in layered perovskites due to the lack of redox stable layered perovskites. Therefore, exsolution trends in redox stable layered perovskites are of particular interest, not only from scientific but also from engineering points of view, because they can provide a strategy of tailoring materials for fuel cell electrodes, catalytic oxidation of hydrocarbon and thermochemical hydrogen production from water[18,19].

Here we report the contribution of various transition metals for in situ growth of finely dispersed metal nanoparticles on a $PrBaMn_{1.7}T_{0.3}O_{5+\delta}$ (T = Mn, Co, Ni, and Fe) layered perovskite with the aim to verify trends in exsolution and improve the electrochemical performance of solid oxide fuel cell anodes. The exsolution trends of the B-site dopants (Mn, Co, Ni and Fe) are verified by a transmission electron microscopy (TEM) analysis and density functional theory (DFT) calculations.

2.2 Experimental

Materials synthesis. $Pr_{0.5}Ba_{0.5}Mn_{0.85}T_{0.15}O_{3-\delta}$ (T = Mn, Co, Ni, and Fe) powders were prepared by the Pechini method. Stoichiometric amounts of $Pr(NO_3)_3{\cdot}6H_2O$ (Aldrich, 99.9%, metal basis), $Ba(NO_3)_2$ (Aldrich, 99+%), $Mn(NO_3)_2{\cdot}4H_2O$ (Aldrich, 98%), $Co(NO_3)_2{\cdot}6H_2O$ (Aldrich, 98+%), $Ni(NO_3)_2{\cdot}6H_2O$ (Aldrich, 98.5+%), and $Fe(NO_3)_3{\cdot}9H_2O$ (Aldrich, 98+%) were dissolved in distilled water with proper amounts of ethylene glycol and citric acid, followed by combustion to obtain fine powders. These powders were calcined at 600 °C for 4h and then sintered at 950 °C for 4h in air. The A-site layered $PrBaMn_{1.7}T_{0.3}O_{5+\delta}$ (T = Mn, Co, Ni, and Fe) was obtained by annealing $Pr_{0.5}Ba_{0.5}Mn_{0.85}T_{0.15}O_{3-\delta}$ (T = Mn, Co, Ni, and Fe) oxide, respectively, at 800 °C for 4h in humidified H_2. The chemical composition of the synthesized powders and their abbreviations are given in Table 2.1. A thin $Pr_{0.5}Ba_{0.5}MnO_3$ film was deposited on the dense Al_2O_3 substrate by pulsed laser deposition (PLD) by using a commercial system (PLD-7; PASCAL, Japan). The oxygen pressure was adjusted to 0.67 Pa before the deposition process by introducing commercially available oxygen (without further purification), and the substrate was heated to 800 °C by using an infrared heater. An excimer laser was used with a power of 180 mJ $pulse^{-1}$ and a frequency of 10 Hz to deposit the film.

Structure characterization. The crystal structures of the samples were identified by X-ray powder diffraction (XRD) (Rigaku-diffractometer, Cu Ka radiation, 40 kV, 30 mA). The morphologies of the anode materials were investigated using a field emission scanning electron microscope (SEM). Transmission electron microscopy (TEM) images were obtained with a JEOL JEM 2100F with a probe forming (STEM) Cs (spherical aberration) corrector at 200 kV. Cross-sectional samples for the TEM analysis were prepared by using a focused ion beam (FIB, Helios 450HP, FEI). X-ray photoelectron spectroscopy (XPS) analyses were conducted on ESCALAB 250XI from Thermo Fisher Scientific with a monochromated Al-Ka (ultraviolet He1, He2) X-ray source. The base pressure inside the spectrometer during analysis was 1×10^{-10} mmHg.

Computational methods. DFT calculations were carried out using the Vienna ab initio Simulation Package (VASP).[20] Exchange-correlation energies were treated by the Perdew-Burke-Ernzerhof (PBE) functional based on generalized gradient approximation (GGA). A plane wave expansion with a cutoff of 400 eV was used with a 3 × 3 × 1 Monkhorst-Pack *k*-point sampling of the Brillouin zone for all slab model calculations.[21] Gaussian smearing was used with a width of 0.05 eV to determine partial occupancies. Geometries were relaxed using a conjugate gradient algorithm until the forces on all unconstrained atoms were less than 0.03 eV/Å. In order to take into account for on-site Coulomb and exchange interactions, we used GGA+*U* schemes with the effective *U* values of 4.0, 3.3, 6.4, and 4.0 to Mn, Co, Ni, and Fe respectively.[22] Based on our XRD and TEM images, the L-PBMO structure was optimized with a tetragonal *P4/mmm* structure ($a = b = 4.035$, $c = 7.940$) (Figure 2.1a). An eight layered PBMO slab model was also constructed with vacuum thickness of up to 17 Å, which was sufficient to describe surface phenomena. (Figure 2.1b).

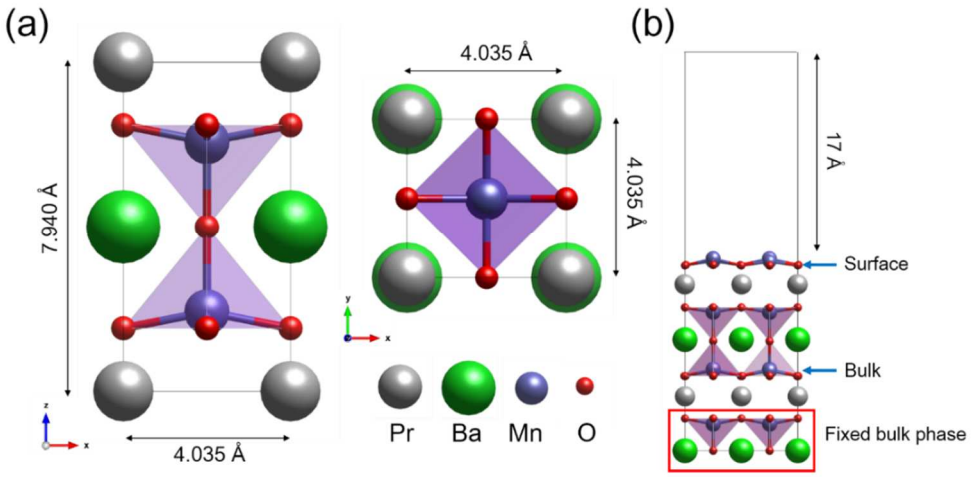

Figure 2.1. Optimized (a) bulk and (b) surface structures of L-PBMO that we used for DFT calculations in this study.

The oxygen vacancy formation energy (E_{vf}) was calculated from the total energies of the supercells with various defect positions (Figure 2.2).

$$E_{\mathrm{vf}} = \left(E_{\mathrm{vac}} + \frac{1}{2} E_{O_2} \right) - E_{\mathrm{clean}}, \qquad (1)$$

where E_{vac} is the total energy of the system containing an oxygen vacancy, E_{O_2} is the total energy of an isolated oxygen molecule in the gas phase, and E_{clean} is the total energy of optimized perfect slab structures. The segregation energy of B-site metal (E_{seg}) with or without oxygen vacancies is defined as the total energy difference between the systems with the exsoluting B-site metal located at the surface and in the bulk:

$$E_{\text{seg}} = E_{(\text{B-Vo})\_\text{surf}} - E_{(\text{B-Vo})\_\text{bulk}}, \quad (2)$$

where $E_{(\text{B-Vo})\_\text{surf}}$ and $E_{(\text{B-Vo})\_\text{bulk}}$ are the total energy of the exsoluting B-site metal located at the surface and in the bulk with or without oxygen vacancies, respectively. With our definition, a negative segregation energy indicates that the B-metal energetically prefers to exsolve toward the surface.

Fabrication of fuel cells. $La_{0.9}Sr_{0.1}Ga_{0.8}Mg_{0.2}O_{3-\delta}$ (LSGM) powder was prepared by conventional solid-state reaction and electrolyte substrate was prepared by pressing and followed by sintering at 1475 °C. Stoichiometric amounts of La_2O_3 (Sigma 99.99%), $SrCO_3$ (Sigma, 99.99%), Ga_2O_3 (Sigma, 99.99%), and MgO (Sigma, 99.9%) powders were ball milled in ethanol for 24 h. After drying, the powder was calcined at 1000 °C for 6 h. The thickness of LSGM electrolyte was polished about 250 μm. $La_{0.4}Ce_{0.6}O_{2-\delta}$ (LDC) was also prepared by ball milling stoichiometric amounts of La_2O_3 and CeO_2 (Sigma, 99.99%) in ethanol and then calcined at 1000 °C for 6 h. For preparation of the anode ink, $Pr_{0.5}Ba_{0.5}Mn_{0.85}T_{0.15}O_3$ (T= Mn, Co, Ni, and Fe) was mixed with an organic binder (Heraeus V006) (1:2 weight ratio). $NdBa_{0.5}Sr_{0.5}Co_{1.5}Fe_{0.5}O_{5+\delta}$-$Ce_{0.9}Gd_{0.1}O_{2-\delta}$ (NBSCF50-GDC) cathode ink was prepared by pre-calcined cathode and GDC powders (at a weight ratio of 60:40) were mixed using ball milling, together with an organic binder. The electrode inks were applied on the LSGM pellet by screen printing method, and then calcined at 950 °C in air for 4 h. The porous electrode had active area of 0.36 cm^2 and thickness about 20 μm. LDC layer was used as the buffer layer between the anode and the electrolyte to prevent inter-diffusion of ionic species between anode and LSGM electrolyte. For fuel cell performance tests, the cells were mounted on alumina tubes with ceramic adhesives (Ceramabond 552, Aremco). Silver paste and silver wire were used for electrical connections to both the anode and the cathode. The entire cell was placed inside a furnace and heated to the desired temperature. I-V polarization curves were measured using a BioLogic Potentiostat.

Chemical composition	**Abbreviation**	**Chemical composition**	**Abbreviation**
$Pr_{0.5}Ba_{0.5}MnO_{3-\delta}$	S-PBMO	$PrBaMn_2O_{5+\delta}$	L-PBMO
$Pr_{0.5}Ba_{0.5}Mn_{0.85}Co_{0.15}O_{3-\delta}$	S-PBMCO	$PrBaMn_{1.7}Co_{0.3}O_{5+\delta}$	L-PBMCO
$Pr_{0.5}Ba_{0.5}Mn_{0.85}Ni_{0.15}O_{3-\delta}$	S-PBMNO	$PrBaMn_{1.7}Ni_{0.3}O_{5+\delta}$	L-PBMNO
$Pr_{0.5}Ba_{0.5}Mn_{0.85}Fe_{0.15}O_{3-\delta}$	S-PBMFO	$PrBaMn_{1.7}Fe_{0.3}O_{5+\delta}$	L-PBMFO

Table 2.1. Chemical compositions and abbreviations of samples.

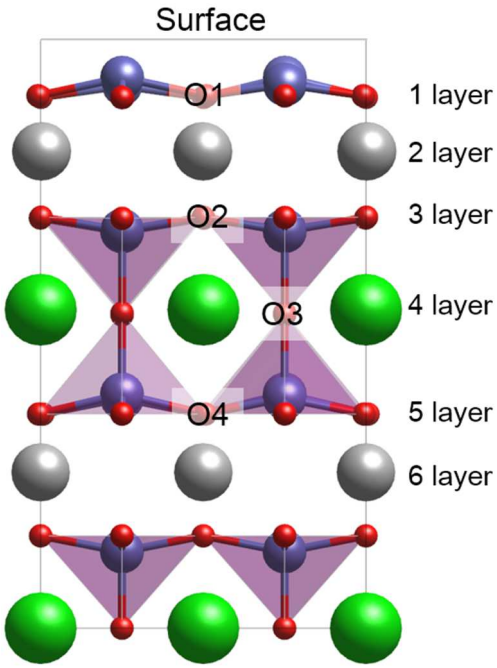

Figure 2.2. Side view of L-PBMO. Possible vacancy positions except in the bottom two layers were considered to calculate vacancy formation energies (Table S1). The most stable vacancy sites at each layer's lattice oxygen are marked in each figure (O1-O4).

2.3 Results and Discussions

The crystalline structures of the oxide materials before and after reduction were examined using the X-ray diffraction (XRD) technique. As shown in Figure 2.3, diffraction patterns for all samples sintered at 950 ºC in air exhibit a simple perovskite structure with a mixture of cubic and hexagonal phases without any secondary phases.[1] Apparently, the B-site doping has no influence on the formation of the simple perovskite structure. Figure 2.4 shows the XRD patterns of L-PBMO, $PrBaMn_{1.7}Co_{0.3}O_{5+\delta}$(L-PBMCO), $PrBaMn_{1.7}Ni_{0.3}O_{5+\delta}$(L-PBMNO), and $PrBaMn_{1.7}Fe_{0.3}O_{5+\delta}$(L-PBMFO) after reduction in humidified H_2 (3% H_2O) at 800 ºC for 4h. The reduced samples present a single phase of the layered perovskite structure with metal or metal oxide phases, indicating that the phase transition from the simple perovskite to the layered perovskite and exsolution occurred in the reducing atmosphere. Although all the samples were reduced under the same conditions, MnO, metallic Co, and Ni phases are observed in the L-PBMO, L-PBMCO, and L-PBMNO, respectively, and no Fe phase is observed in the L-PBMFO. These results clearly show that MnO, Co, and Ni are more easily exsolved to form nanoparticles than Fe, and thus B-site transition metals show some trend to exsolve in the layered perovskite oxide.

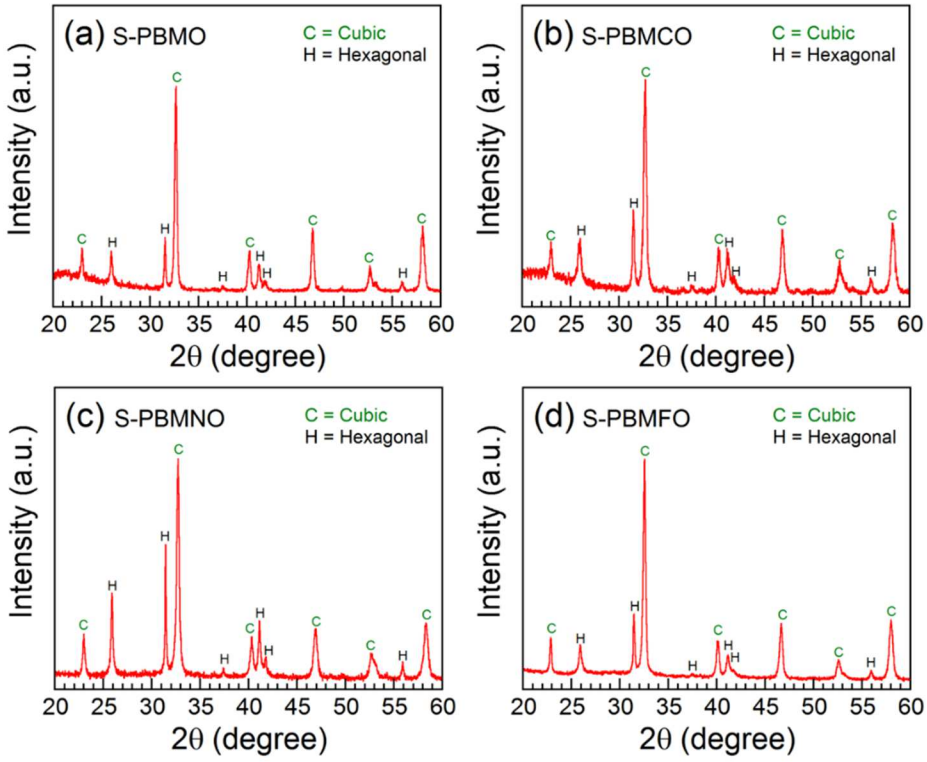

Figure 2.3. X-ray diffraction patterns of (a) S-PBMO, (b) S-PBMCO, (c) S-PBMNO, and (d) S-PBMFO after sintering at 950 ºC for 4h in air.

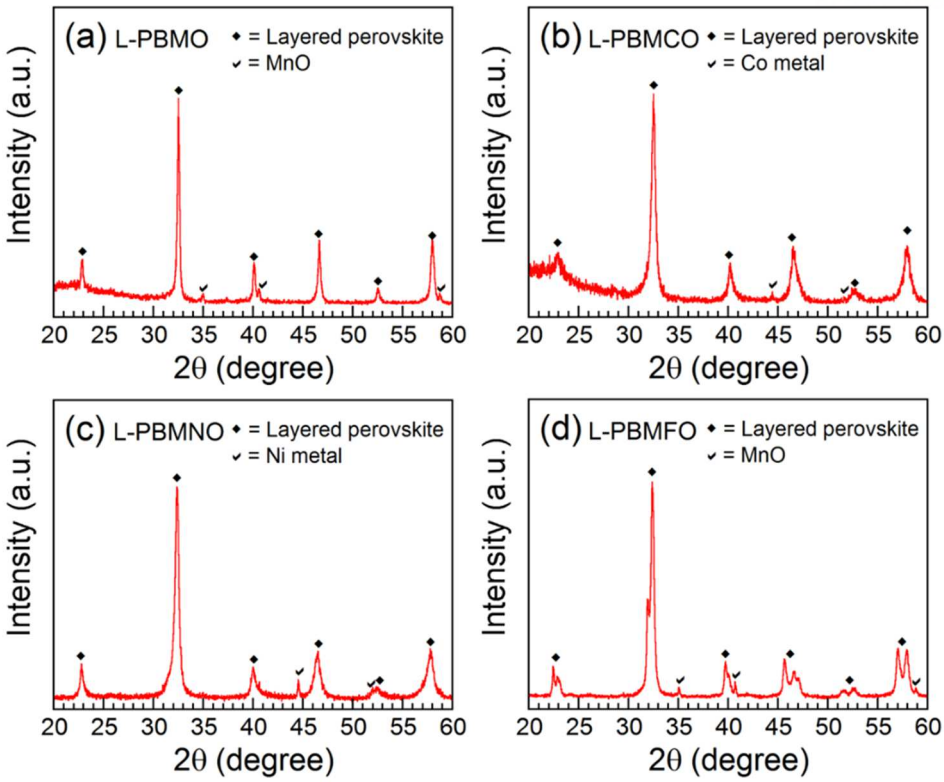

Figure 2.4. X-ray diffraction patterns of (a) L-PBMO, (b) L-PBMCO, (c) L-PBMNO, and (d) L-PBMFO after reducing at 800 ºC for 4h in humidified (3% H_2O) H_2.

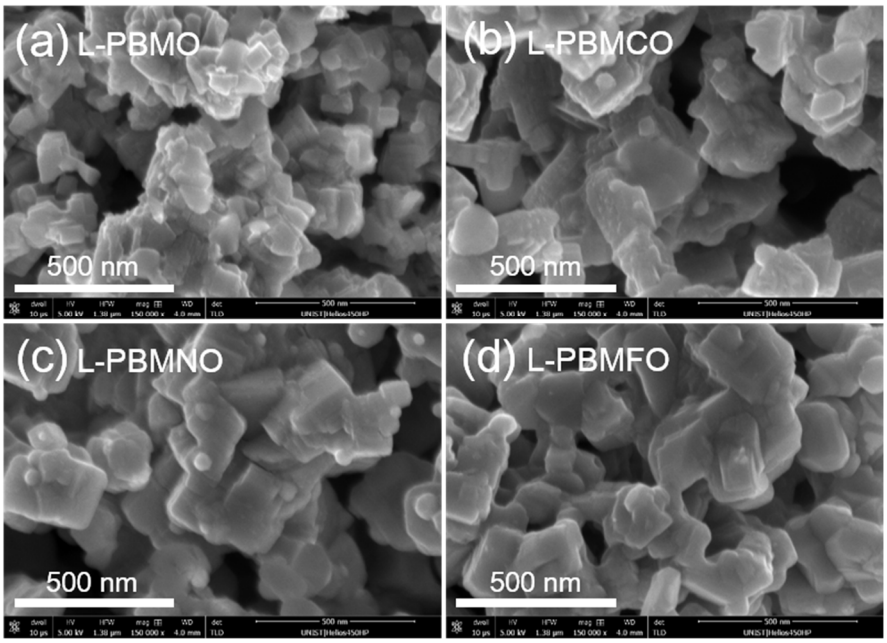

Figure 2.5. Scanning electron microscope images of (a) L-PBMO, (b) L-PBMCO, (c) L-PBMNO, and (d) L-PBMFO after reducing treatments using a humidified (3% H_2O) H_2 at 800 ºC.

Figure 2.5 shows scanning electron microscope (SEM) images of (a) L-PBMO, (b) L-PBMCO, (c) L-PBMNO, and (d) L-PBMFO after reducing treatment using humidified (3% H_2O) H_2 at 800 ºC. As shown in the SEM images, the surface morphologies of the reduced samples are similar, and some small spherical nanoparticles with 20~50 nm diameter are only observed on the surface of L-PBMCO and L-PBMNO. Although Co and Ni nanoparticles are readily observed in the SEM images, this is not straightforward in the case of MnO because the population of the exsolved MnO nanoparticles is small in dimension and low in number.

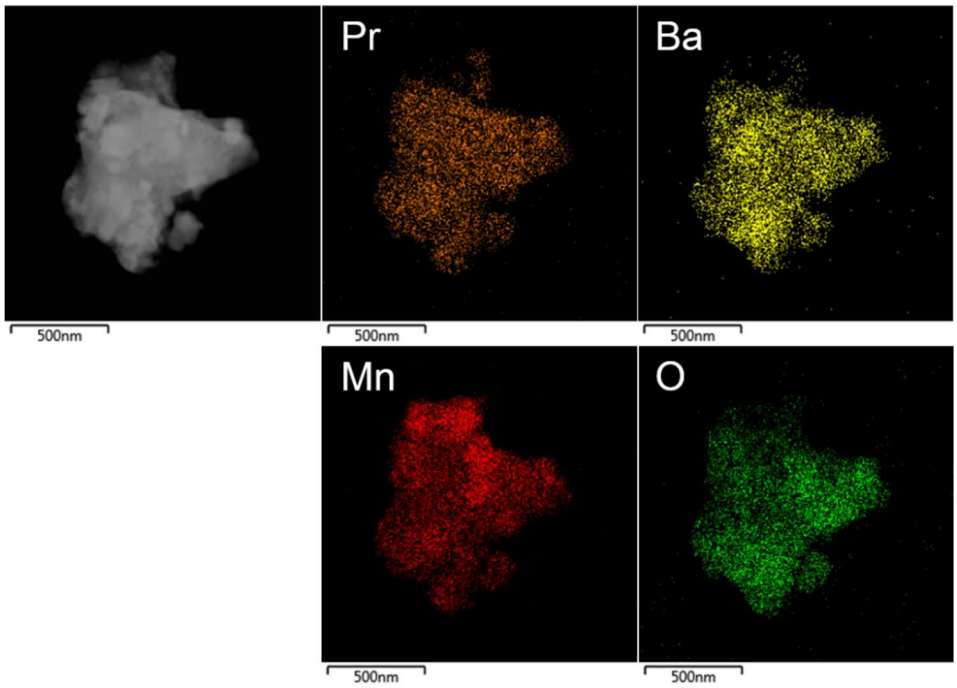

Figure 2.6. Energy dispersive spectroscopy (EDS) micrographs and elemental mapping of Pr, Ba, Mn, and O, respectively, for L-PBMO after reducing at 800 ºC in humidified (3% H_2O) H_2.

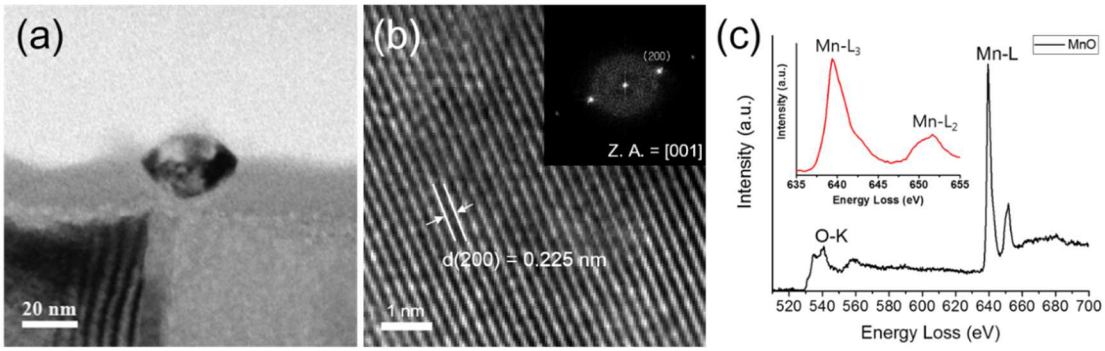

Figure 2.7. (a) A bright-field (BF) TEM image of L-PBMO sample. (b) Magnified high-resolution TEM image and (c) Electron Energy-Loss Spectroscopy (EELS) analysis of exsolved MnO nanoparticle.

To observe the exsolved nanoparticles and morphologies of the reduced samples in detail, we measured transmission electron microscopy (TEM). Energy dispersive spectroscopy (EDS) revealed that Mn and O elements coexist in the L-PBMO (Figure 2.6), speculating that MnO nanoparticles are exsolved in reducing atmosphere as seen in the XRD results. In the bulk state, MnO exsolution is not easily detectable because both MnO and L-PBMO are oxide materials.[13] To realize the nature of exsolved MnO nanoparticles, a $Pr_{0.5}Ba_{0.5}MnO_3$ polycrystalline film was fabricated by pulse laser deposition (PLD) followed by reduction in H_2 at 800 °C for the exsolution of the nanoparticles from the lattice. From the bright-field TEM image (Figure 2.7a), it is observed that the nanoparticles having roughly 40 nm diameter are successfully exsolved from the L-PBMO in the reducing atmosphere. For the exsolved nanoparticles of L-PBMO, the lattice space between planes is identified as 0.225 nm by high-resolution TEM and Fast Fourier Transformation (FFT) (Figure 2.7b), corresponding to the lattice constant of (200) planes of the MnO, which is in agreement with the XRD results (Figure 2.4a). To identify the oxidation state of Mn nanoparticles, electron energy-loss spectroscopy (EELS) was performed and the results indicated that O-K and Mn-$L_{2,3}$ features are consistent with MnO, as reported in a previous study (Figure 2.7c).[23, 24] Based on the relative reducibility and thermodynamic possibility, Mn exsolution from the L-PBMO would be MnO rather than metallic Mn.[25] Generally, among manganese oxides there are four relevant oxides (MnO, Mn_3O_4, Mn_2O_3 and MnO_2) in the redox cycling reactions. Among them, Mn_3O_4 (Eq. 1) and Mn_2O_3 (Eq. 2) are easily reduced to MnO in a reducing atmosphere, and the reaction is identified by the values of Gibbs energy ΔG_r. In the case of MnO, however, the reduction of MnO to metallic Mn (Eq. 3) is thermodynamically unfavourable at 1000 K due to the positive value of ΔG_r for MnO reduction.

$$Mn_3O_4(s) \xleftrightarrow[1000\ K,\ H_2]{} 3MnO(s) + H_2O(g) \quad \Delta G_r = -86.63\ kJ\ mol^{-1} \qquad (1)$$

$$Mn_2O_3(s) \xleftrightarrow[1000\ K,\ H_2]{} 2MnO(s) + H_2O(g) \quad \Delta G_r < -86.63\ kJ\ mol^{-1} \qquad (2)$$

$$MnO(s) \xleftrightarrow[1000\ K,\ H_2]{} Mn(s) + H_2O(g) \quad \Delta G_r > 100\ kJ\ mol^{-1} \qquad (3)$$

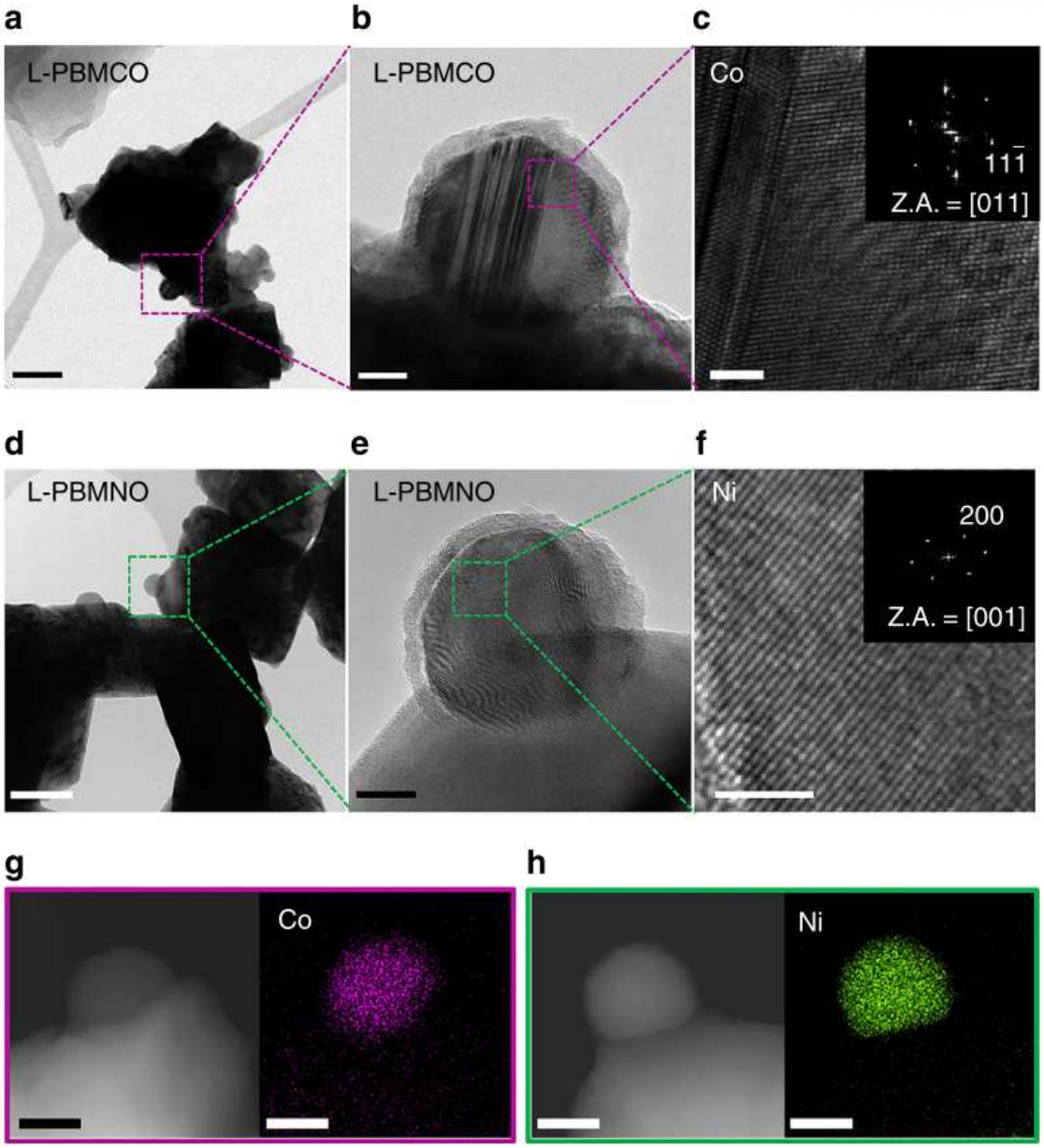

Figure 2.8. Transmission electron microscopic analysis. (a) A bright-field (BF) TEM image; scale bar, 100nm and (b) high-resolution (HR) TEM image of $PrBaMn_{1.7}Co_{0.3}O_{5-\delta}$ (L-PBMCO) sample; scale bar 10 nm. (c) Magnified HR TEM image of exsolved Co nanoparticle; scale bar 2 nm, (d) BF TEM image; scale bar 100nm and (e) HR TEM image of $PrBaMn_{1.7}Ni_{0.3}O_{5-\delta}$(L-PBMNO) sample; scale bar 10 nm. (f) Magnified HR TEM image of Ni nanoparticle; scale bar 2 nm. (g) High-angle annular dark-field (HAADF) image of the L-PBMCO with the EDS elemental map of Co; scale bar 25 nm. (h) HAADF image of the L-PBMNO with the EDS elemental map of Ni; scale bar 25 nm.

Figure 2.8 shows bright-field TEM images and high-resolution TEM images of reduced L-PBMCO and L-PBMNO. As shown in Figure 2.8a and 2.8d, the morphologies of L-PBMCO and L-PBMNO are similar to SEM images. From the high-resolution TEM images (Figure 2.8b and 2.8e), it is observed that the nanoparticles having roughly 30 nm diameter are successfully exsolved from the L-PBMCO and L-PBMNO, respectively, in reducing atmosphere. In addition, the lattice spaces between planes of exsolved nanoparticles are 0.204 nm (Figure 2.8c) and 0.176 nm (Figure 2.8f), and these values are consistent with the lattice constant of $(11\bar{1})$ planes of Co metal and (200) planes of Ni metal, respectively. As shown in Figure 2.8g and 2.8h, the EDS micrograph and elemental mapping also reveal that Co and Ni nanoparticles are exsolved from L-PBMCO and L-PBMNO, respectively. Unlike L-PBMO, metal nanoparticles are exsolved without MnO from L-PBMCO and L-PBMNO, which is also supported by thermodynamic possibilities. The reductions of CoO and NiO to metallic Co and Ni are thermodynamically favourable at 1000 K due to the negative value of ΔG_r for the CoO (Eq. 4) and NiO (Eq. 5) reductions.[26] As noted from the XRD results, MnO nanoparticles are exsolved from L-PBMFO in humidified H_2 (3% H_2O) at 800 °C, which is also confirmed by the TEM-EDS analysis results (Figure 2.9).

$$\mathrm{CoO(s)} \xleftrightarrow[1000\mathrm{K},\ \mathrm{H_2}]{} \mathrm{Co(s)} + \mathrm{H_2O(g)} \quad \Delta G_\mathrm{r} = -29.172\ \mathrm{kJ\ mol^{-1}} \quad (4)$$

$$\mathrm{NiO(s)} \xleftrightarrow[1000\mathrm{K},\ \mathrm{H_2}]{} \mathrm{Ni(s)} + \mathrm{H_2O(g)} \quad \Delta G_\mathrm{r} = -43.48\ \mathrm{kJ\ mol^{-1}} \quad (5)$$

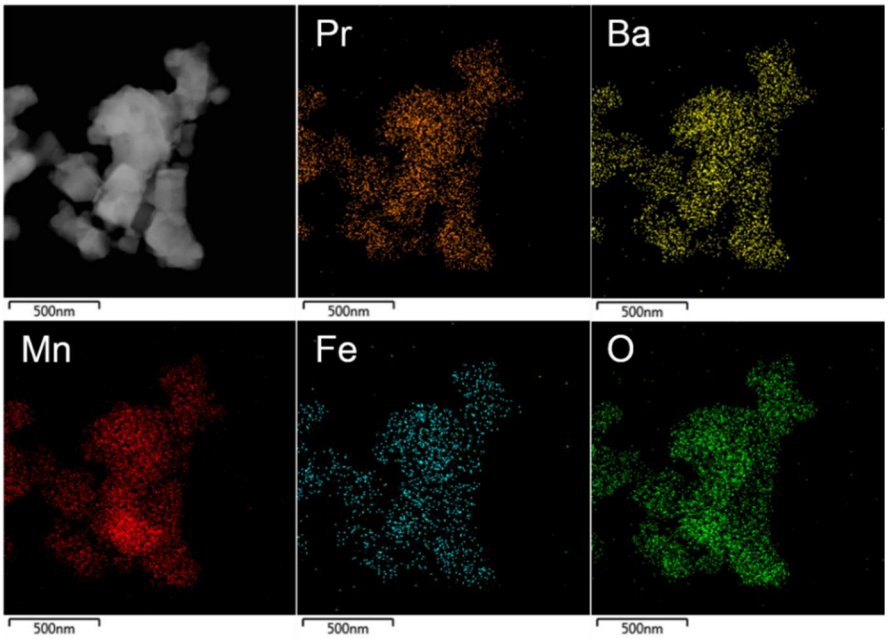

Figure 2.9. Energy dispersive spectroscopy (EDS) micrographs and elemental mapping of Pr, Ba, Mn, Fe, and O, respectively, for L-PBMFO after reducing at 800 °C in humidified (3% H_2O) H_2.

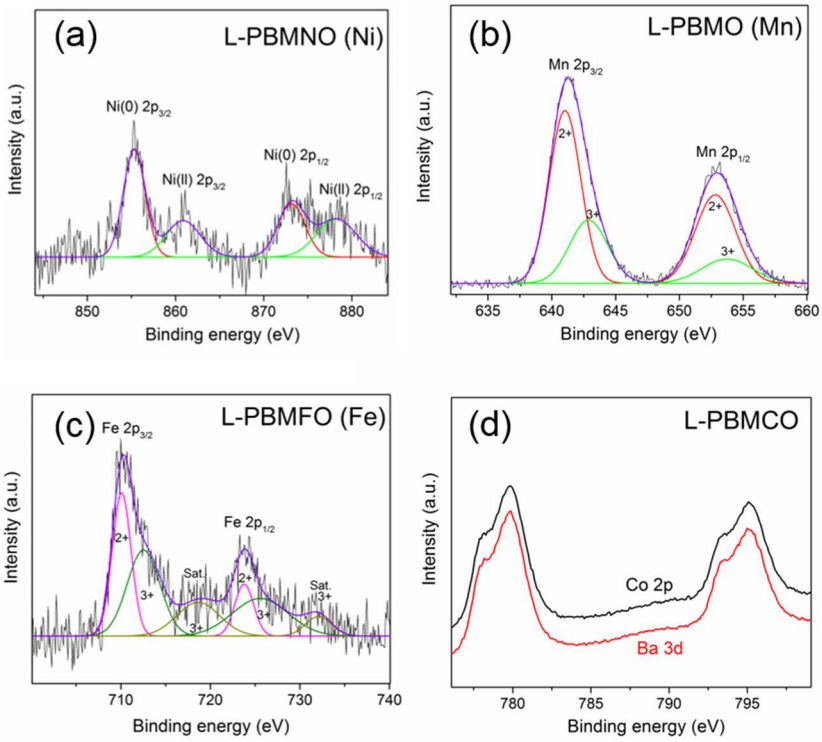

Figure 2.10. XPS spectra of (a) Ni 2p in L-PBMNO, (b) Mn 2p in L-PBMO, (c) Fe 2p in L-PBMFO, and (d) Co 2p and Ba 3d in L-PBMCO.

X-ray photoelectron spectroscopy (XPS) was performed to examine oxidation states of B-site dopants in the L-PBMO, L-PBMCO, L-PBMNO, and L-PBMFO. As shown in Figure 2.10a, the binding energy peaks of metallic Ni (855.3 and 873.1 eV) could be detected in L-PBMNO[27], which is consistent with the XRD and TEM results. Furthermore, the percentages of metallic Ni and Ni^{2+} are about 58 and 42 %, respectively, indicating that approximately 58 % of Ni migrates to the surface in L-PBMNO. Figure 2.10b shows the binding energy peaks of Mn^{2+} (641 and 652.8 eV) and Mn^{3+} (642.8 and 653.7 eV) in L-PBMO.[28] Figure 2.10c shows two major peaks with binding energy at 710.2 and 723.9 eV, corresponding to Fe $2p_{3/2}$ and Fe $2p_{1/2}$, accompanied by two shake-up satellite peaks (718.6 and 732 eV) in L-PBMFO. The appearance of two peaks at 710 and 723.7 eV is Fe^{2+}, whereas the other two peaks at 712.5 and 725.5 eV are characteristic of Fe^{3+}. However, in the L-PBMCO, it is not easy to identify exact oxidation state of Co because binding energy peaks of Co 2p and Ba 3d main lines overlap each other (Figure 2.10d). From the XPS results, we can identify that Mn and Fe have no metallic phase in L-PBMO and L-PBMFO, respectively, which is also in agreement with our experimental results.

The effect of co-segregation energy on exsolution. A question that remains to be addressed is how the exsolution phenomenon occurs in layered perovskites. The exsolution phenomenon was confirmed in A-site deficient simple perovskites, where oxygen vacancies were introduced during reduction, which destabilizes the perovskite structure and results in spontaneous exsolution of B-site cation. We speculate

that spontaneous exsolution phenomenon occurs in layered perovskites when considerable amounts of oxygen vacancies and B-site metal vacancies could be introduced instantaneously (co-segregation) by reduction, and then the metal oxide can be converted to the corresponding metal or metal oxide (Figure 2.11). This mechanism of exsolution in layered perovskites is expressed as point defect (Schottky type defect) reactions as follows:

$$T_{Mn}^{\times} + O_O^{\times} \leftrightarrow TO + V_O^{\circ\circ} + V_{Mn}'' \quad (6)$$

$$TO \leftrightarrow T_{(metallic\ exsolution)} + \frac{1}{2}O_2 \quad (7)$$

where $T_{Mn}^{\times}$ denotes the B-site dopant in the Mn site with the net charge zero, $O_O^{\times}$ denotes oxygen in the oxygen site with the net charge zero, $V_O^{\circ\circ}$ denotes the oxygen ion vacancy with the net charge +2, V_{Mn}'' denotes the cation vacancy in the Mn site with the net charge -2, and TO denotes the transition metal oxide.

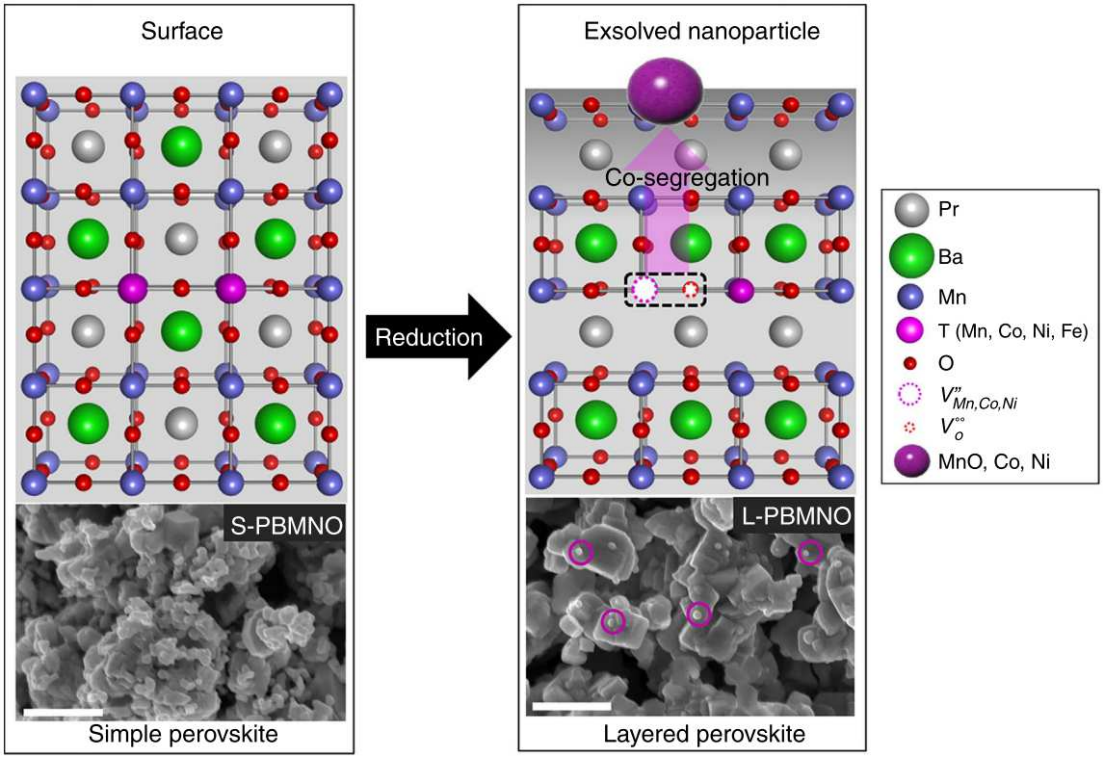

Figure 2.11. Exsolution of B-site cation with oxygen from layered perovskite in a reducing atmosphere. The SEM images present surface morphologies of $Pr_{0.5}Ba_{0.5}Mn_{0.85}Ni_{0.15}O_3$ before reduction and $PrBaMn_{1.7}Ni_{0.3}O_{5-\delta}$ after reduction in humidified (3% H_2O) H_2 at 800 °C for 4 h; scale bar 500nm. In the SEM image of $PrBaMn_{1.7}Ni_{0.3}O_{5-\delta}$, the purple circles indicate the exsolved nanoparticles.

Based on the XRD and TEM results, it appears that transition metals show different degrees of exsolution in the B-site of the layered perovskite. To verify the exsolution trends of B-site transition metals in the layered perovskite, we performed density functional theory (DFT) calculations. As mentioned above, it can be thought that the exsolution process occurs through two key sequential steps: [1] metal segregation toward the surface and [2] phase transition from the segregated phase to metallic phase.

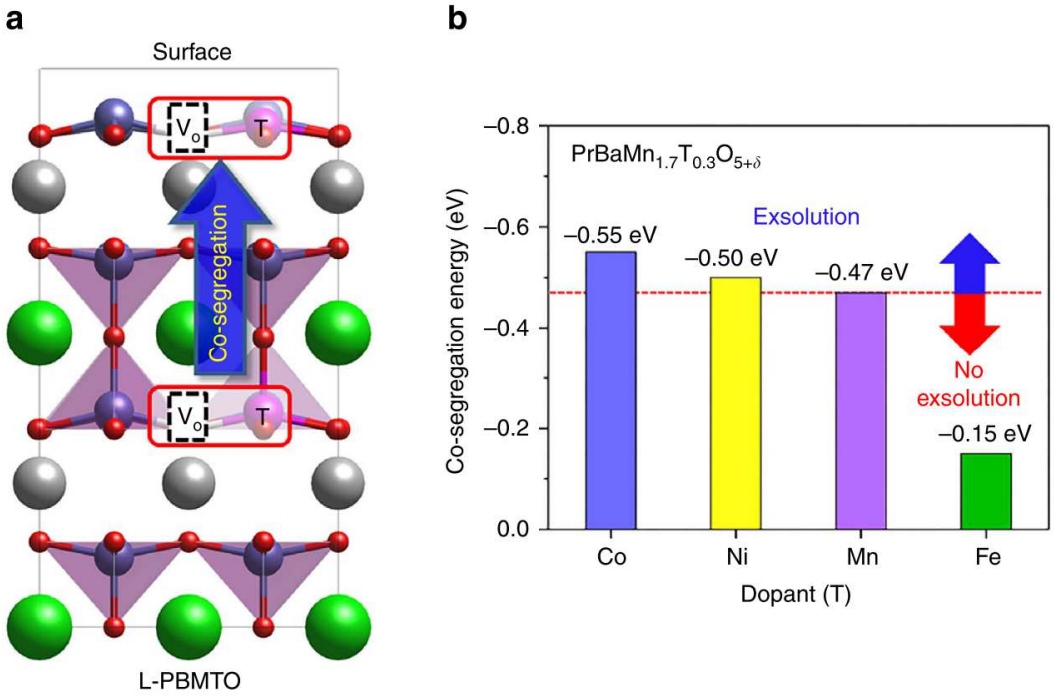

Figure 2.12. Density functional theory calculations for elucidating co-segregation energy. (a) Schematic illustration of our model used for the calculations of co-segregation energy. Pr, Ba, Mn, T (Mn, Co, Ni and Fe) and O atoms are shown as grey, green, dark blue, purple and red, respectively. The inset red boxes indicate the co-segregation of B-cation with an oxygen vacancy. (b) Comparison of the co-segregation energy with the dopant (T) materials.

To quantitatively compare the exsolution between the Mn (non-doped L-PBMO) and other B-site dopants (L-PBMCO, L-PBMNO, L-PBMFO), we calculated the co-segregation energy of B-site transition metal accompanying oxygen vacancies. This approach involves the assumption that the oxygen vacancy co-segregates with the nearby B-site metal towards the surface (Figure 2.12a). In a previous study, Hamada *et al*. performed DFT calculations to identify the role of the oxygen vacancy on precious metal (Pd, Pt, and Rh) exsolution.[29] The introduction of oxygen vacancies significantly enhanced the Pd exsolution, stabilizing the surfaces over a wide range of oxygen chemical potentials on $LaFe_xPd_{1-x}O_3$. Neagu *et al*. also reported that non-stoichiometry such as A-site deficiency facilitates

the formation of oxygen vacancies, which results in particle exsolution on $La_{\alpha}Sr_{1-\alpha}Ti_{\beta}Ni_{1-\beta}O_{3-\gamma}$ (LSTN) surfaces.[13] These studies imply that the creation of oxygen vacancies at the surfaces or bulk of the perovskite oxides is closely related to the exsolution of metal or metal oxide from the parent lattice. Since these considerations contain both the effect of B-site metal segregation and vacancy formation, it enables us to make a comprehensive comparison of the tendency of B-site transition metal exsolution. The co-segregation energies obtained by DFT calculations are -0.47 eV, -0.55 eV, -0.50 eV, and -0.15 eV for L-PBMO, L-PBMCO, L-PBMNO, and L-PBMFO, respectively (Figure 2.12b), indicating that Co and Ni more favourably exsolve towards the surface than Mn, and Fe less favourably exsolves than Mn.

Once the B-site metal and oxygen vacancy co-segregate toward the surface, stabilization of the segregated phase containing the B-site dopant on the surface is required to maintain the B-site dopant as metallic phase. For this, there should be a preference of oxygen vacancy formation near the B-site dopant compared to other sites. Therefore, we examined the oxygen vacancy formation at various lattice O sites in Figure 2.2. Our results showed that the most stable sites of oxygen vacancy formation in L-PBMO are near the surface (Table 2.2). Thus, the oxygen vacancy formed in the bulk prefers to be segregated out to the surface. Then, we compared the oxygen vacancy formation energy of B-site dopants at the surface of layered perovskites (Figure 2.13). The oxygen vacancy formation energies of the L-PBMCO (2.46 eV), L-PBMNO (2.85 eV), and L-PBMFO (2.91 eV) surfaces are lower than the L-PBMO surface (2.97 eV). This indicates that Co, Ni, and Fe create oxygen vacancies more easily than Mn at the surface, and consequently the segregated phase is also easily stabilized to the metallic phase in the following order: L-PBMCO > L-PBMNO > L-PBMFO > L-PBMO. However, L-PBMFO has lower co-segregation energy than L-PBMO as confirmed previously, it is expected that no exsolved metallic Fe nanoparticles exist on the surface of L-PBMFO, which is in good agreement with our experimental results.

	Oxygen vacancy formation energy (eV)
1 layer	2.97
3 layer	3.08
4 layer	3.72
5 layer	3.45

Table 2.2. Oxygen vacancy formation energies of L-PBMO at each layer.

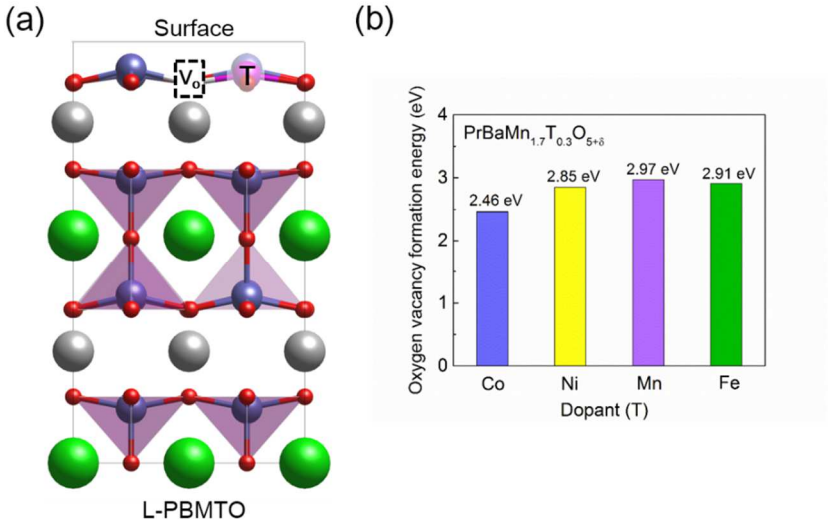

Figure 2.13. (a) Schematic of our model used for (b) the calculations of oxygen vacancy formation on the surfaces. Pr, Ba, Mn, T (Mn, Co, Ni, and Fe), and O atoms are shown as gray, green, dark blue, purple, and red, respectively. The inset box indicates the oxygen vacancy.

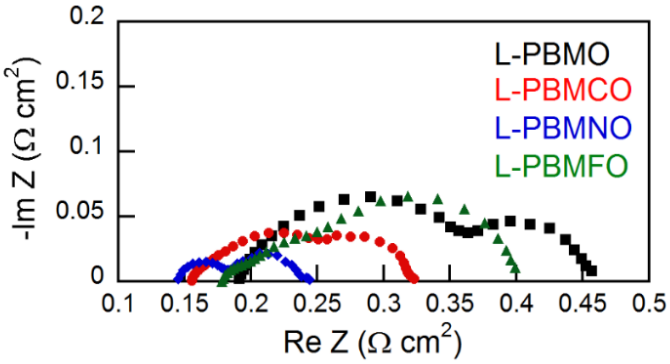

Figure 2.14. Impedance spectra of the L-PBMTO (T = Mn, Co, Ni, and Fe) measured in humidified (3% H_2O) H_2 at 800 °C.

Power output and durability of fuel cells. To confirm the catalytic effect of the exsolved nanoparticles, the electrochemical performance of single cells was tested using $La_{0.9}Sr_{0.1}Ga_{0.8}Mg_{0.2}O_{3-\delta}$ (LSGM) electrolyte supported cell in humidified H_2 (3% H_2O) as the fuel and ambient air as the oxidant with the configuration of L-PBMTO (T = Mn, Co, Ni, and Fe)/$La_{0.4}Ce_{0.6}O_{2-\delta}$ (LDC)/ LSGM/$NdBa_{0.5}Sr_{0.5}Co_{1.5}Fe_{0.5}O_{5+\delta}$-$Ce_{0.9}Gd_{0.1}O_{2-\delta}$ (NBSCF50-GDC). The electrochemical impedance spectra of single cell corresponding to the I-V polarization curve at 800 °C are presented in Figure 2.14 and Figure 2.15a. The non-ohmic resistances of L-PBMO, L-PBMCO, L-PBMNO, and L-PBMFO are 0.265, 0.167, 0.099, and 0.221 Ω cm^2 at 800 °C, respectively. In previous reports, exsolved Co and Ni nanoparticles increase the catalytic activation in fuel oxidation, which reduces the anode polarization

resistance.[9, 30] Therefore, the non-ohmic resistances of L-PBMCO and L-PBMNO are lower than L-PBMO and L-PBMFO. The maximum power densities of the L-PBMO, L-PBMCO, L-PBMNO, and L-PBMFO single cells are 0.661, 1.15, 1.12, and 0.690 W cm^{-2} at 800 °C in H_2, respectively. Figure 2.15b shows the I-V polarization curves of the L-PBMCO (0.331 W cm^{-2}) and L-PBMNO (0.322 W cm^{-2}) single cells in C_3H_8 at 800 °C. Table 2.3 shows the comparison of electrochemical performance of other ceramic anodes decorated with metal particles in hydrocarbon fuels. Furthermore, no remarkable degradation was observed under a constant voltage of 0.6 V at 700 °C in C_3H_8 (Figure 2.15c) and H_2 (Figure 2.16) for more than 200 h. It is worthwhile to point out that even though oxidation catalysts, such as Ce, Pt, and metal alloys, were not added into either of the electrodes from the outside, the exsolved nanoparticles on the surface of the ceramic anodes serve as a good fuel oxidation catalyst. Especially, the exsolved Co and Ni nanoparticles on the surface of the layered perovskite show excellent cell performance (1.15 and 1.12 W cm^{-2} at 800 °C in H_2, respectively) among developed ceramic anodes without adding any catalysts externally (Figure 2.15d and Table 2.4).[31-37]

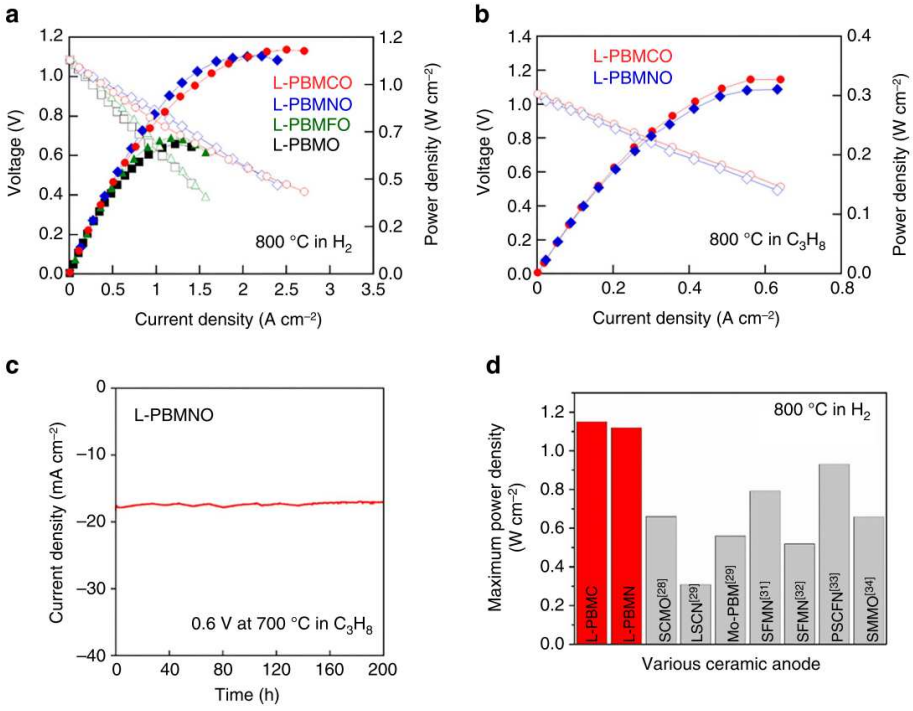

Figure 2.15. Electrochemical properties of layered $PrBaMn_{1.7}T_{0.3}O_{5-\delta}$ anode in fuel cells. (a) I–V curve and the corresponding power densities of the L-PBMTO (T = Mn, Co, Ni and Fe) electrode using humidified (3% H_2O) H_2 and ambient air as the oxidant at 800 °C. (b) I–V curve and the corresponding power densities of the $PrBaMn_{1.7}Co_{0.3}O_{5-\delta}$ (L-PBMCO) and $PrBaMn_{1.7}Ni_{0.3}O_{5-\delta}$ (L-PBMNO) electrode using C_3H_8 as fuel and ambient air as the oxidant at 800 °C. (c) Electrochemical performances of L-PBMNO anode in C_3H_8 at 700 °C under a constant voltage of 0.6V. (d) Comparison of the maximum power density at 800 °C in H_2 of the present work and other studies in the literature[31-37].

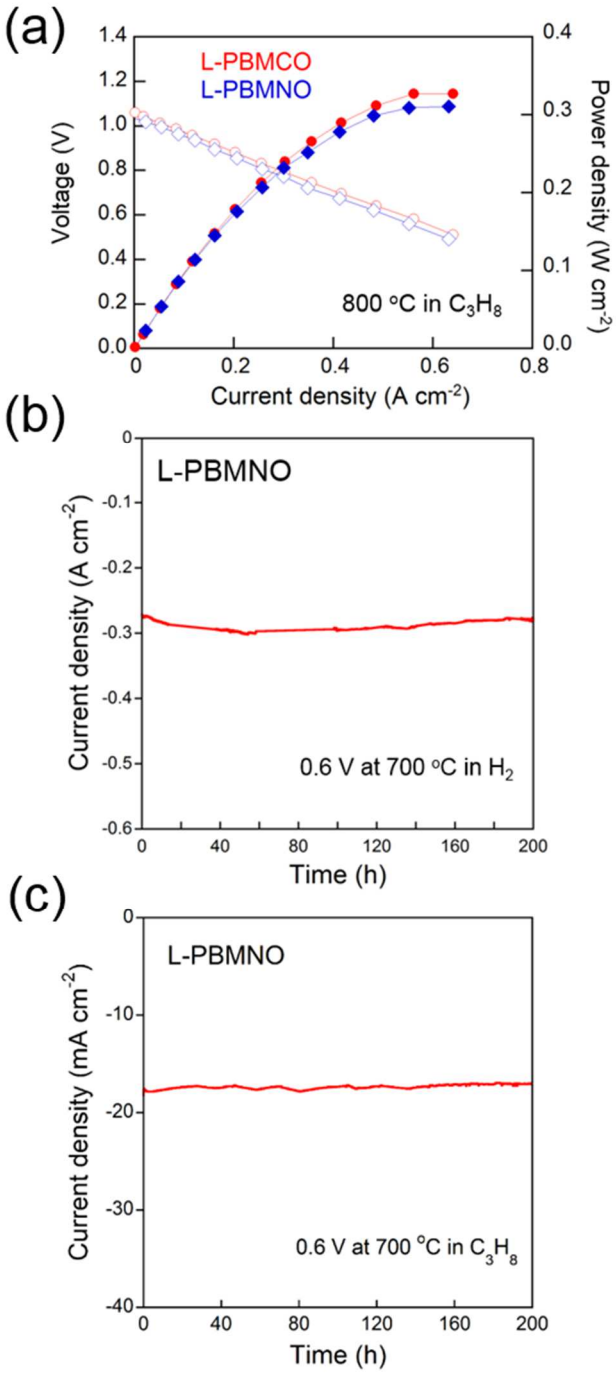

Figure 2.16. (a) I-V curve and the corresponding power densities of the L-PBMCO and L-PBMNO electrode using C_3H_8 as fuel and ambient air as the oxidant at 800 °C. Electrochemical performances of L-PBMNO anode in (b) H_2 and (c) C_3H_8 at 700 °C under a constant voltage of 0.6 V.

Cell configuration	Electrolyte thickness (μm)	Maximum power density (Wcm^{-2})	Ref
SCMO/SDC/LSGM/SCF	300	0.660	1
LSCN/YSZ/YSZ-LSM	100	0.309	2
Mo-PBMO/GDC/YSZ/LSCF	100	0.560	3
SFMNi/LDC/LSGM/LSCF	300	0.792	4
SFNM/LSGM/PBCO	200	0.520	5
PSCFN/LDC/LSGM/BCFN	300	0.930	6
SMMO/SDC/LSGM/BSCF	280	0.659	7
L-PBMCO/LDC/LSGM/NBSCF-GDC	250	1.15	This work
L-PBMNO/LDC/LSGM/NBSCF-GDC	250	1.12	This work

Table 2.3. Comparison of the performance of SOFC at 800 °C in H_2 reported in the present work and in the literature.

Cell configuration	Electrolyte thickness (μm)	Maximum power density (Wcm^{-2})	Temperature (°C)	Fuel	Ref
SFMNi/LDC/LSGM/LSCF	300	0.50	850	CH_4	4
A-LSCFe/YSZ/LSM	300	0.30	800	CH_4	8
LSCF//Ni–YSZ/YSZ/LSM	33	0.66	850	CH_4	9
PBMCo/YSZ/LSM	--	0.65	900	C_2H_4	10
K-PSCFN/LDC/LSGM/BCFN	300	0.60	850	CH_4	11
L-PBMCO/LDC/LSGM/NBSCF-GDC	250	0.33	800	C_3H_8	This Work
L-PBMNO/LDC/LSGM/NBSCF-GDC	250	0.32	800	C_3H_8	This Work

Table 2.4. Comparison of the performance of SOFC in hydrocarbon reported in the present work and in the literature.

2.4 Conclusions

In summary, the present work demonstrates the transition metal (Mn, Co, Ni, and Fe) exsolution trends for self-grown catalytic nanoparticle on a layered perovskite, which may be useful for the development of tailored functional materials. On the basis of DFT calculations, we proposed a possible mechanism for the exsolution of transition metals in layered perovskites, wherein co-segregation of B-site metal and oxygen vacancies plays a central role in the exsolution. We found that Co and Ni have high co-segregation energy (-0.55 eV and -0.50 eV) in the layered perovskite, which facilitates the exsolution of Co and Ni metal particles on the surface. The maximum power densities of an electrolyte supported cell with L-PBMCO and L-PBMNO anodes reached 1.15 and 1.12 W cm^{-2} in humidified H_2 at 800 ^oC, respectively, constituting excellent electrochemical performance as compared to other ceramic anodes. Our findings thus provide a key to understand the exsolution trends in transition metals (Mn, Co, Ni, and Fe) containing perovskites and design highly catalytic perovskite oxides for fuel reforming and electro-oxidation.

References

1. Sengodan, S. et al. Layered oxygen-deficient double perovskite as an efficient and stable anode for direct hydrocarbon solid oxide fuel cells. Nat. Mater. **14**, 205-209 (2015)
2. Huijben, M. et al. Electronically coupled complementary interfaces between perovskite band insulators. Nat. Mater. **5**, 556–560 (2006).
3. Yu, A. S. et al. Decreasing interfacial losses with catalysts in $La_{0.9}Ca_{0.1}FeO_{3-\delta}$ membranes for syngas production. Appl. Catal. A Gen. **486**, 259–265 (2014).
4. Jeon, N. J. et al. Solvent engineering for high-performance inorganic-organic hybrid perovskite solar cells. Nat. Mater. **13**, 897-903 (2014).
5. Kim, S. et al. Nanostructured Double Perovskite Cathode With Low Sintering Temperature For Intermediate Temperature Solid Oxide Fuel Cells. ChemSusChem **8**, 3153–3158 (2015).
6. Gorte, R. J. & Vohs, J. M. Nanostructured anodes for solid oxide fuel cells. Curr. Opin. Colloid Interface Sci. **14**, 236–244 (2009).
7. Schlupp, M. V. F., Evans, A., Martynczuk, J. & Prestat, M. Micro-solid oxide fuel cell membranes prepared by aerosol-assisted chemical vapor deposition. Adv. Energy Mater. **4**, 1301383 (2014).
8. Tanaka, H. et al. The intelligent catalyst having the self-regenerative function of Pd, Rh and Pt for automotive emissions control. Catal. Today **117**, 321–328 (2006).
9. Cui, S.-H. et al. Cobalt doped $LaSrTiO_{3-\delta}$ as an anode catalyst: effect of Co nanoparticle precipitation on SOFCs operating on H_2S-containing hydrogen. J. Mater. Chem. A **1**, 9689-9696 (2013).
10. Liu, S., Liu, Q. & Luo, J.-L. Highly Stable and Efficient Catalyst with In Situ Exsolved Fe-Ni Alloy Nanospheres Socketed on an Oxygen Deficient Perovskite for Direct CO_2 Electrolysis. ACS Catal. **6**, 6219-6228 (2016).
11. Sun, Y.-F. et al. New opportunity for in situ exsolution of metallic nanoparticles on perovskite parent. Nano Lett. 16, 5303-5309 (2016).
12. Neagu, D. *et al.* Nano-socketed nickel particles with enhanced coking resistance grown in situ by redox exsolution. *Nat. Commun.* **6**, 8120 (2015).
13. Neagu, D., Tsekouras, G., Miller, D. N., Ménard, H. & Irvine, J. T. S. *In situ* growth of nanoparticles through control of non-stoichiometry. *Nat. Chem.* **5**, 916–923 (2013).
14. Choi, S. *et al.* Highly efficient and robust cathode materials for low-temperature solid oxide fuel cells: $PrBa_{0.5}Sr_{0.5}Co_{2-x}Fe_xO_{5+\delta}$. *Sci. Rep.* **3**, 2426 (2013).
15. Yoo, S. *et al.* Development of double-perovskite compounds as cathode materials for Low-temperature solid oxide fuel cells. *Angew. Chem. Int. Ed.* **53,** 13064-13067 (2014).
16. Kim, J. *et al*. Triple-Conducting Layered Perovskites as Cathode Materials for Proton-Conducting Solid Oxide Fuel Cells. *ChemSusChem.* **7**, 2811–2815 (2014).

17. Jun, A., Kim, J., Shin, J. & Kim, G. Achieving High Efficiency and Eliminating Degradation in Solid Oxide Electrochemical Cells Using High Oxygen-Capacity Perovskite. *Angew. Chemie Int. Ed.* **55**, 12512-12515 (2016).
18. Sun, Y.-F., Li, J.-H., Zhang, Y.-Q., Hua, B. & Luo, J.-L. Bifunctional Catalyst of Core–Shell Nanoparticles Socketed on Oxygen-Deficient Layered Perovskite for Soot Combustion: *In Situ* Observation of Synergistic Dual Active Sites. *ACS Catal.* **6**, 2710–2714 (2016).
19. Motohashi, T. *et al.* Significant Lanthanoid Substitution Effect on the Redox Reactivity of the Oxygen-Storage Material $BaYMn_2O_{5+\delta}$. *Chem. Mater.* **28**, 4409–4414 (2016).
20. Kresse, G. & Furthmüller, J. Efficient iterative schemes for ab initio total-energy calculations using a plane-wave basis set. Phys. Rev. B. 54, 11169 (1996).
21. Monkhorst, H. J. & Pack, J. D. Special points for Brillouin-zone integrations. Phys. Rev. B. 13, 5188-5192 (1976).
22. Kirklin, S. et al. The Open Quantum Materials Database (OQMD): assessing the accuracy of DFT formation energies. npj Computational Materials. 1, 15010 (2015).
23. Schmid, H. K. & Mader, W. Oxidation states of Mn and Fe in various compound oxide systems. Micron. 37, 426–432 (2006).
24. Tan, H., Verbeeck, J., Abakumov, A. & Van Tendeloo, G. Oxidation state and chemical shift investigation in transition metal oxides by EELS. Ultramicroscopy 116, 24–33 (2012).
25. Svoboda, K., Siewiorek, A., Baxter, D., Rogut, J. & Punčochář. Thermodynamic Possibilities and Constraints of Pure Hydrogen Production by a Chromium , Nickel , and Manganese-Based Chemical Looping Process at Lower Temperatures. Chemical Papers. 61, 110-120 (2007).
26. Svoboda, K., Siewiorek, A., Baxter, D., Rogut, J. & Pohořelý, M. Thermodynamic possibilities and constraints for pure hydrogen production by a nickel and cobalt-based chemical looping process at lower temperatures. Energy Convers. Manag. 49, 221–231 (2008).
27. Zahmakıran, M. et al. Zeolite framework stabilized nickel(0) nanoparticles: Active and long-lived catalyst for hydrogen generation from the hydrolysis of ammonia-borane and sodium borohydride. Catal. Today. 170, 76-84 (2011).
28. Zheng, F., Zhu, D., Shi, X. & Chen, Q. Metal–organic framework-derived porous $Mn_{1.8}Fe_{1.2}O_4$ nanocubes with an interconnected channel structure as high-performance anodes for lithium ion batteries. J. Mater. Chem. A. 3, 2815-2824 (2015).
29. Hamada, I., Uozumi, A., Morikawa, Y., Yanase, A. & Katayama-Yoshida, H. A Density Functional Theory Study of Self-Regenerating Catalysts LaFe1-xMxO3-y (M = Pd, Rh, Pt). J. Am. Chem. Soc. 133, 18506–18509 (2011).
30. Gao, Y., Chen, D., Saccoccio, M., Lu, Z. & Ciucci, F. From material design to mechanism study: Nanoscale Ni exsolution on a highly active A-site deficient anode material for solid oxide fuel cells.

Nano Energy. 27, 499–508 (2016).

31. Wei, T., Zhang, Q., Huang, Y.-H. & Goodenough, J. B. Cobalt-based double-perovskite symmetrical electrodes with low thermal expansion for solid oxide fuel cells. J. Mater. Chem. 22, 225-231 (2012).
32. Sun, Y. et al. A-site deficient perovskite: the parent for in situ exsolution of high-active, regenerable nano-particles as SOFCs anode. J. Mater. Chem. A. 3, 11048-11056 (2015).
33. Sun, Y. F. et al. Molybdenum doped $Pr_{0.5}Ba_{0.5}MnO_{3-\delta}$ (Mo-PBMO) double perovskite as a potential solid oxide fuel cell anode material. J. Power Sources 301, 237–241 (2016).
34. Du, Z. et al. High-Performance Anode Material $Sr_2FeMo_{0.65}Ni_{0.35}O_{6-\delta}$ with In Situ Exsolved Nanoparticle Catalyst. ACS Nano. 10, 8660-8669 (2016).
35. Ding, H., Tao, Z., Liu, S. & Yang, Y. A redox-stable direct-methane solid oxide fuel cell (SOFC) with $Sr_2FeNb_{0.2}Mo_{0.8}O_{6-\delta}$ double perovskite as anode material. J. Power Sources 327, 573–579 (2016).
36. Yang, C. et al. In situ fabrication of CoFe alloy nanoparticles structured $(Pr_{0.4}Sr_{0.6})_3(Fe_{0.85}Nb_{0.15})_2O_7$ ceramic anode for direct hydrocarbon solid oxide fuel cells. Nano Energy. 11, 704–710 (2015).
37. Jiang, L., Liang, G., Han, J. & Huang, Y. Effects of Sr-site deficiency on structure and electrochemical performance in Sr_2MgMoO_6 for solid-oxide fuel cell. J. Power Sources 270, 441–448 (2014).

Chapter 3. Self-assembled alloy nanoparticles in a layered double perovskite as a fuel oxidation catalyst for solid oxide fuel cells

This chapter has been published

Reproduced from Kwon, O.; Kim, K.; Joo, S.; Jeong, H. Y.; Shin, J.; Han, J. W.; Sengodan, S.; Kim, G. Self-assembled alloy nanoparticles in a layered double perovskite as a fuel oxidation catalyst for solid oxide fuel cells. *J. Mater. Chem. A* **2018**, *6*, 15947-15953 DOI: 10.1039/C8TA05105D, by permission of The Royal Society of Chemistry.

3.1 Introduction

Perovskite oxides (ABO_3) characterize an interesting and versatile structural family, in which all the transition and rare earth metals have been incorporated. Therefore, intensive researches have been focused on perovskite oxides due to their compositional and structural flexibility in the field of solid oxide fuel cells (SOFCs)[1–3], partial oxidation membranes[4], metal air batteries[5], and other applications[6]. The modification of physical and chemical properties by doping strategy signifies one of the main areas in perovskite research. However, the electrochemical performance of these doped perovskites is still inferior to the metal/metal oxide-based materials. Recent studies have shown that the performance of perovskite electrodes in SOFCs can be greatly improved by decorating the perovskite surface with catalytic metal/metal oxide nanoparticles.[7,8]

An exsolution, *in situ* formation of catalytic nanoparticles on the perovskite surface in reducing atmosphere, has attracted intense attention for making catalysts.[9–11] Various catalytic transition metals can be incorporated on B-site of the perovskite oxide in air synthesis process and exsolved from the parent perovskite under the reducing atmosphere.[12] The exsolved nanoparticles are socketed on the perovskite surface, preventing agglomeration of the nanoparticles and enhancing carbon coking tolerance.[13] Although several perovskite electrode materials have been developed by exsolution approach, most of the exsolution approaches have generally been performed to exsolve single metal from the simple perovskite lattice. In addition, comprehensive characterizations for exsolution of intermetallic compounds (referred as alloys) have not been clearly reported, but have only focused on the simple perovskites.[14,15] Indeed, the mechanism of alloy formation for the entire perovskite family is still an open question in terms of experimental observations and theoretical calculations.

The goal of this work is to respond to this lack of information and to resolve this gap through detailed investigation of catalytic alloy nanoparticles exsolved from a layered double perovskite. Also, there is a need for characterization of phase stability, phase transition at atomic levels, and alloy formation energies, which is essential for understanding various physical and chemical properties of alloy nanoparticles. Previously, we demonstrated the exsolution trends of transition metals (Co, Ni, Fe, and

Mn) in $PrBaMn_2O_{5+\delta}$ (PBMO) layered double perovskite oxide.[16] Among the transition metals, we selected Co and Ni for the alloy system because Co and Ni have high co-segregation energies (Co = -0.55 eV and Ni = -0.50 eV) for exsolution compared to Fe (-0.15 eV) and Mn (-0.47 eV). In the process of alloy exsolution, Gibbs free energies of alloy formation at the surface and in the bulk, are -0.01 eV and +0.02 eV, respectively, indicating that alloy formation takes place more favorable at the surface than in the bulk. Combining theoretical calculation and experimental observation, we find that Co and Ni are exsolved separately from the bulk, and then aggregated to form Co-Ni alloy at the surface. The Co-Ni alloy nanoparticles decorated on $PrBaMn_{1.7}Co_{0.1}Ni_{0.2}O_{5+\delta}$(PBMCNO) oxide surface show higher catalytic activity towards dry reforming of methane, fuel oxidation in fuel cells (0.97 W cm^{-2} at 800 ^oC), and stability (>500 h at 800 ^oC).

3.2 Experimental

$Pr_{0.5}Ba_{0.5}Mn_{0.85}Co_{0.05}Ni_{0.1}O_3$ powder was prepared by the Pechini method. Stoichiometric amounts of $Pr(NO_3)_3{\cdot}6H_2O$ (Aldrich, 99.9%, metal basis), $Ba(NO_3)_2$ (Aldrich, 99+%), $Mn(NO_3)_2{\cdot}4H_2O$ (Aldrich, 98%), $Co(NO_3)_2{\cdot}6H_2O$ (Aldrich, 98+%), and $Ni(NO_3)_2{\cdot}6H_2O$ (Aldrich, 98.5+%) were dissolved in distilled water with proper amounts of ethylene glycol and citric acid, followed by combustion to obtain fine powders. This powder was calcined at 600 ^oC for 4h and then sintered at 950 ^oC for 4h in air. The A-site layered $PrBaMn_{1.7}Co_{0.1}Ni_{0.2}O_{5+\delta}$ (PBMCNO) was obtained by annealing $Pr_{0.5}Ba_{0.5}Mn_{0.85}Co_{0.05}Ni_{0.1}O_3$ oxide at 850 ^oC for 4h in humidified H_2.

The crystal structures of the samples were identified by X-ray powder diffraction (XRD) (Bruker D8 advance, Cu Ka radiation, 40 kV, 30 mA). *In situ* XRD was measured in H_2 at temperatures between 600-850 ^oC (Bruker D8 advance). The morphologies of the anode materials were investigated using a field emission scanning electron microscope (SEM). Transmission electron microscopy (TEM) images were obtained by a JEOL JEM 2100F with a probe forming (STEM) Cs (spherical aberration) corrector at 200 kV. The redox properties and oxygen non-stoichiometry of PBMCNO were measured using coulometric titration (CT) as a function of temperature. The sample was located inside an oxygen ion (O^{2-}) conducting YSZ tube (Z15410630, McDanel Advanced Ceramic Techonologies). Ag paste was painted on the inner and outer sides of the YSZ tube as electrodes. The Ag electrodes on both sides of the tube are alternatively used for pumping in/out oxygen and to measure the potential across the tube. The potential across the tube is driven by the ratio of the pO_2 inside and outside the cell according to the Nernst equation.

Catalytic activity of PBMCNO for dry reforming reaction was evaluated through gas chromatography (GC) (Agilent 2820A GC instrument) with a thermal conductivity detector (TCD) and a packed column (Agilent carboxen 1000). The gas used for GC measurement were controlled using a mass flow controller (MFC) (Atovac GMC1200) and the exact volume value of gas was calibrated through a bubble

flow meter. Sample powder (950 ºC air sintering) was prepared and 0.2 g of powder was packed in the middle of the quartz tube reactor using glass wool. The sample powder was in-situ reduced at 900 ºC for 30 minutes while blowing humidified H_2 (3% H_2O) gas in a quartz tube reactor. After reduction, the reactor was purged for 1 hour with He gas before each measurement to remove residual H_2, then CO_2, CH_4, and He were inserted with a ratio of 20:20:60 ml min^{-1}, respectively. The dry reforming reaction is shown as below, CO_2 conversion and CO selectivity are calculated using the following equation.[17]

$$CH_4+CO_2 \leftrightarrow 2CO+2H_2 \ (\Delta H^0_{298K}=247 \text{ kJ/mol})$$

$$\text{CO}_2 \text{ conversion} = \frac{[CO_2]_{consumed}}{[CO_2]_{inserted}} \times 100\% = \frac{[CO]_{detect}}{[CO]_{detect} + 2[CO_2]_{detect}} \times 100\%$$

$$\text{CO selectivity} = \frac{[CO]_{detect}}{[CO]_{detect} + [CO_2]_{detect}} \times 100\%$$

We carried out DFT calculations using the Vienna Ab initio Simulation Package (VASP).[18] Exchange-correlation energies were treated by Perdew-Burke-Ernzerhof (PBE) functional based on generalized gradient approximation (GGA). An energy cutoff of 400 eV was used for plane-wave expansion. A 3 × 3 × 1 Monkhorst-Pack k-point sampling of the Brillouin zone was used for all slab model calculations.[19] Gaussian smearing was used with a width of 0.05 eV to determine partial occupancies. Geometries were relaxed using a conjugate gradient algorithm until the forces on all unconstrained atoms were less than 0.03 eV/Å. To consider for on-site Coulomb and exchange interactions, we used GGA+U schemes with the effective U values of 4.0, 3.3, and 6.4 for Mn, Co, and Ni, respectively. 8 layered PBMO slab model was constructed with the vacuum thickness of up to 17 Å in the z-direction by cleaving a bulk PBMO structure.[16] The dopant position at top surface or in 5th layer represents that it is located at surface or in bulk, respectively. To describe the alloy formation, we substituted two Mn atoms with Co or Ni atom in PBMO. More calculation details for Gibbs free energies of B-site metal aggregation and segregation are described in Figure 3.1. A single cell with a configuration of PBMCNO/$La_{0.4}Ce_{0.6}O_{2-\delta}$ (LDC)/$La_{0.9}Sr_{0.1}Ga_{0.8}Mg_{0.2}O_{3-\delta}$ (LSGM)/$NdBa_{0.5}Sr_{0.5}Co_{1.5}Fe_{0.5}O_{5+\delta}$-$Ce_{0.9}Gd_{0.1}O_{2-\delta}$ (NBSCF50-GDC) was fabricated based on 250 μm LSGM electrolyte supported cells to measure the electrochemical performance. The LSGM electrolyte powder was pelletized and sintered at 1475 ºC for 5h in air. To prevent inter-diffusion of ions between the anode and the electrolyte, the LDC buffer layer was located between the anode and the electrolyte. The NBSCF50-GDC cathode and the anode slurries were screen-printed onto both sides of the LSGM electrolyte, and then sintered at 950 ºC for 4h in air. Ag wires were attached at both electrodes of the single cell using Ag paste as a current collector. Ceramic adhesive (Aremco, Ceramabond 553) and an alumina tube were used to seal the single cell. Humidified hydrogen (3% H_2O) was used at the anode side as fuel through a water bubbler with a flow rate of 100 mL min^{-1} and ambient air was applied as an oxidant during single cell tests. Impedance spectra and I-V curves

were measured using a BioLogic Potentiostat at the operating temperature.

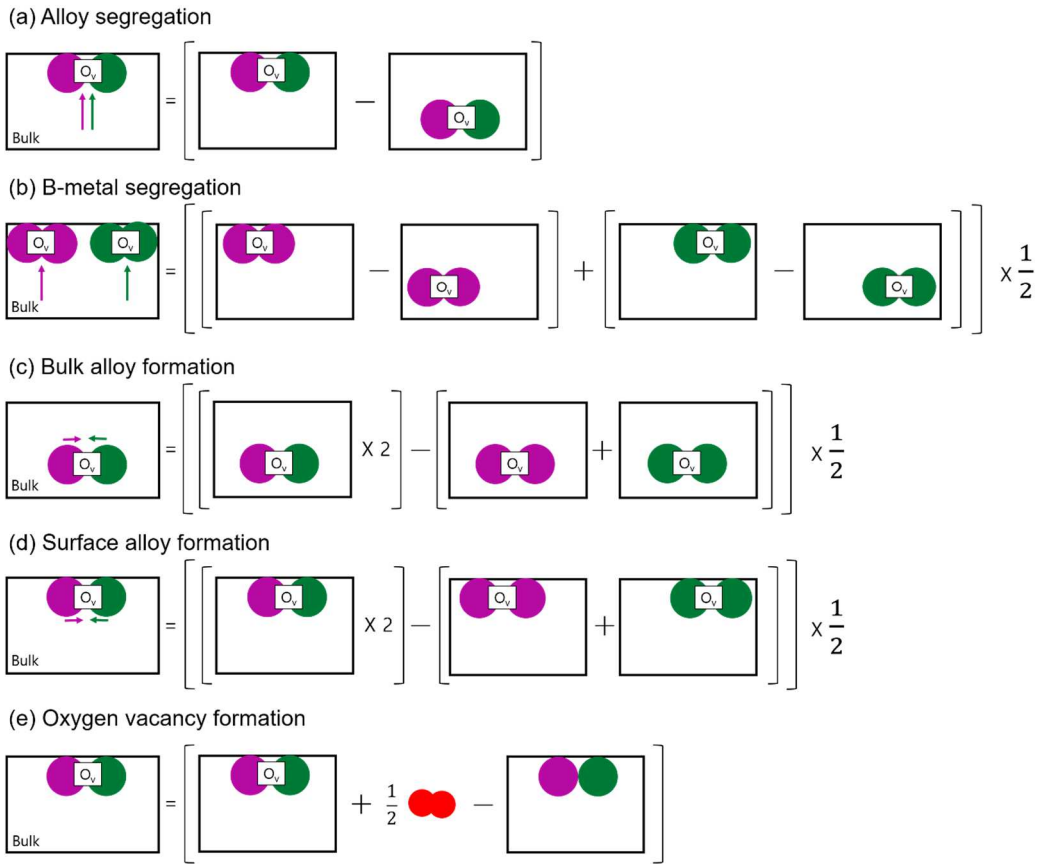

Figure 3.1 Schematic illustration for DFT-calculated energetics at each elementary step. (a) The alloy segregation energy was defined by the total energy difference between the systems with Co-O_v-Ni alloy located at surface and in bulk. (b) To compare the segregation energy of Co-O_v-Ni alloy with the separate segregation of Co-O_v-Co and Ni-O_v-Ni, we used the normalized segregation energies of Co-O_v-Co and Ni-O_v-Ni. The alloy formation energies (c) in the bulk and (d) at the surface were defined by the total energy difference between the systems where two different B-site metals are separated and aggregated. (e) The oxygen vacancy formation energy was defined by total energy difference of the supercells with and without an oxygen vacancy.

3.3 Results and Discussions

X-ray diffraction (XRD) technique was used to confirm the crystalline structures of the oxide materials before and after reduction. As shown in Figure 3.2a, diffraction pattern for $Pr_{0.5}Ba_{0.5}Mn_{0.85}Co_{0.05}Ni_{0.1}O_3$ sintered at 950 ºC in air presents a simple perovskite structure with a mixture of hexagonal and cubic phases[16, 20, 21]. Figure 3.2b shows the diffraction pattern of $PrBaMn_{1.7}Co_{0.1}Ni_{0.2}O_{5+\delta}$ (PBMCNO) after reduction at 850 ºC in H_2. The reduced PBMCNO has a layered double perovskite structure with a metal phase, indicating that the phase transition from simple perovskite to layered double perovskite and metal exsolution occur simultaneously in the reducing atmosphere. Apparently, the peak labelled as "▼" in Figure 3.2b is assigned to the diffraction peak for Co-Ni metal alloy which is *in situ* exsolved from the layered double perovskite backbone. The surface morphologies of the oxide materials were investigated by scanning electron microscopy (SEM). As shown in Figure 3.2c, the surface of the $Pr_{0.5}Ba_{0.5}Mn_{0.85}Co_{0.05}Ni_{0.1}O_3$ (before reduction) sample is smooth without any detectable nanoparticles. On the other hand, many small nanoparticles of 20-50 nm diameter are observed on the surface of the reduced sample in Figure 3.2d.

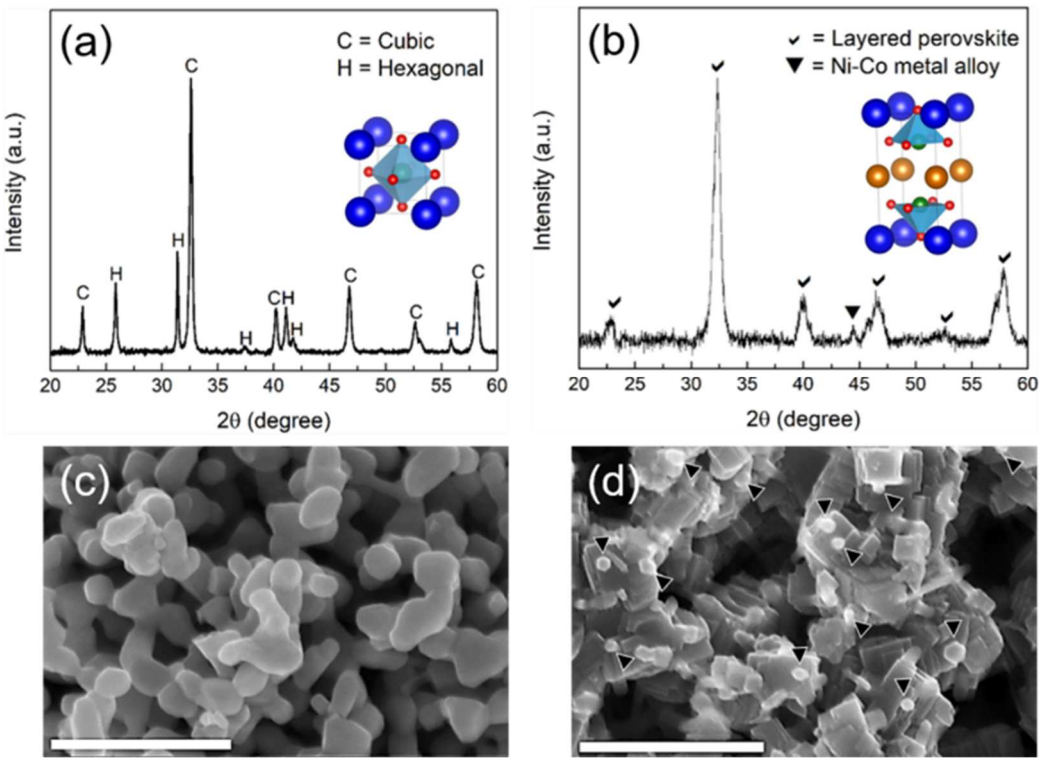

Figure 3.2. X-ray diffraction patterns of (a) $Pr_{0.5}Ba_{0.5}Mn_{0.85}Co_{0.05}Ni_{0.1}O_3$ sintered at 950 ºC for 4h in air and (b) PBMCNO after reduction at 850 ºC for 4h in humidified (3% H_2O) H_2. Scanning electron microscope images of (c) $Pr_{0.5}Ba_{0.5}Mn_{0.85}Co_{0.05}Ni_{0.1}O_3$ and (d) PBMCNO; scale bar 400 nm. In the SEM image of PBMCNO, the black triangles indicate the exsolved nanoparticles

To obtain further information of exsolved nanoparticles, high-resolution transmission electron microscopy (HR-TEM) and energy dispersive X-ray spectroscopy (EDS) were conducted. The EDS result shows that Co and Ni elements coexist on the surface of PBMCNO (Figure 3.3a), implying that Co-Ni alloy nanoparticles are exsolved in reducing atmosphere. In the bright-field and high-resolution TEM image of PBMCNO (Figure 3.3b and 3.3c), it is observed that some nanoparticles possessing 40 nm diameter are socketed on the PBMCNO surface. The lattice space between planes of the exsolved nanoparticle is 0.127 nm (Figure3.3d), and this value is consistent with the lattice constant of (220) planes of Co-Ni metal alloy. Meanwhile, in the attempt to produce Co-Fe alloy in Co and Fe co-doped PBMO layered double perovskite, only a Co exsolution, not Fe or Co-Fe exsolution, was observed (Figure 3.4). This agrees with our previous study on the exsolution trends and is due to a low co-segregation energy of Fe in layered double perovskite system. In sharp contrast, the Fe metal alloys can easily exsolved in simple perovskite oxides (ABO_3) such as $Sr_{0.95}(Ti_{0.3}Fe_{0.63}Ni_{0.07})O_{3-\delta}$ and $La_{0.6}Sr_{0.4}Fe_{0.8}Ni_{0.2}O_{3-\delta}$ under the same experimental conditions, which is quite different from this report.[14, 22]

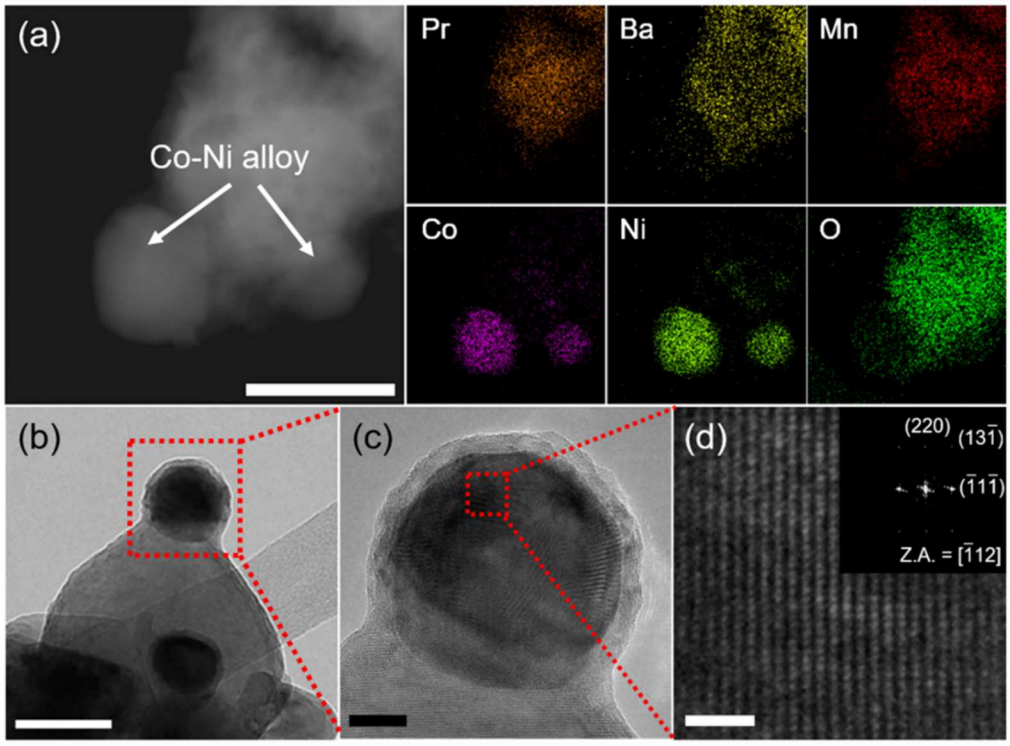

Figure 3.3. Transmission electron microscopy analysis. (a) High-angle annular dark-field (HAADF) image of the PBMCNO with the EDS elemental map of Pr, Ba, Mn, Co, Ni, and O; scale bar 100 nm. (b) A bright-field (BF) TEM image; scale bar, 50 nm and (c) high-resolution (HR) TEM image of PBMCNO; scale bar 10 nm. (d) Magnified HR TEM image of exsolved Co-Ni alloy nanoparticle; scale bar 1 nm.

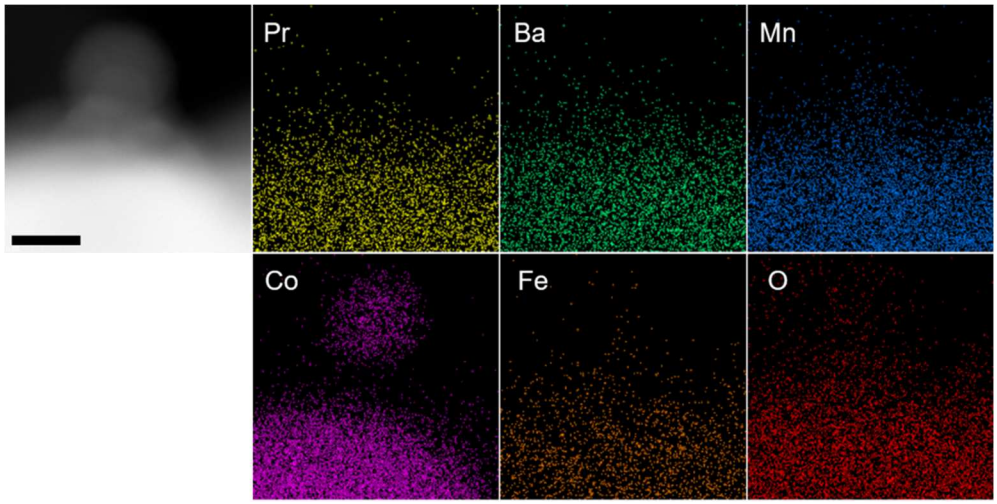

Figure 3.4. High-angle annular dark-field (HADDF) image of the $PrBaMn_{1.7}Co_{0.1}Fe_{0.2}O_{5+}$ with the EDS elemental map of Pr, Ba, Mn, Co, Fe, and O; scale bar 25 nm.

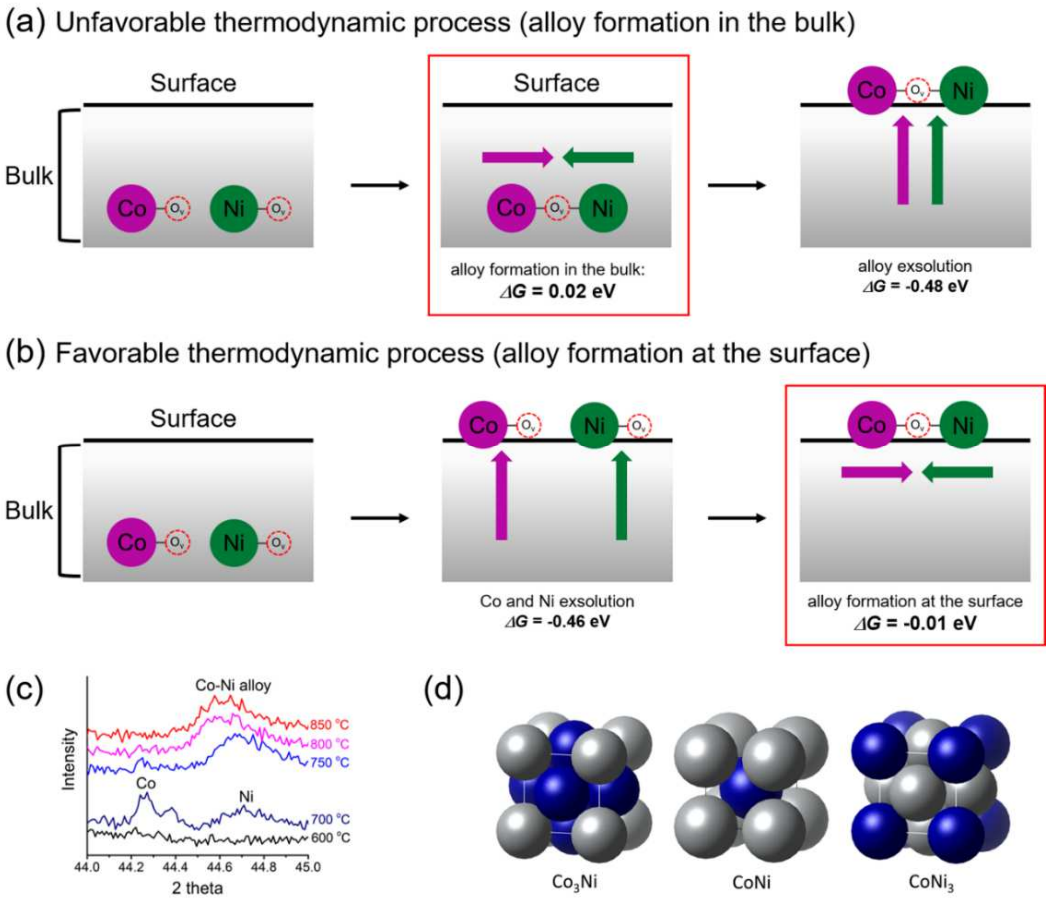

Figure 3.5. Schematic illustrations and energetics of (a) bulk alloy formation and (b) surface alloy formation for the exsolution of alloy nanoparticles. (c) In situ XRD patterns of PBMCNO in humidified (3% H_2O) H_2 at various temperatures. (d) Optimized alloy structures of Co_3Ni, CoNi, and $CoNi_3$ that we used for DFT calculations in this study.

Generally, most metals are immiscible with each other over a wide temperature range, and thus metallurgical high temperature methods are required to form bimetallic alloys.[23] However, the catalytic alloy nanoparticles prepared by conventional methods will tend to agglomerate at high temperature (above 600 °C), which increases particle size and reduces surface area. From the TEM results, we can identify that exsolution is an efficient method to overcome the problems associated with agglomeration of conventional nano-catalyst in metal/metal oxide system at high temperature, because exsolved nanoparticles have high tolerance to agglomerate due to their special surface morphology in which nanoparticles are well anchored and socketed.[1]

To form the exsolved Co-Ni alloy nanoparticles, it can be reasonably thought that both the aggregation of two doped B-metals and their segregation toward the surface should occur simultaneously. However, the detailed mechanism for such phenomena is quantitatively unclear. To obtain a better understanding of the mechanism, two possible mechanisms of "Bulk alloy formation" and "Surface alloy formation" were investigated as shown in Figure 3.5a and 3.5b. Here, we focused on the thermodynamic tendency to aggregate and segregate a pair of metals. The bulk alloy (Co-O_v-Ni) formation starts with the aggregation of Co-O_v-Co and Ni-O_v-Ni in the bulk of PBMCNO by locating each B metal into the nearest neighbor site with sharing an oxygen vacancy. Then, the Co-O_v-Ni segregates toward the surface, which is essentially equivalent to the definition of co-segregation used in our previous work.[2] On the other hand, the surface alloy (Co-O_v-Ni) formation starts with the independent segregation of each pair of Co-O_v-Co and Ni-O_v-Ni toward the surface. It is then followed by the aggregation of Co-O_v-Co and Ni-O_v-Ni to form a nearest neighbored Co-O_v-Ni on the surface of PBMCNO. Although the initial and final states are the same for both pathways, the required energies for each step are quite different. The Gibbs energies of aggregation (ΔG_{aggr}) of Co-O_v-Ni at the surface (surface alloy formation) and in the bulk (bulk alloy formation) are −0.01 and 0.02 eV, respectively, indicating that Co and Ni are more favorable to aggregate at the surface than in the bulk. Meanwhile, the Gibbs energies for co-segregation (ΔG_{seg}) of Co, Ni, and Co-Ni with an oxygen vacancy are exothermic (−0.53, −0.39, and −0.48 eV, respectively), which is thermodynamically favorable for all cases. Thus, we can conclude that the alloy formation is much harder than the metal segregation, and "surface alloy formation" is preferred to "bulk alloy formation" with no apparent thermodynamic energy requirement. Experimentally, to confirm the progress of alloy exsolution, the $Pr_{0.5}Ba_{0.5}Mn_{0.85}Co_{0.05}Ni_{0.1}O_3$ sample prepared in air was examined by *in situ* XRD in humidified H_2 (3% H_2O) during elevating temperature. As shown in Fig. 3c, the peaks of metallic cobalt located at 44.25° (JCPDS card # 15-0806) and metallic nickel located at 44.7° (JCPDS card # 04-0850) were observed at 700 °C, and then the two peaks were merged to form a single peak at temperature above 750 °C. Therefore, this *in situ* XRD results confirm the mechanism of the surface alloy formation.

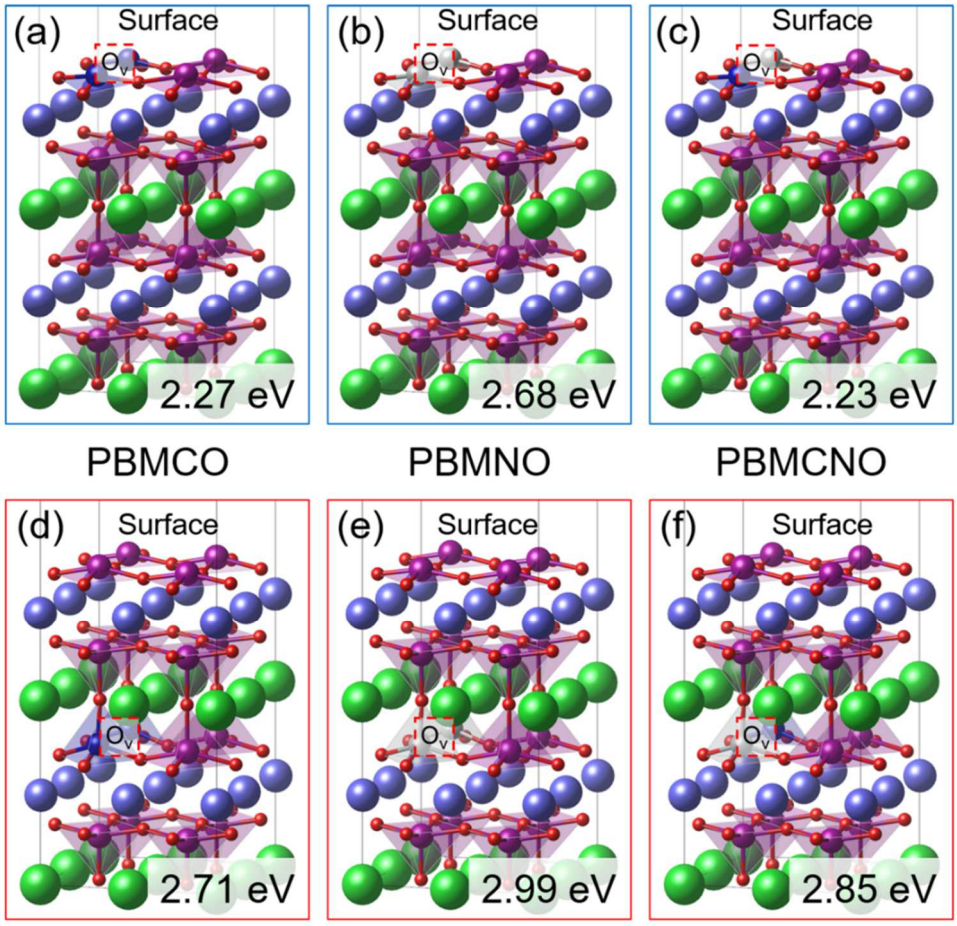

Figure 3.6. Oxygen vacancy formation energies (a)-(c) at the surface or (d)-(f) in the bulk of Co, Ni, and Co-Ni doped PBMO, respectively. Pr, Ba, Mn, Co, Ni, and O atoms are shown as dark blue, green, purple, blue, grey, and red, respectively. The Ov in red rectangular indicates an oxygen vacancy.

For the stability of exsolved nanoparticles as metallic phase after co-segregation of B-site metal and oxygen vacancy, a preference of oxygen vacancy formation near the segregated B-site metals should be necessary.[24] Therefore, we examined the oxygen vacancy formation energy (E_{vf}) at various surface lattice O sites. Our results show that the most stable sites of oxygen vacancies are located at between the two B-metal atoms such as Co-O_v-Co, Ni-O_v-Ni, and Co-O_v-Ni at surface and in bulk (Figure 3.6). In addition, oxygen vacancies are more easily formed at surface (E_{vf} = 2.97, 2.27, 2.68, and 2.23 eV for PBMO, $PrBaMn_{1.7}Co_{0.3}O_{5+\delta}$(PBMCO), $PrBaMn_{1.7}Ni_{0.3}O_{5+\delta}$ (PBMNO), and PBMCNO, respectively) than in bulk (E_{vf} = 3.72, 2.71, 2.99, and 2.85 eV for PBMO, PBMCO, PBMNO, and PBMCNO, respectively). Especially, PBMCNO shows the lowest oxygen vacancy formation energy at the surface, implying that the Co-Ni aggregation significantly stabilizes an oxygen vacancy near the surface. The oxygen vacancies are easily formed near the Co-Ni aggregation that would be easily transformed to the metallic phase of Co-Ni alloy nanoparticles. In addition, the aggregation energy of Co-Ni at the surface

is 0.23 eV without an oxygen vacancy, which is unfavorable than that of Co-Ni at the surface (-0.01 eV) with an oxygen vacancy (Co-O_v-Ni). This supports that the surface oxygen vacancy stabilizes the formation of Co-Ni alloy. In this regard, similar results have been reported that the introduction of surface oxygen vacancies significantly enhances the B-metal exsolution as well as stabilizes surface by changing hybridized states of segregated atom.[16, 24, 25] Consequently, on the PBMCNO surface, oxygen vacancies would be more accumulated near the segregated Co-Ni due to relatively lower E_{vf} (2.23 eV) than the host Mn (2.97 eV), which results in both facile formation and stabilization of metallic exsolved alloy nanoparticles.

Furthermore, the formation energies of Co-Ni alloys were also investigated to determine whether the formation of alloys depends on intrinsic cohesion characteristics between Co and Ni (Figure 3.5d). We examined the alloy formations of Co_3Ni, CoNi, and $CoNi_3$ in their most stable crystalline states of FCC, BCC, and FCC with the equilibrium lattice constants of 3.500, 2.802, and 3.520 Å, respectively.[26, 27] The Gibbs energies of alloy formation for Co_3Ni, CoNi, and $CoNi_3$ are all positive numbers (0.10, 0.41, and 0.18 eV, respectively), which means that Co-Ni alloy formation without PBMO is thermodynamically unfavorable compared to both the surface and bulk alloy pathways in PBMCNO. Therefore, to induce thermodynamically favorable alloy nanoparticles, it is very important to find valuable support materials such as the PBMO.

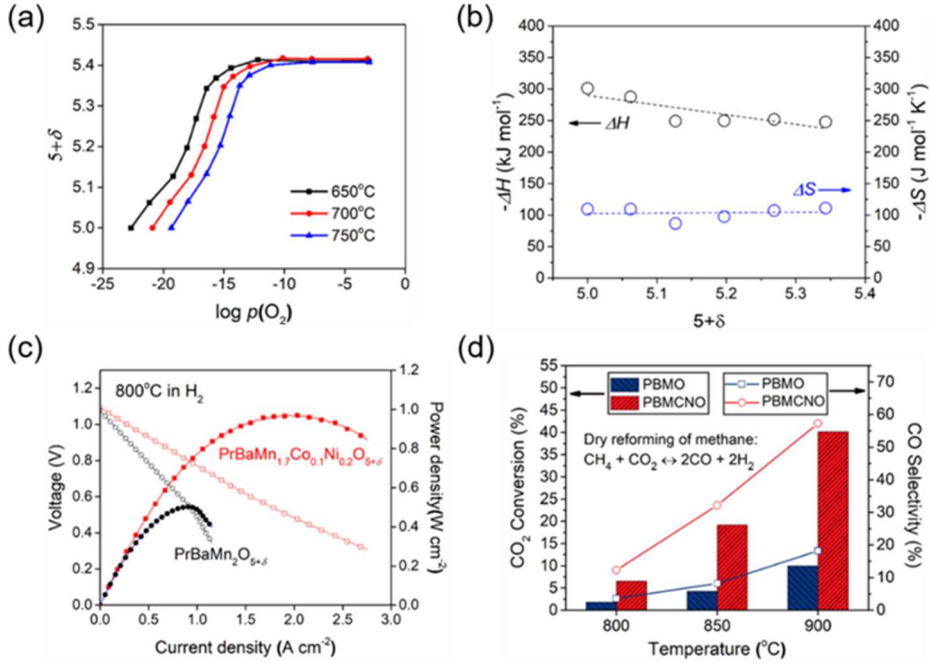

Figure 3.7. (a) Oxygen non-stoichiometry of PBMCNO as a function of $p(O_2)$ at 650, 700, and 750 °C. (b) Partial molar enthalpy (ΔH) and partial molar entropy (ΔS) of PBMCNO. (c) I-V curve and corresponding power densities of the fuel cells with PBMO and PBMCNO anodes using humidified (3% H_2O) H_2 as the fuel and ambient air as the oxidant at 800 °C. (d) Conversion of CO_2 and selectivity of CO observed on the PBMO and PBMCNO in CH_4/CO_2 reforming at various temperatures.

Figure 3.7a shows the equilibrium oxygen non-stoichiometry of PBMCNO as a function of $p(O_2)$ at a temperature of 650-750 °C. The measured δ increases with increasing the oxygen partial pressure. This behavior is similar to the relationship between oxygen content and oxygen partial pressure of other layered double perovskites.[1, 20, 21] Oxygen vacancy formed under reducing atmospheres is accompanied by the reduction of Mn^{4+} to Mn^{3+}, and Mn^{3+} to Mn^{2+} ions. The interaction between the defect species and the oxygen in the PBMCNO can be expressed as follows

$$2T_T^{\times} + \frac{1}{2}O_2 + V_O^{\bullet\bullet} \rightleftarrows O_O^{\times} + 2T_T^{\bullet} \qquad (1)$$

Where, $T_T^{\times}$ denotes B site metal in B site position with net charge zero, $V_O^{\bullet\bullet}$ denotes oxygen vacancy with net charge +2, $O_O^{\times}$ denotes oxygen in oxygen site with net charge zero, and $T_T^{\bullet}$ denotes B site metal in B site position with net charge +1. The partial molar enthalpy (*ΔH*) and partial molar entropy (*ΔS*) for reaction (1) can be calculated from the Fig. 4a using the Gibbs–Helmholtz equation and Maxwell relationship as follows,

$$\Delta H = \frac{\partial\left(\frac{\Delta G}{T}\right)}{\partial\left(\frac{1}{T}\right)} = \frac{R}{2}\frac{\partial \ln [p(O_2)]}{\partial\left(\frac{1}{T}\right)}\bigg|_{\delta} \qquad (2)$$

$$-\Delta S = \frac{\partial \Delta G}{\partial T} = \frac{R}{2}\frac{\partial \ln [p(O_2)]}{\partial T}\bigg|_{\delta} \qquad (3)$$

The *ΔH* and *ΔS* are calculated from the oxygen nonstoichiometric plot using the above equations (Figure 3.7b). From the calculation results, *ΔH* ranges from -301 to -247 kJ mol^{-1} and *ΔS* ranges from -109 to -118 J mol^{-1} K^{-1}. The calculated partial molar enthalpies suggest that the energy required to lift-off the oxygen from the lattice becomes larger with decreasing δ, and the partial molar entropies suggest that the probability of the oxygen vacancy formation reaction is almost constant as the reduction proceeds.

The electrochemical performance of single cells was characterized by $La_{0.9}Sr_{0.1}Ga_{0.8}Mg_{0.2}O_{3-\delta}$ (LSGM) electrolyte-supported cell in ambient air as the oxidant and humidified H_2 (3% H_2O) as the fuel with the composition of (PBMO and PBMCNO)/$La_{0.4}Ce_{0.6}O_{2-\delta}$ (LDC)/LSGM/$NdBa_{0.5}Sr_{0.5}Co_{1.5}Fe_{0.5}O_{5+\delta}$ - $Ce_{0.9}Gd_{0.1}O_{2-\delta}$. Impedance spectra and I-V curves of the single cells at 800 °C are presented in Figure 3.8 and Figure 3.7c, respectively. The non-ohmic resistance of PBMCNO (0.170 Ω cm^2) is lower than PBMO (0.302 Ω cm^2) and the maximum power density of PBMCNO (0.97 W cm^{-2}) is higher than PBMO (0.50 W cm^{-2}). The exsolved Co-Ni alloy nanoparticles act as catalyst for fuel oxidation, decreasing the anode polarization resistance.[3–5] To exemplify the remarkable improvement in the catalytic activity of Co-Ni alloy exsolved from PBMCNO, a dry reforming of methane using fixed-bed

reactor was evaluated at various temperatures (800-900 °C) with a fixed mole ratio of CH_4/CO_2 1:1. As shown in Figure 3.7d, CO_2 conversion and CO selectivity increase as the temperature increases for both PBMO and PBMCNO. The CO_2 conversion of PBMCNO is almost four times higher than that of PBMO, showing that the exsolved Co-Ni alloy nanoparticles on the surface enhance catalytic capability of hydrocarbon oxidation. Furthermore, no significant degradation in carbon coking was observed under a constant voltage of 0.4 V at 800 °C in CH_4 for more than 500 h (Figure 3.9). As shown in the SEM images (Figure 3.10), no carbon depositions are observed in the PBMCNO anode, indicating excellent carbon coking tolerance in the hydrocarbon fuel.

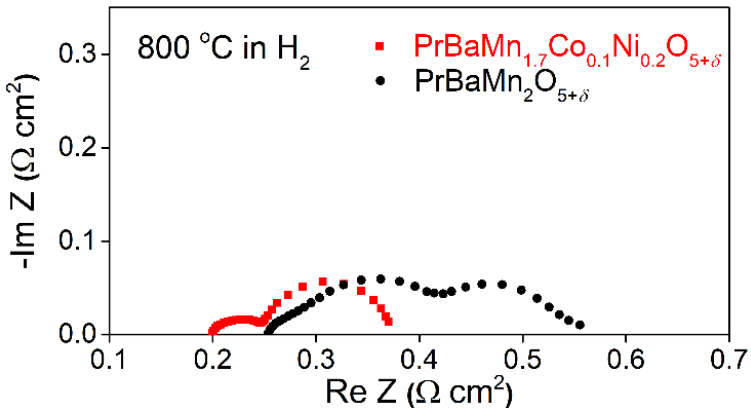

Figure 3.8. Impedance spectra of fuel cells with the $PrBaMn_2O_{5+\delta}$ and $PrBaMn_{1.7}Co_{0.1}Ni_{0.2}O_{5+\delta}$ anodes using humidified (3% H_2O) H_2 and ambient air as the oxidant at 800 °C.

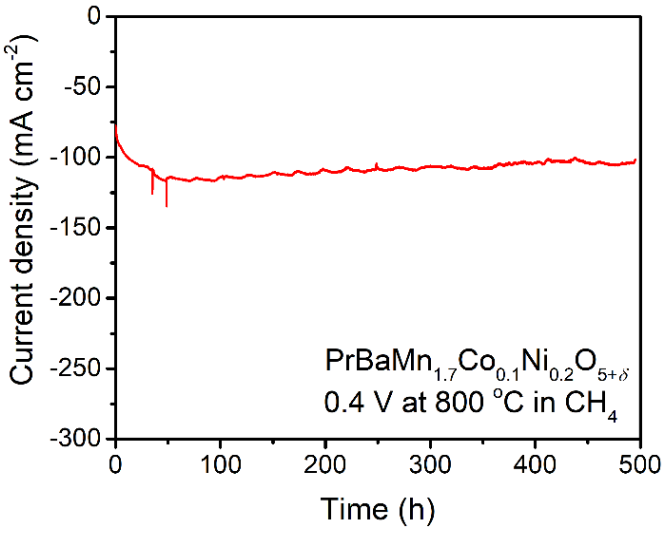

Figure 3.9. Electrochemical performance of fuel cell with $PrBaMn_{1.7}Co_{0.1}Ni_{0.2}O_{5+\delta}$ anode in CH_4 at 800 °C under a constant voltage of 0.4 V.

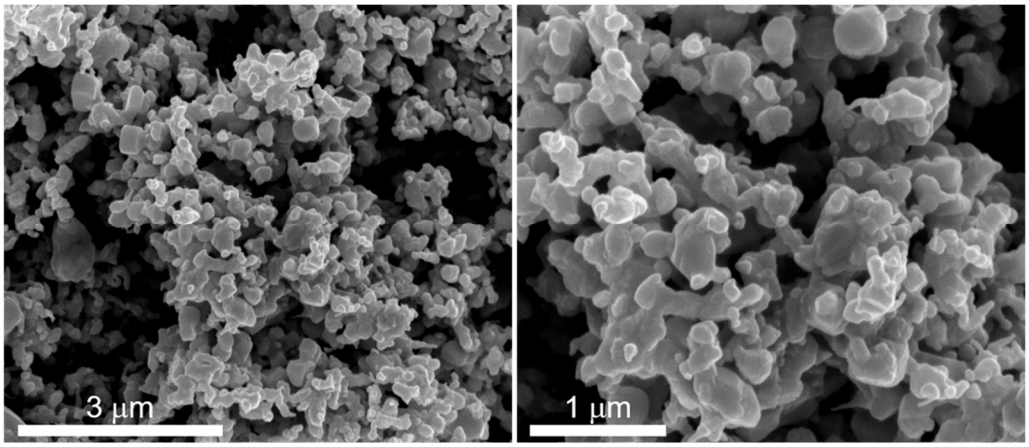

Figure 3.10. Scanning electron microscope images of $PrBaMn_{1.7}Co_{0.1}Ni_{0.2}O_{5+\delta}$ anode after stability test in CH_4 at 800 °C under a constant voltage of 0.4 V.

3.4 Conclusions

In this study, we found exsolved Co-Ni nanoparticles and demonstrated the mechanism for process of alloy exsolution on the PBMCNO layered double perovskite. Based on the DFT calculation, we proposed two possible mechanisms of bulk alloy formation and surface alloy formation to understand the alloy exsolution. The Gibbs energies of alloy formation at the surface and in the bulk, are −0.01 and 0.02 eV, respectively, indicating that Co and Ni are more thermodynamically favorable to form the alloy at the surface than in the bulk. The exsolved Co-Ni alloy nanoparticles on the PBMCNO layered double perovskite enhance catalytic performance for fuel oxidation in fuel cell and dry reforming of methane. The maximum power density of an LSGM electrolyte supported fuel cell with PBMCNO anode reached 0.97 W cm^{-2} at 800 °C in humidified hydrogen. Therefore, this study provides an understanding of the alloy exsolution mechanism in the layered double perovskites and a solution for improving the catalytic properties of high performance electrodes and reforming catalysts.

References

1. S. Sengodan, S. Choi, A. Jun, T. H. Shin, Y. -W. Ju, H. Y. Jeong, J. Shin, J. T. S. Irvine, G. Kim, Nat. Mater., 2015, **14**, 205–209.

2. J. Kim, A. Jun, O. Gwon, S. Yoo, M. Liu, J. Shin, T. -H. Lim, G. Kim, Nano Energy., 2018, **44**, 121–126.

3. A. Jun, J. Kim, J. Shin, G. Kim, Angew. Chemie Int. Ed., 2016, **55**, 12512–12515.

4. A. S. Yu, J. Kim, T. S. Oh, G. Kim, R. J. Gorte, J. M. Vohs, Appl. Catal. A Gen., 2014, **486**, 259–265.

5. Y. Bu, O. Gwon, G. Nam, H. Jang, S. Kim, Q. Zhong, J. Cho, G. Kim, ACS Nano., 2017, **11**, 11594-11601.

6. N. J. Jeon, J. H. Noh, Y. C. Kim, W. S. Yang, S. Ryu, S. I. Seok, Nat. Mater., 2014, **13**, 897-903.

7. Z. Du, H. Zhao, S. Yi, Q. Xia, Y. Gong, Y. Zhang, X. Cheng, Y. Li, L. Gu, K. Świerczek, ACS Nano., 2016, **10**, 8660-8669.

8. J. Myung, D. Neagu, D. N. Miller, J. T. S. Irvine, Nature., 2016, **537**, 528-531.

9. Y. -F. Sun, J. -H. Li, Y. -Q. Zhang, B. Hua, J. -L. Luo, ACS Catal., 2016, **6**, 2710–2714.

10. Y. -F. Sun, Y. -Q. Zhang, J. Chen, J. -H. Li, Y. -T. Zhu, Y. -M. Zeng, B. S. Amirkhiz, J. Li, B. Hua, J. -L. Luo, Nano Lett., 2016, **16**, 5303-5309.

11. Y. Zhu, W. Zhou, R. Ran, Y. Chen, Z. Shao, M. Liu, Nano Lett., 2016, **16**, 512-518.

12. D. Neagu, G. Tsekouras, D. N. Miller, H. Ménard, J. T. S. Irvine, Nat. Chem., 2013, **5**, 916–923.

13. D. Neagu, T. -S. Oh, D. N. Miller, H. Ménard, S. M. Bukhari, S. R. Gamble, R. J. Gorte, J. M. Vohs, J. T. S. Irvine, Nat. Commun., 2015, **6**, 8120.

14. T. Zhu, H. E. Troiani, L. V. Mogni, M. Han, S. A. Barnett, Joule., 2018, **2**, 478-496.

15. H. Chang, H. Chen, Z. Shao, J. Shi, J. Bai, S. -D. Li, J. Mater. Chem. A, 2016, **4**, 13997–14007.

16. O. Kwon, S. Sengodan, K. Kim, G. Kim, H. Y. Jeong, J. Shin, Y. -W. Ju, J. W. Han, G. Kim, Nat. Commun., 2017, **8**, 15967.

17. T. Wan, A. Zhu, Y. Guo, C. Wang, S. Huang, H. Chen, G. Yang, W. Wang, Z. Shao, J. Power Sources., 2017, **348**, 9–15.

18. G. Kresse, J. Furthmüller, Phys. Rev. B., 1996, **54**, 11169–11186.

19. J. D. Pack, H. J. Monkhorst, Phys. Rev. B., 1977, **16**, 1748–1749.

20. S. Choi, S. Sengodan, S. Park, Y. -W. Ju, J. Kim, J. Hyodo, H. Y. Jeong, T. Ishihara, J. Shin, G. Kim, J. Mater. Chem. A., 2016, **4**, 1747–1753.

21. S. Sengodan, Y. -W. Ju, O. Kwon, A. Jun, H. Y. Jeong, T. Ishihara, J. Shin, G. Kim, ACS Sustain. Chem. Eng., 2017, **5**, 9207-9213.

22. S. Liu, Q. Liu, J. -L. Luo, ACS Catal., 2016, **6**, 6219-6228.

23. E. Bennett, J. Monzó, J. Humphrey, D. Plana, M. Walker, C. McConville, D. Fermin, A. Yanson, P. Rodriguez, ACS Catal., 2016, **6**, 1533–1539.

24. Z. -X. Tian, A. Uozumi, I. Hamada, S. Yanagisawa, H. Kizaki, K. Inagaki, Y. Morikawa, Nanoscale Res. Lett., 2013, **8**, 203.

25. I. Hamada, A. Uozumi, Y. Morikawa, A. Yanase, H. Katayama-yoshida, J. Am. Chem. Soc., 2011, **133**, 18506–18509.

26. T. Zeng, J. Liao, H. Li, K. Feng, L. Li, RSC Adv., 2015, **5**, 105307–105312.

27. A. Jain, S. P. Ong, G. Hautier, W. Chen, W. D. Richards, S. Dacek, S. Cholia, D. Gunter, D. Skinner, G. Ceder, K. A. Persson, APL Mater., 2013, **1**, 011002.

28. Y. Gao, D. Chen, M. Saccoccio, Z. Lu, F. Ciucci, Nano Energy, 2016, **27**, 499–508.

29. S. -H. Cui, J. -H. Li, X. -W. Zhou, G. -Y. Wang, J. -L. Luo, K. T. Chuang, Y. Bai, L. -J. Qiao, J. Mater. Chem. A, 2013, **1**, 9689–9696.

30. J. Zhou, T. -H. Shin, C. Ni, G. Chen, K. Wu, Y. Cheng, J. T. S. Irvine, Chem. Mater., 2016, **28**, 2981-2993.

Chapter 4. Cation-swapped homogeneous nanoparticles in perovskite oxides for high power density

This chapter has been published

Reproduced from Joo, S.; Kwon, O.; Kim, K.; Kim, S.; Kim, H.; Shin, J.; Jeong H. Y.; Sengodan, S.; Han, J. W.; Kim, G. Cation-swapped homogeneous nanoparticles in perovskite oxides for high power density. *Nat. Commun.* **2019**, *10*, 697 DOI: 10.1038/s41467-019-08624-0.

4.1 Introduction

Exsolution has been recently explored as a method for the preparation of nanoparticles (NPs) with superior catalytic activity and durability for energy conversion and storage. Specifically, exsolution refers to the formation of metal nanoparticles on the surface of a metal oxide via the release and anchoring of cations from the host lattice to the oxide surface in a reducing atmosphere, producing catalysts with enhanced lifetime compared to traditional deposition techniques (*e.g.*, chemical vapor deposition or wet impregnation) by avoiding particle agglomeration.[6,7]

Despite its benefits, the exsolution process presents two major challenges. Firstly, a significant amount of exsolved metal can remain embedded in the host bulk due to the limited diffusion rate of metal cations.[8,9] Secondly, exsolution can cause structural instability in the host material due to excessive loss of cations.[10] To overcome these challenges, several factors governing the degree of exsolution, such as the nature of the host lattice and environmental conditions,[11] have been extensively investigated in simple perovskite[12,13] (ABO_3) or layered perovskite[2,14–17] ($AA'B_2O_5$). For example, A-site deficiency ($A/B < 1$) in perovskite oxide (ABO_3) has been actively researched recently in terms of cation stoichiometry/non-stoichiometry manipulation.[12,18–20]

Meanwhile, topotactic ion exchange is an interesting soft chemical method that has been applied to numerous perovskite-related compounds for cation replacement.[21,22] Therefore, it could be envisaged as a solution with wide applicability for the complete exsolution of metal cations without leaving cation defects in the host lattice, thereby maintaining the overall structural features of the parent metal oxide.[21]

Herein, we report the use of topotactic ion exchange to overcome the problems associated with common exsolution techniques. When a stoichiometric layered perovskite oxide ($AA'B_{2-x}C_xO_{5+\delta}$) is used, the exsolution of y moles of C metal from the B site would be accompanied by the formation of the corresponding amount of B-site vacancies (Schottky-type defect) (equation 1). In contrast, in the topochemical ion exchange concept, such layered perovskite oxide can yield x moles of exsolved C metal by the ion exchange with x moles of the guest cation G (equation 2). Overall, the topochemical ion exchange produces the layered perovskite without B-site vacancies, thereby preserving the atomic

connectivity of the B–O–B network for an efficient oxygen transport and electron conduction.

$$\underbrace{AA'B_{2-x}C_xO_{5+\delta}}_{\text{Stoichiometric layered perovskite}} \rightarrow \underbrace{AA'B_{2-x}C_{x-y}\square_yO_{5+\delta}}_{\text{Residual layered perovskite with B-site vacancy }(\square)} + \underbrace{yC}_{\text{Exsolved metal}} \quad (1)$$

$$\underbrace{AA'B_{2-x}C_xO_{5+\delta}}_{\text{Stoichiometric layered perovskite}} + \underbrace{xG}_{\text{Guest cation}} \xrightarrow[\text{exchange}]{\text{Topotactic ion}} \underbrace{AA'B_{2-x}G_xO_{5+\delta}}_{\text{New layered perovskite without B-site vacancy}} + \underbrace{xC}_{\text{Exsolved metal}} \quad (2)$$

We selected the layered perovskite $PrBaMn_{1.7}Co_{0.3}O_{5+\delta}$ (PBMCo) as the host and Fe (Fe^{3+}/Fe^{4+}) as the guest cation. A previous study revealed that, in layered perovskite, the Co cation has a higher tendency to be exsolved toward the surface than Fe, mainly due to the higher co-segregation energy of Co (−0.55 eV) compared to that of Fe (−0.15 eV).[2] Therefore, when the Fe guest cation is externally introduced into the host material, the initial host PBMCo can be converted to $PrBaMn_{1.7}Fe_{0.3}O_{5+\delta}$ (PBMFe) through topotactic cation exchange. This simple synthetic approach not only can readily exsolve most of the cations from the bulk lattice but also can produce new compounds with multiple functionalities by exsolving nanoparticles without leaving cation defects. Moreover, we illustrate that the as-exsolved particles exhibit high catalytic activities, which are verified by solid oxide fuel cell anode test and dry reforming reaction of methane.

4.2 Experimental

$Pr_{0.5}Ba_{0.5}Mn_{0.85}Co_{0.15}O_{3-\delta}$, $Pr_{0.5}Ba_{0.5}Mn_{0.85}Fe_{0.15}O_{3-\delta}$, and $Pr_{0.5}Ba_{0.5}MnO_{3-\delta}$ were prepared by the Pechini sol-gel synthesis method. The required amounts for stoichiometry of $Pr(NO_3)_3{\cdot}6H_2O$ (Aldrich, 99.9%, metal basis), $Ba(NO_3)_2$ (Aldrich, 99+%), $Mn(NO_3)_2{\cdot}4H_2O$ (Aldrich, 98%), $Fe(NO_3)_3{\cdot}9H_2O$ (Aldrich, 98+%), and $Co(NO_3)_2{\cdot}6H_2O$ (Aldrich, 98+%) were dissolved in distilled water. After complete dissolution, proper amounts of ethylene glycol and citric acid as complexing agents were added to the solution and combustion process on heating plate is followed to make fine powders. These powders were calcined at 600 ºC for 4 h to eliminate organic residue. The chemical composition of the synthesized powders and their abbreviations are given in Table 4.1.

Commercial electrolyte powders, $La_{0.9}Sr_{0.1}Ga_{0.8}Mg_{0.2}O_{3-\delta}$, (LSGM, 99.9% Kceracell) was pressed into pellet of 0.9 g and sintered at 1475 ºC. After sintering, pellet was polished to about 250 μm. A buffer layer, $La_{0.4}Ce_{0.6}O_{2-\delta}$ (LDC) was prepared by ball milling stoichiometric amounts of La_2O_3 and CeO_2 (Sigma, 99.99%) in ethanol and then calcined at 1,000 ºC for 6h. LDC is applied between anode and electrolyte to prevent ionic inter-diffusion. Anode powder PBMCo was mixed with an organic binder

(Heraeus V006) (1:2 weight ratio) to make slurry ink. Cathode powders composed of $PrBa_{0.5}Sr_{0.5}Co_{1.5}Fe_{0.5}O_{5+\delta}$(PBSCF)-$Ce_{0.9}Gd_{0.1}O_{2-\delta}$ (at a weight ratio of 60:40) were mixed with an organic binder (1:1.2 weight ratio) for a cathode slurry ink as described elsewhere.[19,20] These electrode inks were applied on the LSGM electrolyte pellet by screen printing method to produce a configuration of PBMCo | LDC | LSGM | PBSCF-GDC, which was followed by sintering at 950 °C in air for 4 h. The Fe precursor solution was infiltrated on PBMCo after sintering. The porous electrodes had an active area of 0.36 cm^2 and thickness about 20 μm. For the electrochemical tests, Ag wires were fixed to both electrodes using Ag paste as current collectors and the cell was sealed on an alumina tube using a ceramic adhesive (Ceramabond 552, Aremco). The entire cell was placed inside a furnace and heated to the desired temperature. I-V polarization curves were measured using a BioLogic Potentiostat.

Compound	Abbreviations
$PrBaMn_{1.7}Co_{0.3}O_{5+\delta}$	PBMCo
$PrBaMn_{1.7}Co_{0.3}O_{5+\delta}$ + 3wt% infiltration of Fe	PBMCo-3-Fe
$PrBaMn_{1.7}Co_{0.3}O_{5+\delta}$ + 7wt% infiltration of Fe	PBMCo-7-Fe
$PrBaMn_{1.7}Co_{0.3}O_{5+\delta}$ + 12wt% infiltration of Fe	PBMCo-12-Fe
$PrBaMn_{1.7}Co_{0.3}O_{5+\delta}$ + 15wt% infiltration of Fe	PBMCo-15-Fe
$PrBaMn_{1.7}Co_{0.3}O_{5+\delta}$ + 12wt% infiltration of Co-Fe	PBMCo-12-CoFe
$PrBaMn_2O_{5+\delta}$	PBM
$PrBaMn_2O_{5+\delta}$ + 12wt% infiltration of Fe	PBM-12-Fe
$PrBaMn_2O_{5+\delta}$ + 12wt% infiltration of Co	PBM-12-Co
$PrBaMn_{1.7}Fe_{0.3}O_{5+\delta}$	PBMFe
$PrBaMn_{1.7}Fe_{0.3}O_{5+\delta}$ + 12wt% infiltration of Co-Fe	PBMFe-12-CoFe
$PrBa_{0.5}Sr_{0.5}Co_{1.5}Fe_{0.5}O_{5+\delta}$	PBSCF
$Ce_{0.9}Gd_{0.1}O_{2-\delta}$	GDC
$La_{0.4}Ce_{0.6}O_{2-\delta}$	LDC
$La_{0.9}Sr_{0.1}Ga_{0.8}Mg_{0.2}O_{3-\delta}$	LSGM

wt%: weight percent to anode

Table 4.1. Nomenclature for the compounds based on the Fe-infiltrated PBMCo system

A deposition on sample was fulfilled by an infiltration procedure. Precursor solution for infiltration of Fe and Co-Fe were prepared in 0.7 M by dissolving an appropriate amount $Fe(NO_3)_3 \cdot 9H_2O$ (Aldrich, 98+%), $Co(NO_3)_2 \cdot 6H_2O$ (Aldrich, 98+%), and citric acid into distilled water. Precursor solutions were infiltrated into porous PBMCo with various weight percent to parent material (3, 7, and 12 wt. %) and then calcined in air at 450 °C for 4 h. This infiltration procedure was repeated to achieve the targeted weight percent.

To compare the exsolution phenomenon with varying the amount of the deposited Fe on PBMCo, pre-calcined PBMCo was fired at 950 °C in air for 4 h. The sintered PBMCo was infiltrated with Fe precursor solution and reduced at 850 °C in H_2 atmosphere (with 3% H_2O) for 4 h.

The crystal structures of the samples were identified by an XRD (Bruker, D8 Advance, Cu Ka radiation, 40 kV, 40 mA). The morphologies of materials were investigated using SEM (FEI, Nova Nano 230 FE-SEM). TEM images were obtained with a FEI Titan (3) G2 60-300 with an imaging-forming Cs corrector at an accelerating voltage of 80 kV. N_2 adsorption and desorption isotherms measurement was carried out at -196 ^{o}C (BELSORP-Mini II, BEL Co.) to evaluate the pore structure and specific surface area. The specific surface area of the catalysts was calculated from the N_2 adsorption and desorption isotherms results by the BET method. XPS analyses were conducted on ESCALAB 250XI from Thermo Fisher Scientific with a monochromatic A1-Kα (ultraviolet He1, He2) X-ray source.

DFT calculations were carried out using the Vienna Ab initio Simulation Package (VASP)[21, 22]. Exchange-correlation energies were treated by Perdew-Burke-Ernzerhof (PBE) functional based on generalized gradient approximation (GGA)[23]. An energy cutoff of 400 eV was used for plane-wave expansion. A 3 × 3 × 1 Monkhorst-Pack *k*-point sampling of the Brillouin zone was used for all slab calculations[34]. Gaussian smearing was used with a width of 0.05 eV to determine partial occupancies. Geometries were relaxed using a conjugate gradient algorithm until the forces on all unconstrained atoms were less than 0.03 eV/Å. In order to take into account for on-site Coulomb and exchange interactions, GGA+*U* schemes were used with the effective *U* values of 4.0, 3.3, and 4.0 for Mn, Co, and Fe, respectively. The 8 layered PBMO slab model was constructed with the vacuum thickness of up to 17 Å in the *z*-direction by cleaving a bulk PBMO structure[2]. The dopant position at top surface or in 5th layer represents that it is located at surface or in bulk, respectively.

In order to describe the alloy formation, we substituted two Mn atoms with Co or Fe atom in PBMO (Figure 4.1). The Gibbs free energies were also calculated for the thermodynamics of alloy and oxygen vacancy formation based on our previous calculation scheme (Figure 4.2)[2]. More calculation details are provided in supplementary information.

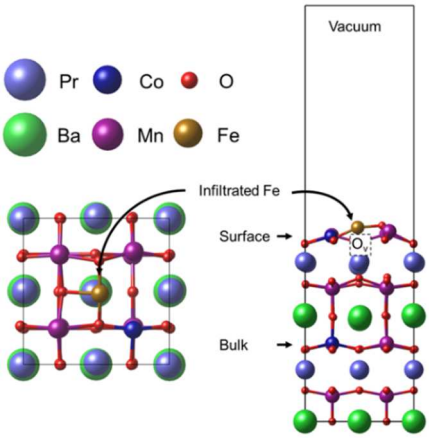

Figure 4.1. Top and side views of surface model structures of Fe infiltrated PBMCo used in our DFT calculations. Note that the locations of initial and final states of the segregated Co are assumed to be the first and the fifth layers in our slab model. For the calculations of Fe infiltrated PBMCo, one Fe atom is added on the surface of PBMCo. The oxygen vacancy formation (O_v) is mostly favorable at a nearest neighbor of surface Co and infiltrated Fe.

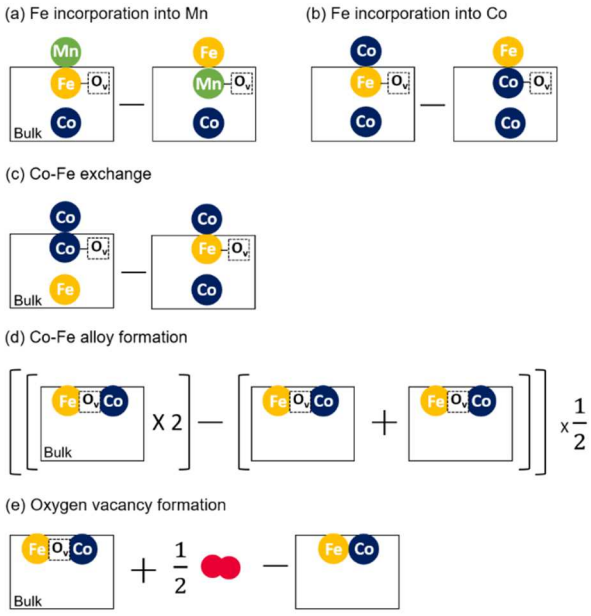

Figure 4.2. Schematic illustration for DFT-calculated energetics at each elementary step. The incorporation energy was defined by the total energy difference between the systems where the infiltrated Fe is located on the surface of PBMCo and at the surface B-metal lattice of (a) Mn or (b) Co. (c) The Co-Fe exchange energy was calculated by the total energy difference between the systems before and after the exchange of the location of surface Fe and bulk Co. (d) The alloy formation energy was calculated by the total energy difference between the systems where two different B-site metals are separated and aggregated. (e) The oxygen vacancy formation energy was calculated by total energy difference of the supercells with and without an oxygen vacancy.

Catalytic activity for dry reforming of methane was evaluated through gas chromatography (GC) (Agilent 7820A GC instrument) with a thermal conductivity detector (TCD) and a packed column (Agilent carboxen 1000). The gas used for GC measurement were controlled using a mass flow controller (MFC) (Atovac GMC1200) and the exact volume value of gas was calibrated through a bubble flow meter.

The 0.2 g of sample powder (950 ^{o}C sintered in air for 4 h) was prepared and packed in the middle of the quartz tube reactor using glass wool. The sample powder was in-situ reduced at 900 ^{o}C for 30 minutes while blowing humified H_2 (3% H_2O) gas in a quartz tube reactor.

After reduction, purging for 1 hour with He gas before each measurement to remove residual H_2, then CO_2, CH_4, and He were inserted with a ratio of 20:20:60 ml min^{-1}, respectively.

The dry reforming reaction is shown as below, CO_2 conversion and CO selectivity were calculated using the following equations.[25, 26]

$$CH_4 + CO_2 \leftrightarrow 2CO + 2H_2 \ (\Delta H^0_{298K} = 247 \text{ kJ/mol})$$

$$CO_2 \text{ conversion} = \frac{[CO_2]_{consumed}}{[CO_2]_{feed}} \times 100\% = \frac{[CO]_{detect}}{[CO]_{detect} + 2[CO_2]_{detect}} \times 100\%$$

$$CO \text{ selectivity} = \frac{[CO]_{detect}}{[CO]_{detect} + [CO_2]_{detect}} \times 100\%$$

4.3 Results and Discussions

In this work, a layered stoichiometric perovskite, $PrBaMn_{1.7}Co_{0.3}O_{5+\delta}$ was selected as the ion exchange host for the preferential exsolution of Co to exemplify the topotactic manipulation. We selected Co as exsolving cation since Co in the B sites has the highest co-segregation energy toward exsolution among various transition metals (Mn, Co, Ni, and Fe), whereas Fe was chosen as the guest material with the lowest co-segregation energy.[2] The deposition of guest cation was done by infiltrating a nitrate solution having different weight percentages of Fe (0, 3, 7, and 12 wt.% with respect to the host material) on $Pr_{0.5}Ba_{0.5}Mn_{0.85}Co_{0.15}O_{3-\delta}$. The amount of infiltrated Fe was also calculated in a mole percentage as shown in Table 4.2. After the infiltration, $Pr_{0.5}Ba_{0.5}Mn_{0.85}Co_{0.15}O_{3-}$ deposited with Fe oxide was annealed in humified hydrogen at 850 °C to exsolve nanoparticles along with phase transition from simple perovskite to layered perovskite structure. Table 4.1 summarizes the different abbreviations of the samples.

Sample	Weight percent of Fe_2O_3 infiltrated (%)	Mol of Fe_2O_3 for the weight percentage to 1 mol of PBMCo	Mole of Fe
PBMCo-12-Fe	12	0.35	0.18
PBMCo-7-Fe	7	0.21	0.10
PBMCo-3-Fe	3	0.09	0.04
Remarks	*(Weight for 1 mol of PBMCo) = 469.28 g/mol *(Weight for 1 mol of Fe_2O_3) = 159.69 g/mol		

Table 4.2. Nomenclature for the compounds based on the Fe-infiltrated PBMCo system

In the process of Co exsolution under a reducing atmosphere, the Co cation in the host material PBMCo undergoes topotactic ion exchange with the deposited Fe due to the difference of co-segregation energy between Co and Fe. Thus, Co tends to be exsolved to the surface while Fe remains in the bulk in the $PrBaMn_{1.7}T_{0.3}O_{5+\delta}$ system (T = Mn, Ni, Co, or Fe).[2] In a stoichiometric layered perovskite, the exsolution of transition metal cation was observed along with the phase transition under a reducing atmosphere (R1 in Figure 4.3a), leaving B-site vacancies (Schottky-type defect). Under typical conditions, only a limited fraction of B-site transition metal can be exsolved. In a stoichiometric layered perovskite of $PrBaMn_{1.7}Ni_{0.3}O_{5+\delta}$ composition, only 58% of Ni can migrate to the surface, leaving many B-site vacancies,[2] with the concomitant decrease in both the oxygen ion conduction and electron conduction paths. On the contrary, for the topotactic ion exchange/exsolution method (R2 in Figure 4.3a), the guest cation is deposited on the patent stoichiometric layered perovskite material followed by reduction. During the exsolution process, the topotactic ion exchange occurs between the lattice Co and the deposited Fe. In parallel, all the Co cations from the B sites are exsolved without the formation of B-site vacancies. The filling of the B sites eventually leads to improved ionic and electrical conduction paths. In the topotactic ion exchange process, Fe dissolves into the underlying perovskite lattice due to its low co-segregation energy compared to that of other transition metals.

To simulate the topotactic ion exchange process between B-site cations, DFT calculation was performed. We assumed that the process occurs through two major stages, i.e. (1) incorporation of the infiltrated Fe into the lattice and (2) exchange between the incorporated Fe and the host Co, and the energy at each stage was investigated. This mechanism of cation exchange in layered perovskites can be expressed in point defect (Schottky-type defect) reactions as follows:

Exsolution without cation exchange,

$$Co_{Co}^{\times} + O_{O}^{\times} \leftrightarrow CoO + V_{O}^{\bullet\bullet} + V_{Co}'' \quad (3)$$

$$CoO \leftrightarrow Co_{(\text{metallic exsolution})} + \frac{1}{2}O_2 \quad (4)$$

Exsolution by topotactic ion exchange,

$$Co_{Co}^{\times} + O_{O}^{\times} + FeO_{(infiltrated)} \leftrightarrow CoO_{(exsolved)} + V_{O}^{\bullet\bullet} + Fe_{Co}^{\times} \quad (5)$$

$$CoO \leftrightarrow Co_{(metallic\ exsolution)} + \frac{1}{2}O_2 \quad (6)$$

Where $Co_{Co}^{\times}$ denotes the Co in the Co site with net charge zero, $O_{O}^{\times}$ denotes oxygen in the oxygen site with net charge zero, $V_{O}^{\bullet\bullet}$ denotes the oxygen ion vacancy with the net charge of +2, V_{Co}'' denotes the cation vacancy in the Co site with the net charge of −2, $Fe_{Co}^{\times}$ denotes the incorporated Fe in the Co site with net charge zero, and FeO/CoO denotes the Fe/Co oxide, respectively.

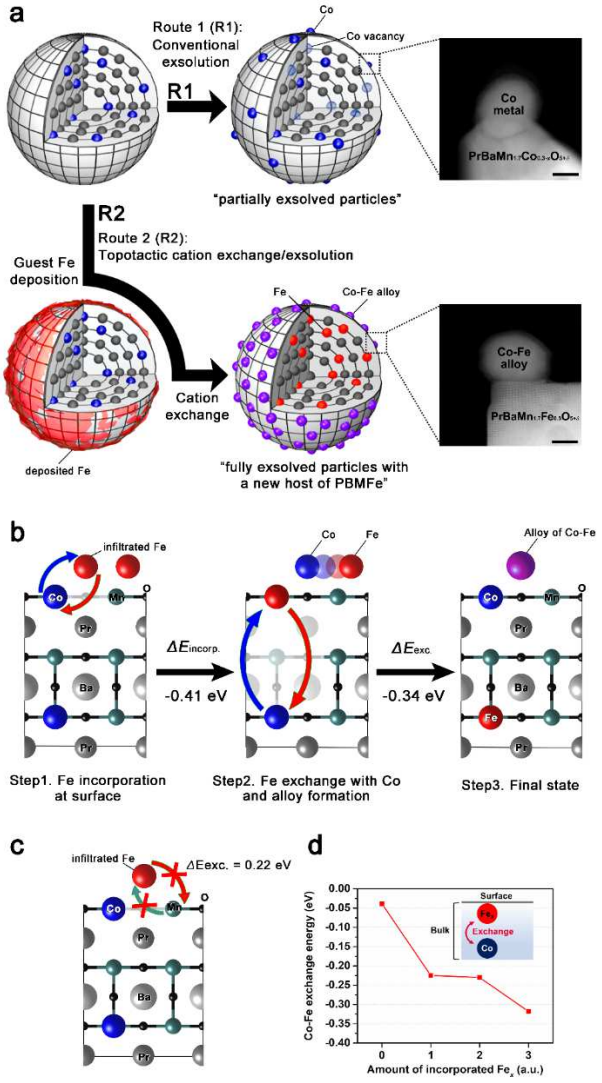

Figure 4.3. Schematic of exsolution process and density functional theory calculations. a Exsolution process with and without topotactic ion exchange. b Topotactic ion exchange energetics for the mechanism of particle exsolution via Fe infiltration on the PBMCo surface. c The unfavorable incorporation energy of infiltrated Fe with Mn of the top surface. d Calculated energetics for the Co–Fex exchange depending on arbitrary Fe concentration

Once Fe is deposited on the host PBMCo, Fe incorporates into the near surface of PBMCo through the exchange with the Co cations on the B sites. Since both the exsolved Co and host Mn can co-exist at the near surface of PBMCo, we compared two possible exchange pathways, Fe ↔ Co and Fe ↔ Mn, on the B cation layer of the surface. Our results show that Fe ↔ Co (−0.41 eV) is thermodynamically more favored than Fe ↔ Mn (0.22 eV) (Figure 4.3b and Figure 4.3c). Thus, the incorporation of Fe occurs through its exchange with Co. After the incorporation, further exchange between the incorporated Fe and the bulk Co is thermodynamically favorable, with an exchange energy of −0.34 eV. Therefore, it can be concluded that Co exsolution is facilitated by the incorporation of Fe.

Next, the Co–Fe exchange energy was calculated as a function of the incorporated Fe concentration in an arbitrary unit (Figure 4.3d). As the arbitrary concentration of the incorporated Fe increases up to the specific concentration, the Co–Fe exchange is thermodynamically favored. This also supports that the Fe incorporation into the host PBMCo possibly accelerates Co exsolution. The Gibbs energy of aggregation ($\Delta G_{aggr.}$) of Co–O_v–Fe at the surface (surface alloy formation) is 0.01 eV, implying that the aggregation of Co and Fe requires only little energy on the surface. This result is consistent with that of the TEM investigation that will be discussed later, which evidences the formation of a Co–Fe alloy. In addition, the lower oxygen vacancy formation energy at the surface of PBMCo-12-Fe (2.52 eV) compared to that of the host PBM (2.97 eV) would promote further reduction of Co–Fe aggregation to form Co–Fe alloy NPs.

To provide evidence of the occurrence of topotactic ion exchange, we varied the amount of infiltrated Fe precursor and investigated the correlation between the amount of Fe deposition and the population of exsolved nanoparticles through scanning electron microscopy (SEM) and Brunauer–Emmett–Teller (BET) analysis. Figure 4.4a shows the schematics of the experimental process. The SEM images of PBMCo, PBMCo-3-Fe, PBMCo-7-Fe, and PBMCo-12-Fe are shown in Figure 4.4b-e. The micrographs illustrate that spherical exsolved nanoparticles of 20–50 nm are evenly distributed on the surface of the parent material. Interestingly, as the amount of infiltrated Fe precursor increase from 0 to 12 wt.%, more spherical particles seem to be exsolved to the surface of the layered perovskite. To provide a more quantitative correlation between the population of particles and the amount of deposited Fe, the exsolved nanoparticles in a specific area were numbered by an image analysis tool (Image J software). As seen in Figure 4.4f, the results demonstrate that the amount of deposited Fe oxides promotes exsolution, particularly a significant increase up to 12 wt.% of infiltrated Fe oxides. With the amount of 15 wt.% infiltration, number of the exsolved nanoparticles in a specific area is not deviated from that of 12 wt.% (counted as 98 particles shown in Figure 4.5a), indicating that the promotion of exsolution is saturated at the certain amount of the deposition. These trends are in good agreement with the BET analysis of the specific surface area of the material, as shown in the right axis of Figure 4.4f, Figure 4.5. This can

be explained by the fact that the specific surface area is affected only by the exsolved nanoparticles, not by the amount of Fe deposition. To validate this statement, we deposited Fe on $Pr_{0.5}Ba_{0.5}MnO_{3-\delta}$ and annealed it in H_2 to form a PBM with layered perovskite structure. The samples with 12 wt.% Fe (PBM-12-Fe) and without Fe (PBM) show a specific surface area of 1.16 and 1.17 $m^2\ g^{-1}$, respectively (Figure 4.5b), and the surface morphology of PBM-12-Fe (Figure 4.5c) appears to be smooth, indicating that the contribution to the specific surface area by infiltration of 12 wt.% Fe on the layered perovskite support is negligible.

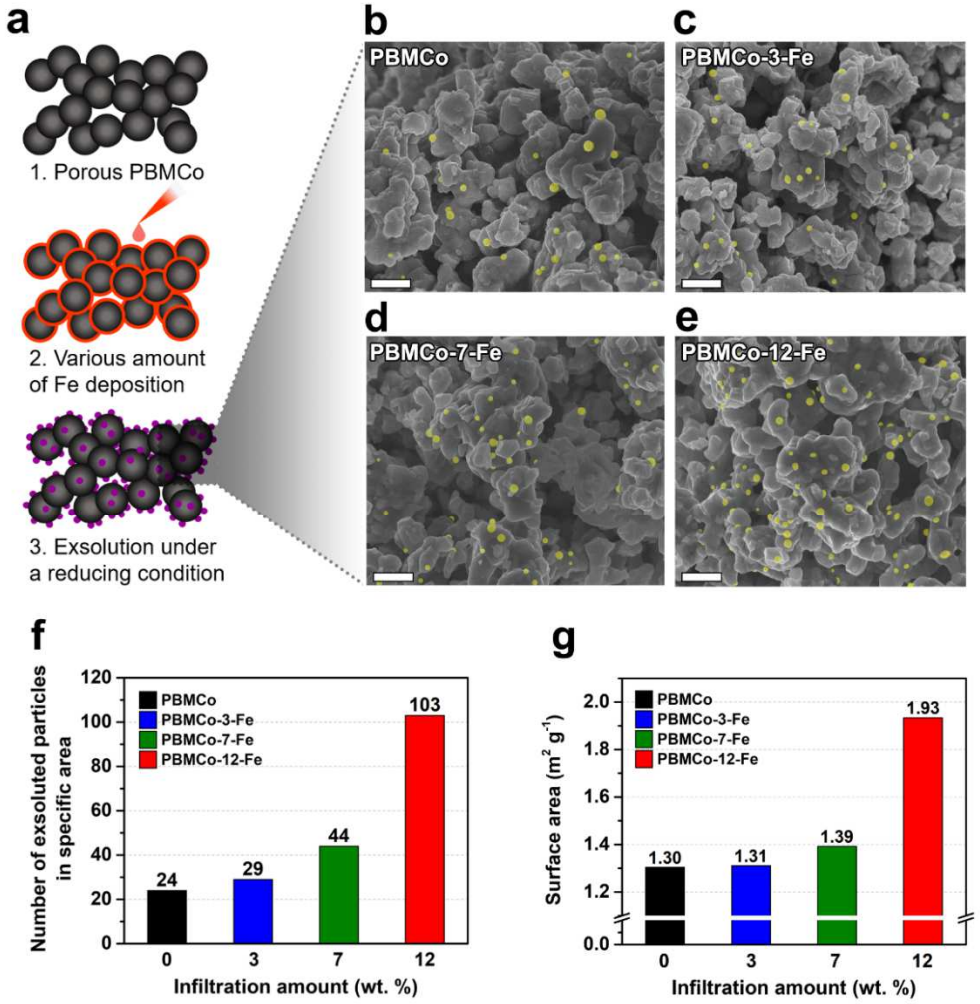

Figure 4.4. Scanning electron microscopy images and population of exsolved particles. a Sample preparation process for confirming the correlation between the amount of infiltrated Fe and the population of exsolved nanoparticles. b–e SEM images of b PBMCo, c PBMCo-3-Fe, d PBMCo-7-Fe, and e PBMCo-12-Fe (exsolved nanoparticles are highlighted in yellow); scale bars are 500 nm. f Number of exsolved particles in specific area counted by Image J. g Specific surface area calculated by the BET method

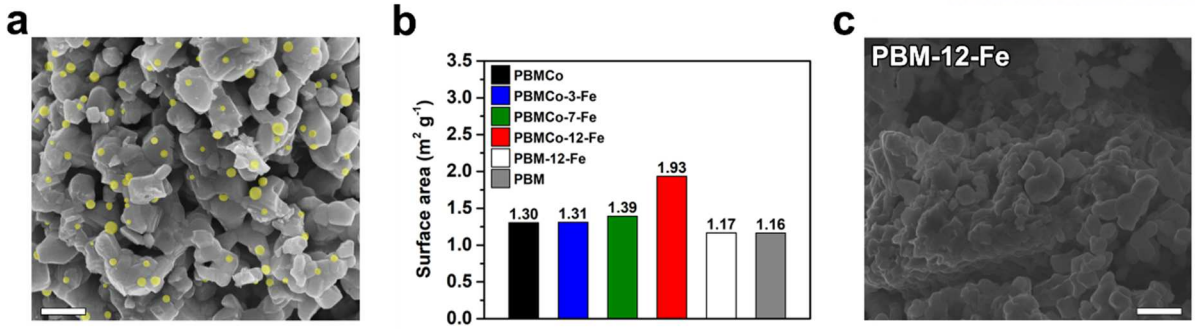

Figure 4.5. SEM images and population of particles. (a) SEM image of PBMCo-15-Fe; scale bar 500 nm. (b) Comparison of the specific surface area between samples calculated by the BET methods. (c) SEM image of PBM-12-Fe; scale bar 500 nm.

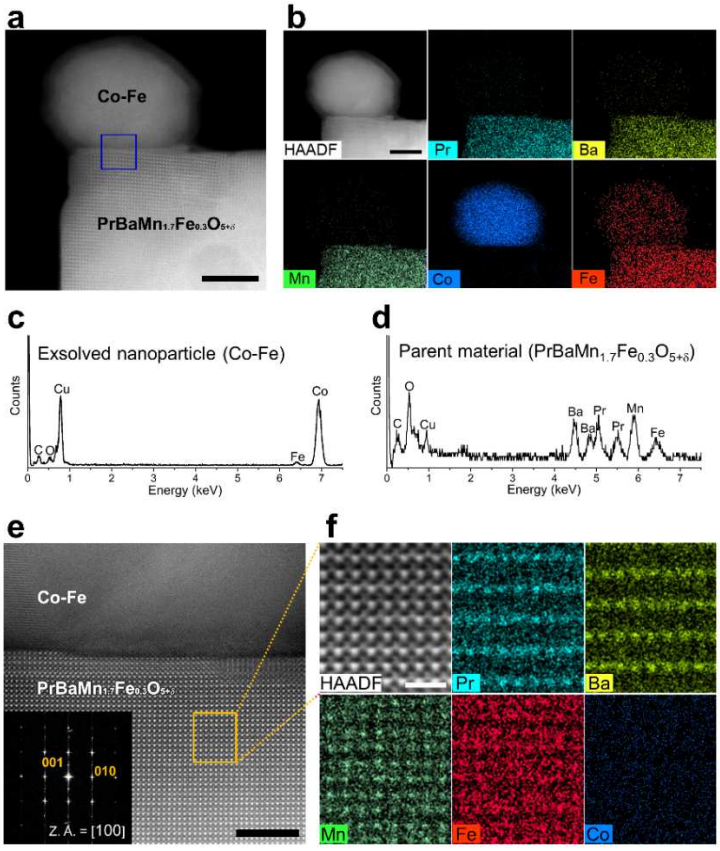

Figure 4.6. Transmission electron microscopy of exsolved particles and parent material. a HAADF scanning TEM image of PBMCo-12-Fe. b EDS elemental map of Pr, Ba, Mn, Co, and Fe; scale bar 20 nm. c EDS spectrum of the exsolved nanoparticles. d EDS spectrum of the parent material of PBMCo-12-Fe. e HAADF scanning TEM image of PBMCo-12-Fe (blue square in Fig. 4.5a) and the corresponding fast-Fourier transformed pattern with zone axis = [100]; scale bar 5 nm. f EDS elemental map of Pr, Ba, Mn, Fe, and Co in the parent material of PBMCo-12-Fe (yellow rectangle in Fig. 4.5d); scale bar 1 nm

To investigate the crystalline structure and composition of the layered perovskite with exsolved nanoparticles, we examined the samples using transmission electron microscopy (TEM). As shown in the high-angle annular dark field (HAADF) scanning TEM image of PBMCo-12-Fe (Figrue 4.6a), nanoparticles having about 30 nm diameter were exsolved from the parent material. In addition, the PBMCo-12-Fe sample was subjected to energy dispersive spectroscopy (EDS) (Figure 4.6b), showing that the exsolved nanoparticles consist of a Co–Fe alloy, and the parent layered perovskite contains Pr, Ba, Mn, and Fe, which is consistent with the EDS spectrum results (Figure 4.6c and 4.6d). This disappearance of Co in the lattice is due to the topotactic ion exchange between the lattice Co and deposited Fe, clearly showing that Co and Fe switch their lattice positions. To gain further insights on the crystal lattice and the topotactic ion exchange, we performed atomic-scale scanning TEM analysis. The A-site ordering was observed by a small additional spot in the fast-Fourier transformed (FFT) pattern indexed to (001) of the tetragonal structure (Figure 4.6e). Furthermore, atomic-scale EDS mapping was conducted in the parent oxide (orange rectangle in Figure 4.6e) to investigate the A-site cation ordering and the positions of Co and Fe (Figure 4.6f). It was found that the atomic positions of Pr, Ba, and Mn remained unaltered, while some Fe was observed in the position of Mn, which implies that Fe entered the B sites of PBMCo. Meanwhile, Co signals were not clearly observed in the EDS mapping, which demonstrates that most of the Co was exsolved to the surface due to the topotactic ion exchange with Fe.

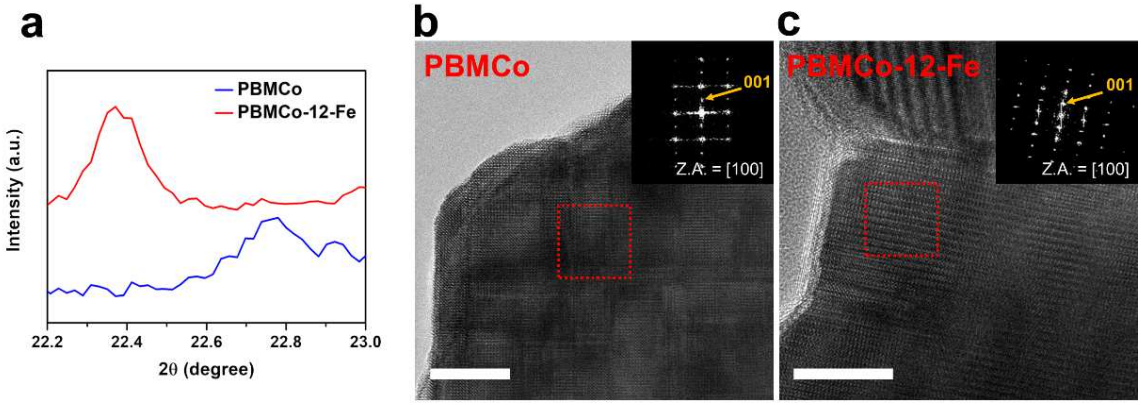

Figure 4.7. (a) X-ray diffraction patterns of PBMCo and PBMCo-12-Fe samples around 22 °. HR TEM image of (b) PBMCo and (c) PBMCo-12-Fe samples and the corresponding fast-Fourier transformed pattern with zone axis = [100]; scale bar 10 nm.

Moreover, we examined XRD peaks around 22 ° to determine the change in lattice as exchanging cations (Figure 4.7a). The peaks around 22 ° corresponding to (200) are 22.79 ° and 22.37 ° for PBMCo and PBMCo-12-Fe, respectively. The peak shift to the left indicates that the lattice expansion occur due to

the cation exchange of smaller Co ions (Co^{2+} (r=0.745 Å) or Co^{3+} (r=0.545 Å)) and larger Fe ions (Fe^{2+} (r = 0.780 Å) or Fe^{3+} (r=0.645 Å)).[20, 27] We also measured high-resolution TEM to confirm the lattice constants before and after the exchange. As shown in the HR TEM images, the lattice spaces between (001) planes of before (Figure 4.7b) and after (Figure 4.7c) exchange are identified as 0.803 and 0.815 nm by fast-Fourier transformed pattern, respectively. Therefore, it can be concluded that the lattice constant of the layered perovskite somewhat increases after the exchange between Co and Fe.

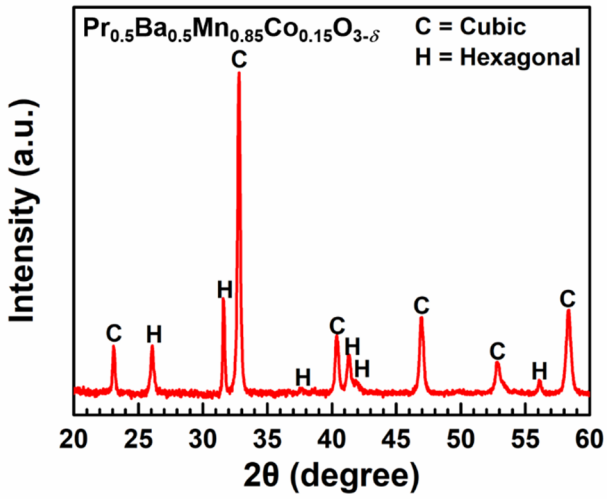

Figure 4.8. X-ray diffraction patterns of $Pr_{0.5}Ba_{0.5}Mn_{0.85}Co_{0.15}O_{3-\delta}$ sintered at 950 °C for 4 h in air.

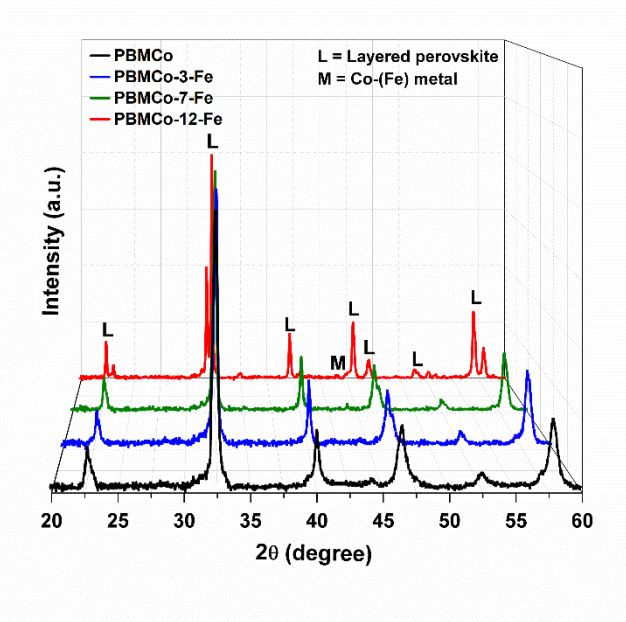

Figure 4.9. X-ray diffraction patterns of PBMCo, PBMCo-3-Fe, PBMCo-7-Fe, and PBMCo-12-Fe samples.

The perovskite oxides were analyzed by X-ray diffraction before and after reduction. From the XRD diffraction pattern (Figure 4.8), it can be deduced that the host material samples sintered at 950 °C in air for 4 h exhibit simple perovskite structures of mixed cubic and hexagonal phases without secondary phase. The diffraction patterns of the PBMCo, PBMCo-3-Fe, PBMCo-7-Fe, and PBMCo-12-Fe samples are shown in Figure 4.9. Under a reducing atmosphere, all the samples experience phase transition from simple perovskite to layered perovskite along with the formation of exsolved nanoparticles on the surface of host materials. For PBMCo, the peak for exsolved Co metal is observed at 2 theta = 44.26° (JCPDS card#15-0806). As the amount of deposited Fe increases, the peak for metal is lower-angle shifted (44.26 ° for PBMCo and PBMCo-3-Fe and 44.17 ° for PBMCo-7-Fe and PBMCo-12-Fe, respectively) due to the formation of the Co–Fe alloy, which originates from the dissolution of Fe in the Co lattice.[28] The diffraction pattern of PBMCo-12-Fe exhibits several additional peaks that are absent in those of the other perovskite oxides. This can be ascribed to the formation of $PrBaMn_{1.7}Co_{0.3-y}Fe_yO_{5+\delta}$ from $Pr_{0.5}Ba_{0.5}Mn_{0.85}Co_{0.15}O_{3-\delta}$ as a result of the swapping between Co and Fe cations according to equation (7). When the B sites of Co are fully substituted by the Fe cations, the parent material is transformed into $PrBaMn_{1.7}Fe_{0.3}O_{5+\delta}$, whose characteristic peak splitting is easily distinguishable from that of $PrBaMn_{1.7}Co_{0.3}O_{5+\delta}$.[2] These results clearly demonstrate the topotactic ion exchange between the host cation Co and the deposited Fe that leads to the selective exsolution of Co without any change in the crystal structure except the exchange of B-site cations.

$$Pr_{0.5}Ba_{0.5}Mn_{0.85}Co_{0.15}O_{3-\delta} + Fe_2O_3\ (\text{deposition}) \xrightarrow{reducing} PrBaMn_{1.7}Co_{0.3-y}Fe_yO_{5+\delta} + y\text{Co} - \text{Fe}\ (\text{exsolution and formation of alloy}) \quad (7)$$

X-ray photoelectron spectroscopy (XPS) was performed to determine the oxidation states of B-site dopants in PBMCo-3-Fe, PBMCo-7-Fe, and PBMCo-12-Fe. As shown in Figure 4.10, the binding energy peaks of Fe ions in the bulk for Fe $2p_{3/2}$ and Fe $2p_{1/2}$ consist of 710 and 723.7 eV corresponding to Fe^{2+}, 712.5 and 725.5 eV corresponding to Fe^{3+}, respectively. For the all samples, Fe is present as the form of mixed Fe^{2+} and Fe^{3+}. In the case of Co, Co metal is predominant and Co^{2+} and Co^{3+} coexist in a similar ratio.

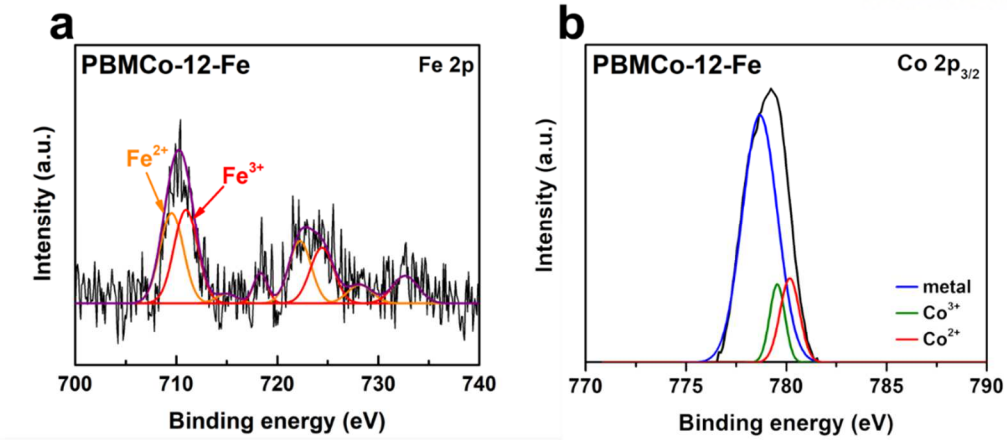

Figure 4.10. X-ray photoelectron spectroscopy of (a) Fe 2p for PBMCo-12-Fe and (b) Co $2p_{3/2}$ for PBMCo-12-Fe.

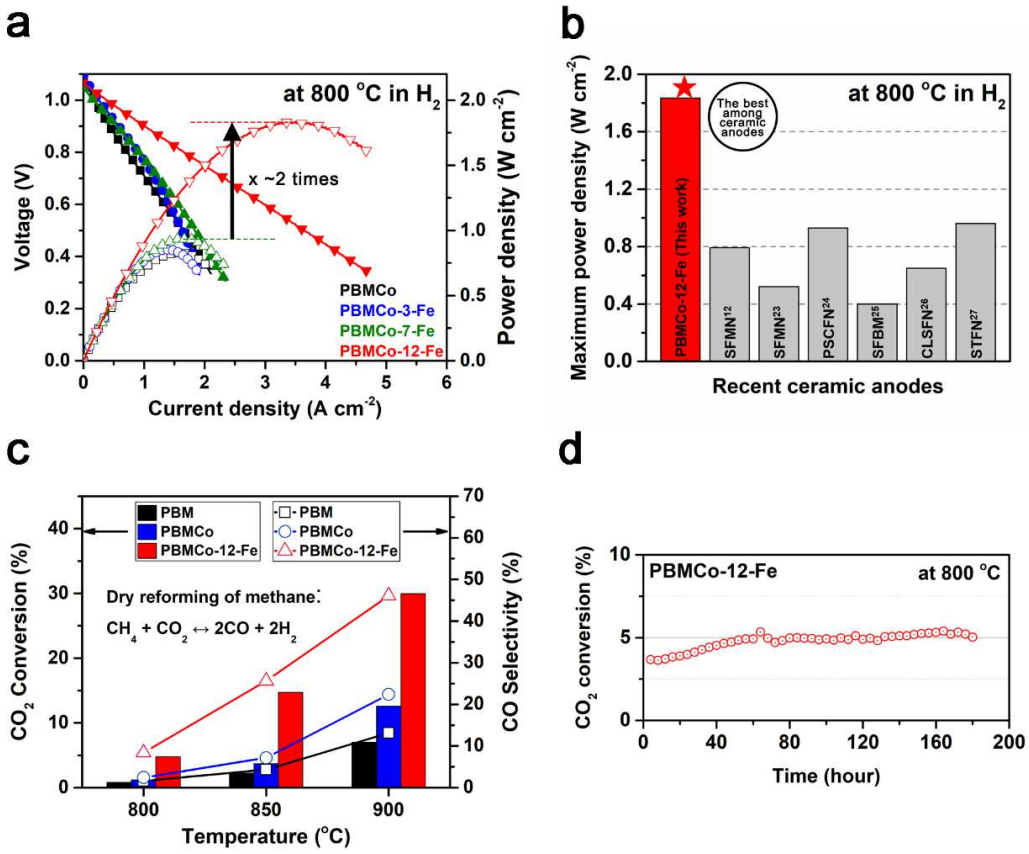

Figure 4.11. Catalytic properties. a I–V curve and the maximum power densities of the PBMCo-x-Fe samples. b Comparison of the maximum power density at 800 °C in H_2 from the present work and other reported studies11,12,23–26. c Conversion of CO_2 and selectivity of CO measured for PBM, PBMCo, and PBMCo-12-Fe in dry reforming of methane at various temperatures. d Time-dependence of CO_2 conversion for PBMCo-12-Fe in dry reforming of methane at 800 °C

To investigate the applicability of the present topotactic ion exchange/exsolution method, the electrochemical performance of fuel cells based on PBMCo-*x*-Fe as the anode was evaluated and compared with that of a PBM anode. The fuel cells with a configuration of PBMCo-*x*-Fe | LDC | LSGM | PBSCF-GDC were tested in humidified H_2 (with 3% H_2O) as the fuel and ambient air as the oxidant. The maximum power densities (MPDs) were 0.826, 0.853, 0.938, and 1.834 W cm^{-2} for PBMCo, PBMCo-3-Fe, PBMCo-7-Fe, and PBMCo-12-Fe, respectively, at 800 °C in humidified H_2 (Figure 4.11a). The number of exsolved particles was found to increase with the amount of Fe infiltration due to the topotactic ion exchange, which resulted in a tremendous enhancement of the electrochemical performance of the SOFC anode. In contrast, the samples without metal exsolution, i.e., the parent PBM anodes with deposited Co and Fe catalyst (Figure 4.12), showed no increment in the electrochemical performance, suggesting that the exsolved particles formed by topotactic ion exchange play a key role in the catalytic activity.

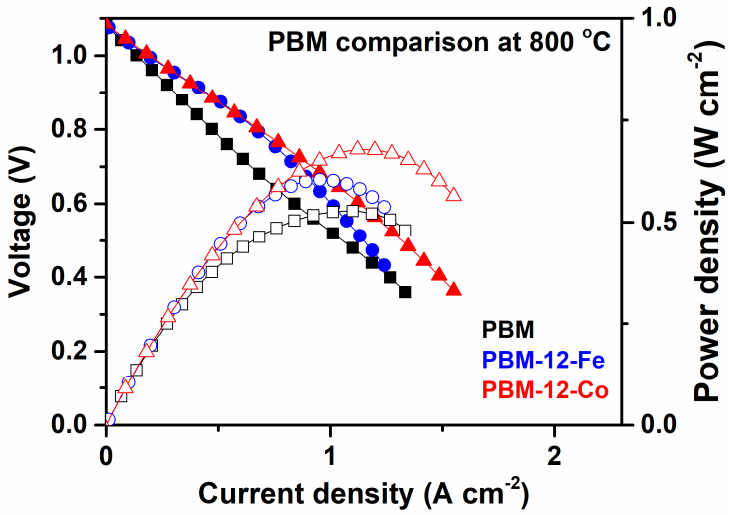

Figure 4.12. I-V curve and power densities of the PBM, PBM-12-Fe, and PBM-12-Co at 800 °C in H_2 (3% H_2O).

To clarify the effect of the cation exchange on the electrochemical performance, Co–Fe infiltrated PBMFe and Co–Fe infiltrated PBMCo were evaluated (Figure 4.13). PBMFe was used for comparative purposes to simulate the parent material after the cation exchange, since the bulk of PBMCo-12-Fe is considered to alter to PBMFe through the cation exchange. The MPD values of PBMFe-12-CoFe and PBMCo-12-CoFe were determined to be 0.743 W cm^{-2} and 0.962 W cm^{-2}, respectively, revealing that the catalytic activity of the Co–Fe alloy particles infiltrated on the parent PBMFe and PBMCo without topotactic cation exchange is not as high as that of the cation-exchanged PBMCo-12-Fe. This can be attributed to the difference in surface morphology between samples. As displayed in the HAADF scanning TEM image of the PBMFe-12-CoFe sample (Figure 4.14), the infiltrated Co–Fe alloy particles

exist irregularly as coarsened particles with a size of 50–300 nm. In contrast, exsolved nanoparticles of 20–50 nm are uniformly distributed on the surface of the PBMCo-12-Fe sample (Fig. 2e). These results are in line with previous findings that present agglomeration and coarsening of catalytic NPs by infiltration as well-known concerns.[29]

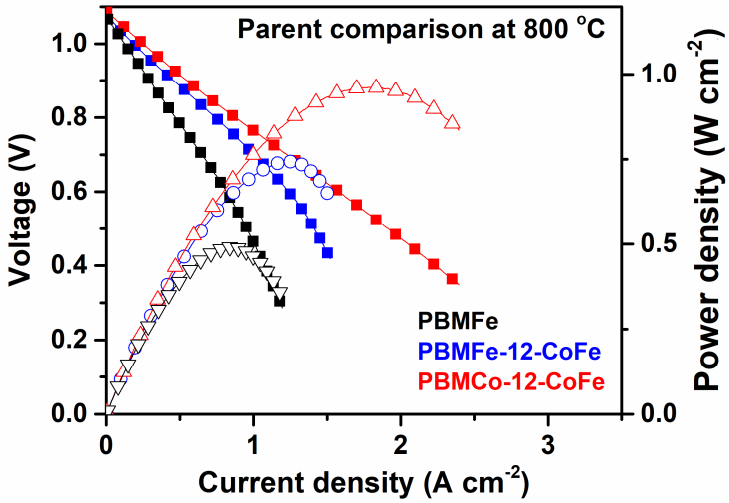

Figure 4.13. I-V curve and power densities of the PBMFe-12-CoFe and PBMCo-12-CoFe at 800 °C in H_2 (3% H_2O).

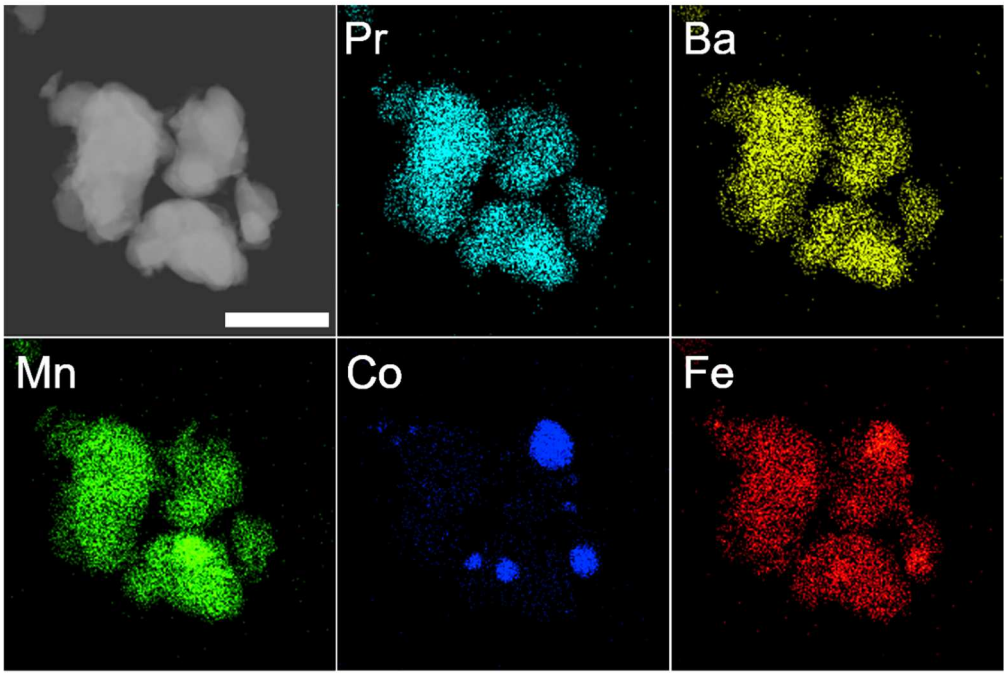

Figure 4.14. High-angle annular dark field (HAADF) image of PBMFe-12-CoFe (NPs formed by infiltration) sample with the EDS elemental map of Pr, Ba, Mn, Co, Fe, and O; scale bar 500 nm.

The non-ohmic resistances for PBMCo-3-Fe, PBMCo-7-Fe, and PBMCo-12-Fe were 0.330, 0.237, and 0.071 Ω cm^2, respectively, at 800 °C in H_2 (with 3% H_2O) (Figure 4.15), which are consistent with the trends observed for the maximum power density. In particular, the single cell performance of PBMCo-12-Fe demonstrates superior catalytic activity among recently developed ceramic anodes using exsolution[12, 30-34](Figure 4.11b). Additionally, to measure the stability of the particles obtained via the topotactic ion exchange/exsolution method, we compared the SEM images of the PBMCo-12-Fe sample after prolonged exposure to 3% humidified hydrogen. As can be seen in Figure 4.16, the exsolved particles maintain their morphologies without undergoing agglomeration even after exposure at 800 °C in humidified H_2 over 100 h.

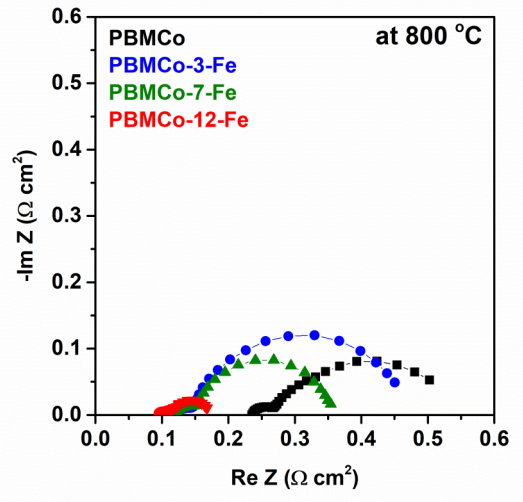

Figure 4.15. Impedance spectra of the PBMCo, PBMCo-3-Fe, PBMCo-7-Fe, and PBMCo-12-Fe at 800 °C in H_2 (3% H_2O).

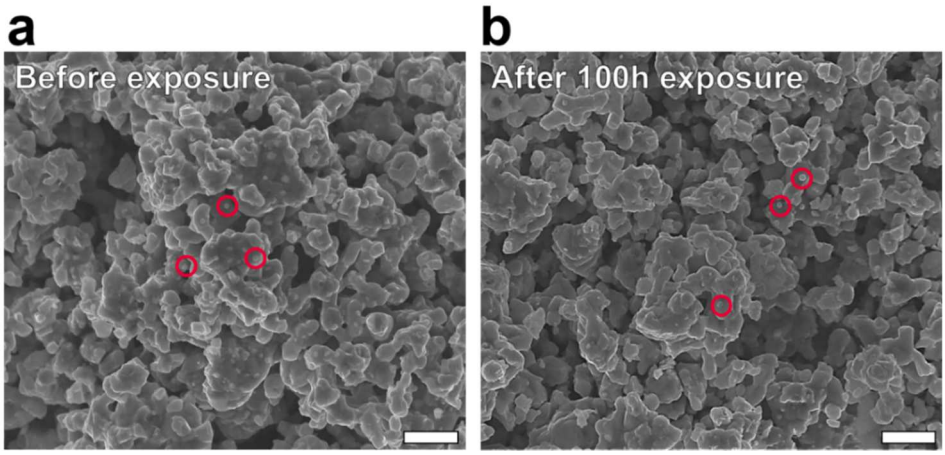

Figure 4.16. Comparison in SEM surface morphology of PBMCo-12-Fe before and after exposure to H_2 (with 3% H_2O) at 800 °C for 100 hours. The red circles indicate the exsolved nanoparticles; scale bar 500 nm.

The catalytic activity of the samples for the dry reforming of methane (DRM) was also assessed using a quartz tube reactor, since Co-based species are known to be excellent catalysts for DRM.[35] At 900 °C, the CO_2 conversion using the PBMCo-12-Fe sample reached 30%, which is almost two times higher than that of PBMCo and four times higher than that of PBM, as shown in Figure 4.11c. The higher conversion of CO_2 for PBMCo-12-Fe strongly supports its excellent capability as DRM catalyst with a long-term stability over 160 h (Figure 4.11d). As shown in Figure 4.17, Co-Fe alloy has an overall metallic phase after DRM reactions and some FeO_x are formed on the surface of Co-Fe alloy due to the difference in redox property of Co and Fe[6]. The reactions involving CO_2 oxidation and CH_4 reduction during DRM are given by the following steps (equation (8) to (10)) according to a Mars-van Krevelen (MvK) mechanism[36]. That is, Co-Fe alloy particles undergo de-alloying/re-alloying process during DRM and consequently, FeO on the surface reacts with carbon deposited on Co to form CO (equation (10)).

$$CH_4 \rightarrow C_{Co} + 2H_2 \quad (8)$$

$$Fe + xCO_2 \leftrightarrow FeO_x + xCO \quad (9)$$

$$FeO_x + C_{Co} \rightarrow xCO + Co + Fe \quad (10)$$

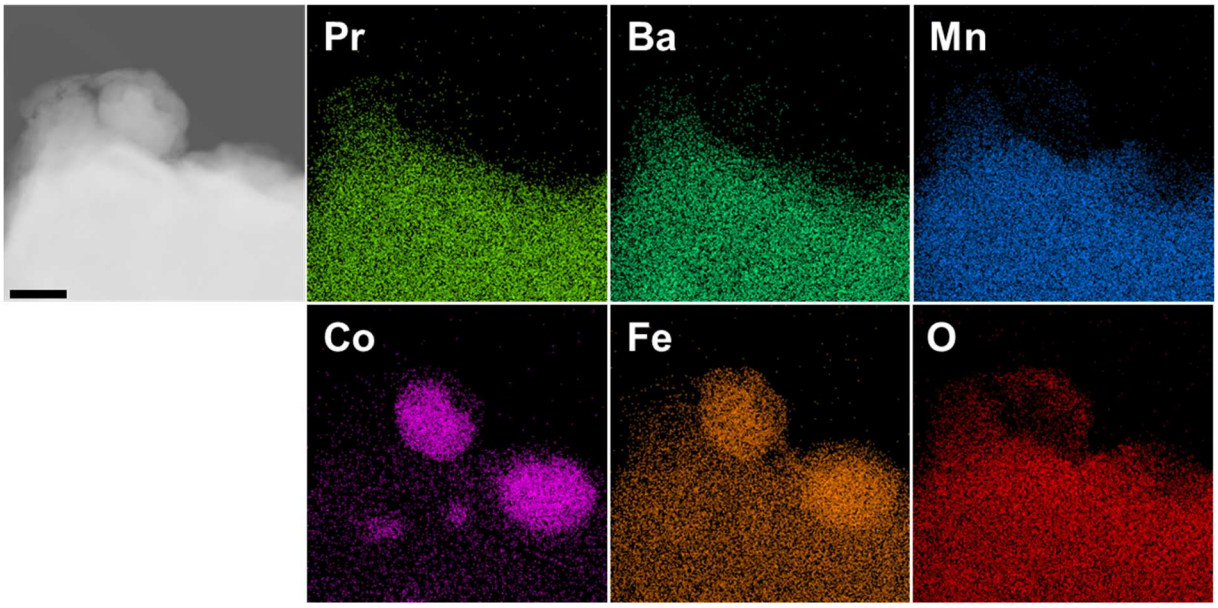

Figure 4.17. High-angle annular dark field (HAADF) image of PBMCo-12-Fe sample with the EDS elemental map of Pr, Ba, Mn, Co, Fe, and O after DRM test at 900 °C; scale bar 100 nm.

4.4 Conclusions

In summary, we have demonstrated the first example of a topotactic ion exchange/exsolution method that offers extensive control over the structure and properties of the obtained nanoparticles. The effectiveness of this approach emphasizes the utility of the topotactic ion exchange manipulation for the selective exsolution of catalytic nanoparticles in oxide materials. The topotactic cation exchange between Co and Fe can occur spontaneously due to the favorable incorporation energy (−0.41 eV) and exchange energy (−0.34 eV) for the deposition of the guest material Fe on the host material PBMCo, consequently resulting in the transformation of PBMCo into PBMFe, according to the results of DFT calculation. The maximum power density of an electrolyte-supported cell with a PBMCo-12-Fe anode reaches 1.834 W cm^{-2} in humidified H_2 at 800 °C, achieving excellent electrochemical performance compared to other recently developed ceramic anodes. In addition, the catalyst activity in DRM is improved about four times and two times compared to PBM and PBMCo, respectively, at 900 °C. This approach based on topotactic cation exchange provides a powerful methodology for controlling the properties of exsolution by actively customizing the material through external cation intercalation, which goes beyond the existing methods that depend on the characteristics of the material itself.

References

1. Neagu, D., Tsekouras, G., Miller, D. N., Menard, H. & Irvine, J. T. S. In situ growth of nanoparticles through control of non-stoichiometry. *Nat Chem* **5,** 916–923 (2013).

2. Nishihata, Y. *et al.* Self-regeneration of a Pd-perovskite catalyst for automotive emissions control. *Nature* **418,** 164–167 (2002).

3. Lin, C., Jang, J. B., Zhang, L., Stach, E. A. & Gorte, R. J. Improved coking resistance of 'Intelligent' Ni catalysts prepared by atomic layer deposition. *ACS Catal.* **8,** 7679–7687 (2018).

4. Katz, M. B. *et al.* Reversible precipitation/dissolution of precious-metal clusters in perovskite-based catalyst materials: Bulk versus surface re-dispersion. *J. Catal.* **293,** 145–148 (2012).

5. Ma, Q., Tietz, F. & Stöver, D. Nonstoichiometric Y-substituted $SrTiO_3$ materials as anodes for solid oxide fuel cells. *Solid State Ionics* **192,** 535–539 (2011).

6. Li, Y. *et al.* Controlling cation segregation in perovskite-based electrodes for high electro-catalytic activity and durability. *Chem. Soc. Rev.* 6345–6378 (2017).

7. Neagu, D. *et al.* Nano-socketed nickel particles with enhanced coking resistance grown in situ by redox exsolution. *Nat Commun* **6,** 8120 (2015).

8. Kobsiriphat, W. *et al.* Nickel- and Ruthenium-doped lanthanum chromite anodes: effects of nanoscale metal precipitation on solid oxide fuel cell performance. *J. Electrochem. Soc.* **157,** B279 (2010).

9. Kwon, O. *et al.* Exsolution trends and co-segregation aspects of self-grown catalyst nanoparticles in perovskites. *Nat. Commun.* **8,** 15967 (2017).

10. Sengodan, S. *et al.* Self-decorated MnO nanoparticles on double perovskite solid oxide fuel cell anode by in situ exsolution. *ACS Sustain. Chem. Eng.* **5,** 9207–9213 (2017).

11. Yang, C. *et al.* In situ fabrication of CoFe alloy nanoparticles structured $(Pr_{0.4}Sr_{0.6})_3(Fe_{0.85}Nb_{0.15})_2O_7$ ceramic anode for direct hydrocarbon solid oxide fuel cells. *Nano Energy* **11,** 704–710 (2015).

12. Du, Z. *et al.* High-performance anode material $Sr_2FeMo_{0.65}Ni_{0.35}O_{6-\delta}$ with in situ exsolved nanoparticle catalyst. *ACS Nano* **10,** 8660–8669 (2016).

13. Yang, C. *et al.* Sulfur-tolerant redox-reversible anode material for direct hydrocarbon solid oxide fuel cells. *Adv. Mater.* **24,** 1439–1443 (2012).

14. Neagu, D. & Irvine, J. T. S. Structure and properties of $La_{0.4}Sr_{0.4}TiO_3$ ceramics for use as anode materials in solid oxide fuel cells. *Chem. Mater.* **22,** 5042–5053 (2010).

15. Tsekouras, G., Neagu, D. & Irvine, J. T. S. Step-change in high temperature steam electrolysis performance of perovskite oxide cathodes with exsolution of B-site dopants. *Energy Environ. Sci.* **6,** 256–266 (2013).

16. Konysheva, E. Y., Xu, X. & Irvine, J. T. S. On the existence of A-site deficiency in perovskites and its relation to the electrochemical performance. *Adv. Mater.* **24,** 528–532 (2012).

17. Schöllhorn, R. Reversible topotactic redox reactions of solids by electron/ion transfer. *Angew. Chemie Int. Ed. English* **19,** 983–1003 (1980).

18. Clearfield, A. Role of ion exchange in solid-state chemistry. *Chem. Rev.* **88,** 125–148 (1988).

19. Choi, S. *et al.* Highly efficient and robust cathode materials for low-temperature solid oxide fuel cells: $PrBa_{0.5}Sr_{0.5}Co_{2-x}Fe_xO_{5+\delta}$. *Sci. Rep.* **3**, 2426 (2013).

20. Joo, S., Kim, J., Shin, J., Lim, T.-H. & Kim, G. Investigation of a layered perovskite for IT-SOFC cathodes: B-site Fe-doped $YBa_{0.5}Sr_{0.5}Co_{2-x}Fe_xO_{5+\delta}$. *J. Electrochem. Soc.* **163**, F1489–F1495 (2016).

21. Kresse, G. & Furthmuller, J. Efficient iterative schemes for ab initio total energy calculations using a plane-wave basis set. *Phys. Rev. B* **54**, 11169–11186 (1996).

22. Kresse, G. & Hafner, J. Norm-conserving and ultrasoft pseudopotentials for first-row and transition elements. *J. Phys. Condens. Matter* **6**, 8245–8257 (1994).

23. Perdew, J. P., Burke, K. & Ernzerhof, M. Generalized gradient approximation made simple. *Phys. Rev. Lett.* **77**, 3865–3868 (1996).

24. Pack, J. D. & Monkhorst, H. J. Special points for Brillonin-zone integrations. *Phys. Rev. B* **16**, 1748–1749 (1977).

25. Wan, T. *et al.* Co-generation of electricity and syngas on proton-conducting solid oxide fuel cell with a perovskite layer as a precursor of a highly efficient reforming catalyst. *J. Power Sources* **348**, 9–15 (2017).

26. Kwon, O. *et al.* Self-assembled alloy nanoparticles in layered double perovskite as a fuel oxidation catalyst for solid oxide fuel cells. *J. Mater. Chem. A* **6**, 15947–15953 (2018).

27. Shannon, R. D. Revised effective ionic radii and systematic studies of interatomic distances in halides and chalcogenides. *Acta Cryst.* A **32**, 751 (1976).

28. Kim, S. *et al.* Tailoring Ni-based catalyst by alloying with transition metals (M=Ni, Co, Cu, and Fe) for direct hydrocarbon utilization of energy conversion devices. *Electrochim. Acta* **225**, 399–406 (2017).

29. Ding, D., Li, X., Lai, S. Y., Gerdes, K. & Liu, M. Enhancing SOFC cathode performance by surface modification through infiltration. *Energy Environ. Sci.* **7**, 552 (2014).

30. Ding, H., Tao, Z., Liu, S. & Yang, Y. A redox-stable direct-methane solid oxide fuel cell (SOFC) with $Sr_2FeNb_{0.2}Mo_{0.8}O_{6-\delta}$ double perovskite as anode material. *J. Power Sources* **327**, 573–579 (2016).

31. Yang, C. *et al.* In situ fabrication of CoFe alloy nanoparticles structured $(Pr_{0.4}Sr_{0.6})_3(Fe_{0.85}Nb_{0.15})_2O_7$ ceramic anode for direct hydrocarbon solid oxide fuel cells. *Nano Energy* **11**, 704–710 (2015).

32. Sun, K. *et al.* Investigation of B-site doped perovskites $Sr_2Fe_{1.4}X_{0.1}Mo_{0.5}O_{6-\delta}$ (X=Bi, Al, Mg) as high-performance anodes for hybrid direct carbon fuel cell. *J. Power Sources* **365**, 109–116 (2017).

33. Chung, Y. S. *et al.* In situ preparation of a $La_{1.2}Sr_{0.8}Mn_{0.4}Fe_{0.6}O_4$ Ruddlesden–Popper phase with exsolved Fe nanoparticles as an anode for SOFCs. *J. Mater. Chem. A* **5**, 6437–6446 (2017).

34. Zhu, T., Troiani, H. E., Mogni, L. V., Han, M. & Barnett, S. A. Ni-Substituted Sr(Ti,Fe)O_3 SOFC anodes: achieving high performance via metal alloy nanoparticle exsolution. *Joule* **2**, 478–496 (2018).

35. Bouarab, R., Akdim, O., Auroux, A., Cherifi, O. & Mirodatos, C. Effect of MgO additive on catalytic properties of Co/SiO_2 in the dry reforming of methane. *Appl. Catal. A Gen.* **264**, 161–168 (2004).

36. Bian, Z., Das, S., Wai, M. H., Hongmanorom, P. & Kawi, S. A Review on bimetallic nickel-based catalysts for CO_2 reforming of methane. *ChemPhysChem* **18**, 3117–3134 (2017).

Chapter 5. *In Situ* Surface Modification of Ni-YSZ with $BaZrO_3$ for Enhancing the Sulfur Tolerance of Ni-YSZ Anode

This chapter has been published

Reproduced from Kwon, O.; Sengodan, S.; Lim, C.; Jeong H. Y.; Shin, J.; Ju, Y. -W.; Kim, G. In Situ Surface Modification of Ni-YSZ with $BaZrO_3$ for Enhancing the Sulfur Tolerance of Ni-YSZ Anode. *J. Electrochem. Soc.* **2016**, *163*, F1055-F1058 DOI: 10.1149/2.0651609jes by permission of The Electrochemical Society. Copyright 2016.

5.1 Introduction

Ni and Ni alloy have been studied for the utilization as a catalyst in hydrocarbon reforming,[1–3] water splitting,[4,5] oxygen reduction reaction,[6,7] and redox reaction in supercapacitor.[8,9] Especially, Ni-based catalysts with high catalytic activity toward fuel reforming have been widely used in solid oxide fuel cells (SOFCs).[10–14] The conventional Ni-YSZ cermet anode with an YSZ electrolyte of SOFCs has excellent catalytic activity and electrical conductivity in H_2 fuel. However, it has suffered from carbon coking and sulfur poisoning when hydrocarbon fuels are used as a fuel.[15–17] The carbon and sulfur are adsorbed on the Ni surface depending upon operating conditions, and they degrade the electrodes and block the electrochemically active sites, leading to serious performance degradation.[18–20]

In this regard, some efforts have been made to find Ni-free ceramic anode materials that provide improved sulfur tolerance and coking tolerance under hydrocarbon fuel operation. The ceramic anodes such as Sr_2MgMoO_6, $La_{0.33}Sr_{0.67}Ti_xMn_{1-x}O_{3-\delta}$,$Y_xSr_{1-x}Ti_{1-x}Fe_xO_{3-\delta}$,and $La_{0.8}Sr_{0.2}Sc_xMn_{1-x}O_{3-\delta}$ have shown improved sulfur tolerance.[21–24] Compared to the conventional Ni-YSZ, however, the ceramic anodes have poor electrochemical activity, low electrical conductivity and in- sufficient compatibility with an YSZ electrolyte at high temperatures.

Other approaches to enhance the sulfur tolerance of the conventional Ni-YSZ anode based on surface coating of the Ni-YSZ with CeO_2, $Sm_{0.2}Ce_{0.8}O_2$, and BaO have been studied.[25–27] In the case of ceria related materials, a thin layer of ceria acts as a sulfur sorbent and prevents sulfur adsorption on the Ni surface through the formation of Ce_2O_2S. The BaO nanoparticles absorb water at the BaO/Ni interfaces and consequently promote sulfur removal from the surface of Ni. However, the thin layer of ceria and BaO nanoparticles are deposited randomly by a dip-coating method or multiple infiltrations. The random distribution can change the microstructure of Ni-YSZ and block the Ni-YSZ anode pores, resulting in modification of its catalytic property and mass flow limitation in the electrodes. There- fore, appropriate surface modification of the Ni-YSZ anode with a uniform catalyst coating on the anode surface is essential to obtain stable performance.

Recently, Liu *et al*. reported a multi-functional anode obtained from Ni-YSZ with $BaCO_3$ modification

in an anode supported cell.[28] The modification creates catalytically active BaO nanoparticles on the Ni surface and a conformal coating of $BaZr_{1-x}Y_xO_{3-\delta}$ (BZY) on the YSZ surface. BZY and BaO have high water adsorption ability, which plays an essential role in facilitating water-mediated carbon removal on the Ni surface. The multi-functional anode presented good electrochemical performance at 750 ^oC in iso-octane fuel. In addition, compared to infiltration or coating method of catalysts, this modification strategy is simple and cost effective because it does not require additional processing steps.

Here, we report an in-situ surface modification of Ni-YSZ with $BaZrO_3$ (BZO) via a small amount of $BaCO_3$ additive in a single step co-sintering process. BZO having high water uptake ability[29] placed Ni-YSZ grain boundaries, which was confirmed by scanning transmission electron microscopy (STEM). This *in-situ* surface modification results in high sulfur tolerance for a long period time compared with the unmodified Ni-YSZ anode

5.2 Experimental

NiO-YSZ-$BaZrO_3$ anode supported cell was fabricated by the following steps. The NiO-YSZ-$BaZrO_3$ cermet anode was prepared by a mixture of NiO, YSZ, corn starch, graphite, and $BaCO_3$ at a weight ratio of 16.5:13.5:3.3:2.1:1.5 via ball milling in ethanol for 24 h. After drying, the NiO-YSZ-$BaCO_3$ mixture was pressed into a pellet. To obtain a porous electrode, the pellet was sintered at 800 ^oC for 4 h in air. A thin NiO-YSZ active layer and a YSZ electrolyte were prepared by the refined particle suspension coating method. The NiO- YSZ and YSZ suspension were prepared by dispersing powder in ethanol with a small amount of binder (polyvinyl Butyral, B-98) and dispersant (triethanolamine, Alfa Aesar) at a ratio of 1:10, respectively. The NiO-YSZ and YSZ solution were sequentially deposited on the anode support by drop coating, followed by drying in air and then co-sintering at 1500 ^oC for 4h. A $La_{0.4}Ce_{0.6}O_{2-\delta}$ (LDC) buffer layer was deposited on the YSZ electrolyte. $La_{0.6}Sr_{0.4}Co_{0.2}Fe_{0.8}O_{3-\delta}$ (LSCF) cathode powders were prepared by the Pechini method and then the powders were mixed with V-006 and acetone to form a cathode slurry. The LSCF cathode was screen-printed on the LDC buffer layer, followed by sintering at 950 ^oC for 4h.

The phase identification of NiO-YSZ-BZO was confirmed by X-ray diffraction (XRD) patterns (Rigaku-diffractometer, Cu Kα radiation) in the 2 theta range of 20 ^{o} to 60 ^{o}. The microstructures and morphologies of the single cells were investigated using a field emission scanning electron microscope (SEM, Nova SEM). Transmission electron microscopy (TEM) images were obtained with a JEOL JEM 2100F with a probe forming Cs (spherical aberration) corrector operating at 200 kV. Cross-sectional samples for the TEM analysis were prepared by using a focused ion beam (FIB, Helios 450HP, FEI). Thermogravimetric analysis (TGA) was carried out by using a SDT-Q600 (TA Instruments, USA) at 700 ^oC.

For measuring the electrochemical performance of the single cell, NiO paste and Ag paste were used as

a current collector at the anode and cathode, respectively. The cells were mounted on an alumina tube with ceramic adhesive (Ceramabond 522, Aremco). Humidified H_2 (3% H_2O) and H_2S containing H_2 were applied to the anode as a fuel through a water bubbler with a flow rate of 100 mL min^{-1} and ambient air was applied to the cathode as an oxidant during cell tests. The cell performance was measured using a BioLogic Potentiostat, in potentiostatic mode.

5.3 Results and Discussions

The X-ray diffraction (XRD) patterns of NiO-YSZ-$BaCO_3$ sintered in air at 1500 °C for 4 h are presented in Figure 5.1a. It shows that NiO, YSZ, and $BaZrO_3$ (BZO) phases are detected as clear lines, interestingly indicating that BZO is formed in the NiO-YSZ anode. Figure 5.1b shows the XRD patterns of BZO modified Ni-YSZ after a sulfur stability test at 700 °C in 100 ppm H_2S containing H_2. It maintains crystallinity without any detectable impurity phases except that the NiO phase converted into a Ni metal phase due to the reducing atmosphere. From the XRD patterns, it is obvious that the BZO modified NiO-YSZ phase remains stable after high level sulfur poisoning.

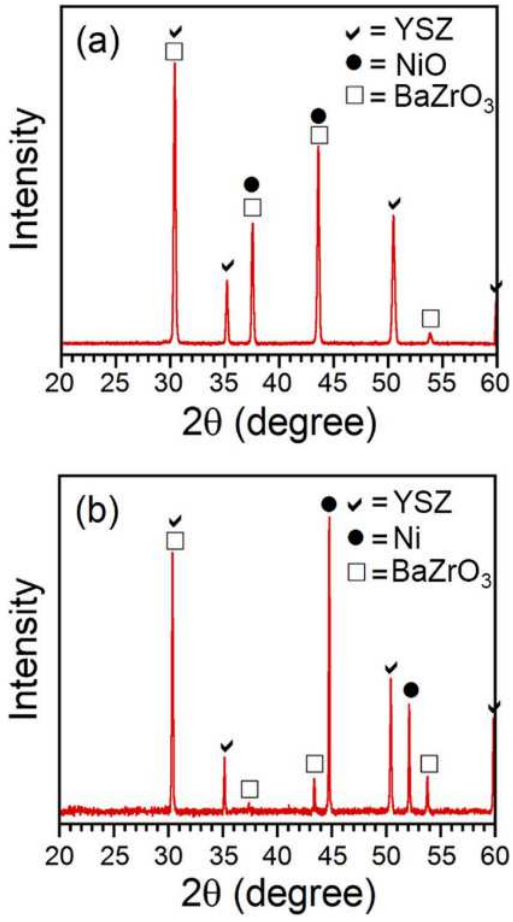

Figure 5.1. XRD patterns of NiO-YSZ with $BaCO_3$ cell (a) sintered at 1500 °C in air for 4 h, (b) after sulfur stability test at 700 °C in 100 ppm H_2S containing H_2.

The morphology of the BZO modified NiO-YSZ anode was investigated using a scanning electron microscope (SEM). Figure 5.2a shows a cross section SEM image of the NiO-YSZ-BZO/ NiO-YSZ/YSZ/LDC/LSCF anode supported cell. The SEM image displays good adhesion and continuous contact at the interfaces be- tween each element of the single cell. Figure 5.2b shows SEM image of the surface of the BZO modified NiO-YSZ anode. The YSZ forms grain boundaries and small particles of the BZO marked green are situated between the YSZ grains. Elements of the small particles of the BZO confirm mainly Ba, Zr and O, which is verified by an energy dispersive spectroscopy (EDS) point analysis (Figure 5.2c). It is also corresponded to the XRD results in Figure 5.1.

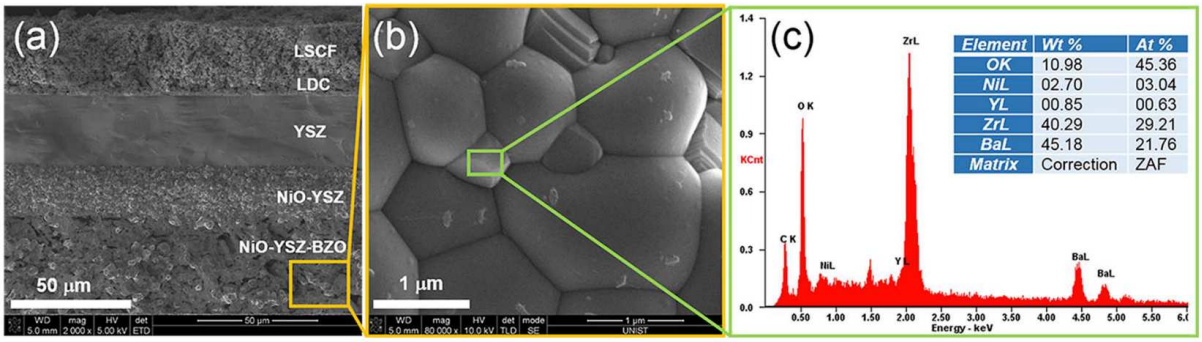

Figure 5.2. SEM images of (a) cross-section of the single cell, (b) surface of the BZO modified NiO-YSZ anode. (c) The point EDS spectrum of the BZO on the BZO modified NiO-YSZ surface.

To identify the configuration of the NiO-YSZ and BZO modified NiO-YSZ anodes sintered in air in detail, we fabricated a thin cross sectional sample of the anode using a focused ion beam (FIB). Figure 5.3 shows scanning transmission electron microscopy (STEM) images of the NiO-YSZ and the BZO modified NiO-YSZ anodes. Figures 5.3a, 3c and 3b, 3d present high-angle annular dark-field (HAADF) STEM images and corresponding energy dispersive spectroscopy (EDS) phase mapping images, respectively. Compared to unmodified NiO-YSZ, BZO modified NiO-YSZ has three phases such as NiO (green), YSZ (blue), and BZO (pink), which are contiguous with each other, as seen in the phase mapping image. In order to analyze the structure of the BZO, we magnified a small portion of the BZO grains (Figure 5.3e). A HAADF STEM image of BZO grain (Figure 5.3f) shows its atomic arrangement of conventional cubic perovskite viewed in the [001] direction. The interlayer d-spacing of (100) was measured as 0.42 nm, which is consistent with the theoretical value of BZO (JCPDS #06- 0399).[30] Based on the XRD and STEM, we confirm that the BZO is formed from NiO-YSZ with $BaCO_3$.

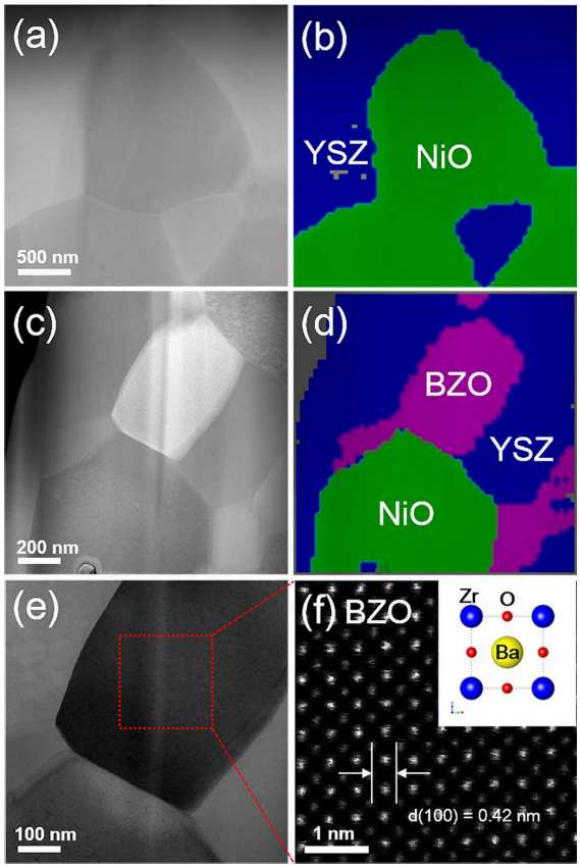

Figure 5.3. (a) High-angle annular dark-field (HAADF) STEM image and (b) EDS phase mapping image of NiO-YSZ. (c) HAADF STEM image and (d) EDS phase mapping image of BZO modified NiO-YSZ. (e) Bright-field (BF) STEM image of BZO modified NiO-YSZ. (f) HAADF STEM image of BZO and its atomic arrangement viewed along the [001] direction.

Figure 5.4 shows TEM images of the BZO modified Ni-YSZ anode after the sulfur stability test at 700 ^{o}C in 100 ppm H_2S containing H_2. Figure 5.4a and Figure 5.4b show a HADDF STEM image and a corresponding EDS phase mapping image of the cross-sectional anode sample, respectively. After the sulfur stability test, only the NiO phase converted into a Ni phase due to the reducing atmosphere, as shown in the phase mapping image. The BZO particles are contiguous with the YSZ grains and Ni metals, as seen in the bright-field TEM image (Figures 5.4b and 4c). Figure 5.4d shows a high-resolution TEM image of the BZO and the corresponding fast-Fourier transformed pattern with a zone axis of [001]. The interlayer distance of (100) plane had the same value of 0.42 nm as that of the sample before the sulfur stability test (Figure 5.3f), suggesting that the BZO has good chemical durability under a H_2 containing a high level of 100 ppm sulfur atmosphere.

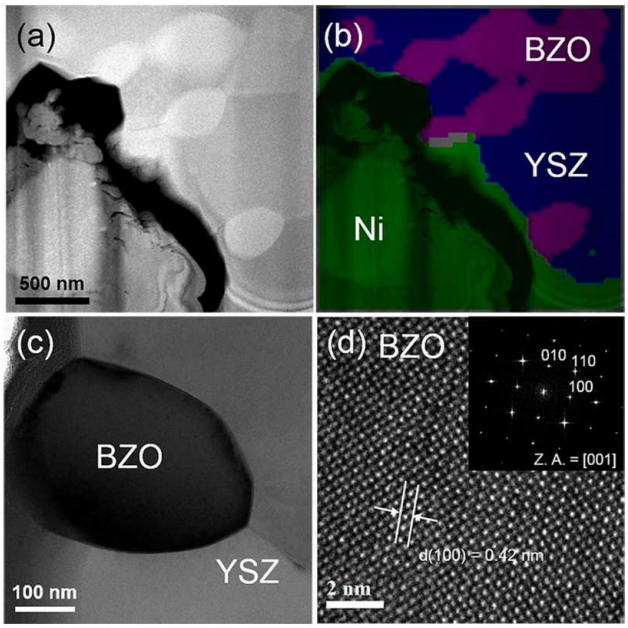

Figure 5.4. (a) HAADF STEM image and (b) EDS phase mapping image of BZO modified Ni-YSZ anode after the sulfur stability test at 700 ºC in 100 ppm H_2S containing H_2. (c) BFTEM image of BZO modified Ni-YSZ. (d) High-resolution (HR) TEM image and corresponding fast-Fourier transformed pattern of BZO grain with a zone axis [001].

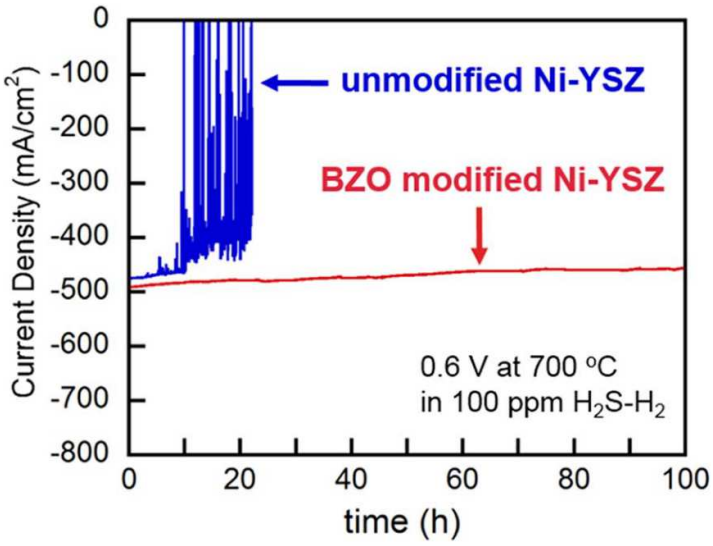

Figure 5.5. Electrochemical performance of unmodified Ni-YSZ anode and BZO modified Ni-YSZ anode in 100 ppm H_2S balanced with humidified (3% H_2O) H_2 at 700 ºC under a constant voltage of 0.6 V.

Figure 5.5 shows the electrochemical performance of unmodified Ni-YSZ and BZO modified Ni-YSZ anode supported cells in 100 ppm H_2S containing H_2 fuel at 700 ºC under a constant voltage of 0.6 V as a function of operating time (hours). The cell performance of the unmodified Ni-YSZ anode supported cell is degraded abruptly after around 8 h of 100 ppm sulfur contamination. The BZO modified Ni-YSZ anode supported cell, however, shows a stable performance in 100 ppm H_2S containing H_2 for more than 100 h. The enhanced sulfur tolerance in the BZO modified Ni-YSZ can be explained as follows.

Proton conducting materials have shown excellent sulfur tolerance because of their high water uptake ability.[11,17,25,31,32] For this reason, the BZO in Ni-YSZ can improve the sulfur tolerance of the conventional Ni-YSZ anode. Figure 5.6 presents thermogravimetric traces of BZO powder sample in dry and wet (3% H_2O) argon at 700 ºC. When the gas is changed from dry to wet atmosphere, an increase of weight is clearly observed for BZO powder sample, indicating that BZO has water uptake ability. Although the exact sulfur removal mechanism in BaO modified Ni-YSZ anode still remains uncertain, it has been hypothesized that the water adsorbed on BaO and $BaZrO_3$-$BaCeO_3$ surface oxidizes the sulfur contaminants, leading to stable operation of the fuel cell. In the resent thermodynamic studies on BaO modified Ni-YSZ, it is also suggested that sulfur could be first adsorbed on the BaO surface instead of Ni surface and then oxidized to SO_2.[25,33] Based on these hypothesis, sulfur tolerance of the BZO modified Ni-YSZ can be explained by following mechanisms in Figure 5.7. (a) In sulfur containing fuels, elemental sulfur adsorbs on the Ni surface, blocking electrochemical active sites. The adsorbed water on the BZO surface reacts with adsorbed elemental sulfur on the Ni surface to form SO_2 and H_2, which removes sulfur from the Ni surface and can be expressed as follows:

$$2H_2O(BZO) + S^*_{Ni} \rightarrow SO_2 + Ni + 2H_2 \quad [1]$$

where $H_2O(BZO)$ refers to adsorbed water on the BZO surface and S^*_{Ni} refers to sulfur adsorbs on the Ni surface. (b) In BZO (BaO-ZrO_2) modified anodes, the elemental sulfur first adsorbed on the BaO surface to form bulk sulfides (BaS) (Equation 2), which lowers the sulfur coverage on the Ni surface. The water adsorbed on the unreacted BZO (BaO-ZrO_2) surface ($OH_{(ads,unr.BaO)}$) reacts quickly with nearby bulk sulfides (BaS) to regenerate BaO (Equation 3).

$$BaO(BZO) + H_2S \leftrightarrow BaS + H_2O \quad [2]$$

$$BaS + 6OH_{(ads,unr.BaO)} \leftrightarrow 3H_2O + SO_2 + BaO_{(BZO)} \quad [3]$$

where $BaO_{(BZO)}$ refers to BaO terminated BZO surface and $OH_{(ads,unr.BaO)}$ refers to OH species adsorbed on the unreacted BaO-ZrO_2 (BZO) surface. These mechanisms and sulfur stability test results indicate

that the favorable high water uptake ability of BZO in Ni-YSZ results in significant enhancement of the electrochemical stability even with H_2 containing a high level of H_2S.

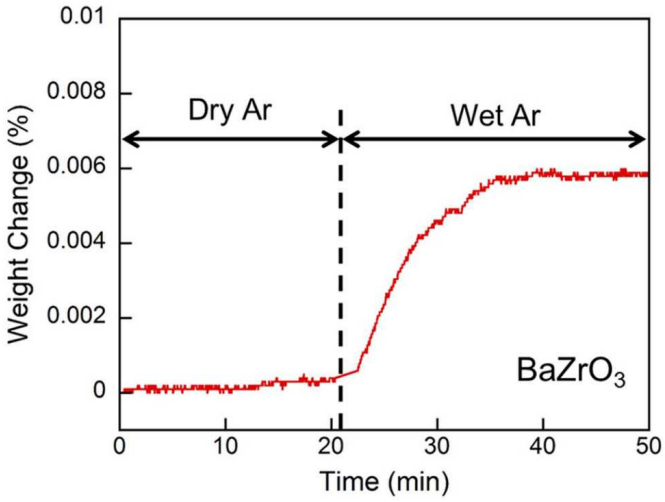

Figure 5.6. Typical thermogravimetric traces for BZO powder samples in dry and wet (3% H_2O) argon at 700 ^oC.

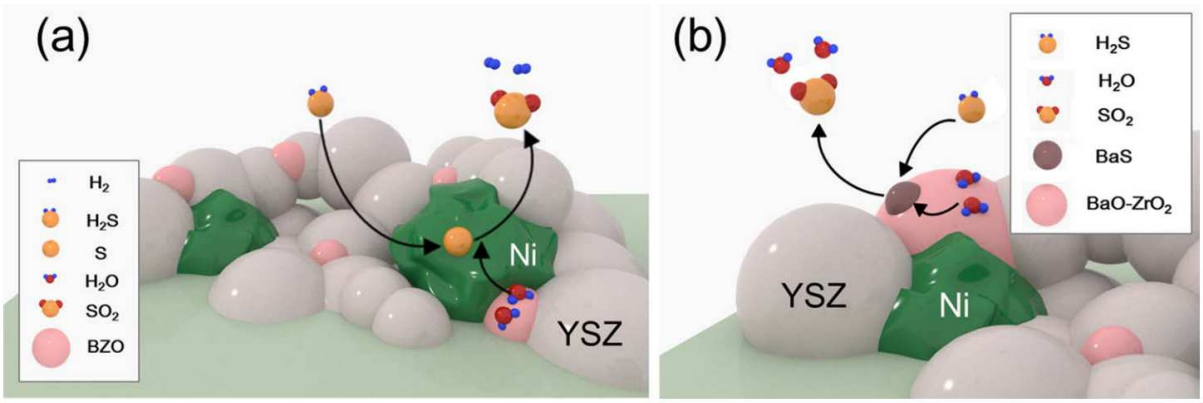

Figure 5.7. Schematic illustrations of the anodic reaction pathways according to (a) S adsorbed on Ni surface, and (b) S adsorbed on BZO surface for the BZO modified Ni-YSZ anode structure under sulfur contaminated H_2 fuel.

5.4 Conclusions

A $BaZrO_3$ (BZO) modified NiO-YSZ anode supported cell was fabricated through co-sintering of NiO, YSZ, and $BaCO_3$ at high temperature. The anode supported cell with the BZO modified Ni-YSZ anode shows remarkably stable performance over 100 h at 700 ^oC in humidified H_2 containing 100 ppm H_2S compared to conventional Ni- YSZ anode. Adsorbed water on the BZO surface removes adsorbed sulfur on the anode surface, leading to enhance sulfur tolerance of Ni-YSZ anode. Therefore, the BZO modified Ni-YSZ anode is a desirable candidate for stable operation in H_2 fuel containing a high level of H_2S.

References

1. P. Kowalik, K. Antoniak-Jurak, M. Błesznowski, M. C. Herrera, M. A. Larrubia, L. J. Alemany, and I. S. Pieta, *Catal. Today*, **254**, 129 (2015).

2. S. Sengodan, S. Choi, A. Jun, T. H. Shin, Y. W. Ju, H. Y. Jeong, J. Shin, J. T. S. Irvine, and G. Kim, *Nat. Mater.*, **14**, 205 (2015).

3. T. Nozaki, N. Muto, S. Kado, and K. Okazaki, *Catal. Today*, **89**, 57 (2004).

4. A. Das, Z. Han, W. W. Brennessel, P. L. Holland, and R. Eisenberg, *ACS Catal.*, **5**, 1397 (2015).

5. G. Chen, L. Chen, S.-M. Ng, and T.-C. Lau, *ChemSusChem.*, 7, 127 (2014).

6. J. Wu, A. Gross, and H. Yang, *Nano Lett.*, **11**, 798 (2011).

7. J. Zhao, A. Sarkar, and A. Manthiram, *Electrochim. Acta*, **55**, 1756 (2010).

8. V. Yordsri, W. Wongwiriyapan, and C. Thanachayanont, *Adv. Mater. Lett.*, **6**, 501 (2015).

9. J. P. Alper, M. S. Kim, M. Vincent, B. Hsia, V. Radmilovic, C. Carraro, and R. Maboudian, *J.Power Sources*, **230**, 298 (2013).

10. S. Park, J. M. Vohs, and R. J. Gorte, *Nature*, **404,** 265 (2000).

11. L. Yang, S. Wang, K. Blinn, M. Liu, Z. Liu, Z. Cheng, and M. Liu, *Science*, **326**, 126 (2009).

12. S. Yoo, A. Jun, Y. W. Ju, D. Odkhuu, J. Hyodo, H. Y. Jeong, N. Park, J. Shin, T. Ishihara, and G. Kim, *Angew. Chemie. Int. Ed.*, **53**, 13064 (2014).

13. A. Jun, J. Kim, J. Shin, and G. Kim, *ChemElectroChem.*, **3**, 511 (2016).

14. A. Jun, S. Yoo, Y. W. Ju, J. Hyodo, S. Choi, H. Y. Jeong, J. Shin, T. Ishihara, T. Lim, and G. Kim, *J. Mater. Chem. A*, **3**, 15082 (2015).

15. M. Liu, M. E. Lynch, K. Blinn, F. M. Alamgir, and Y. Choi, *Mater. Today*, **14**, 534 (2011).

16. A. Atkinson, S. Barnett, R. J. Gorte, J. T. S. Irvine, A. J. McEvoy, M. Mogensen, S. C. Singhal, and J. Vohs, *Nat. Mater.*, **3**, 17 (2014).

17. Z. Cheng, J.-H. Wang, Y. Choi, L. Yang, M. C. Lin, and M. Liu, *Energy Environ. Sci.*, **4**, 4380 (2011).

18. Z. Cheng and M. Liu, Solid State Ionics, 178, 925 (2007).

19. S. Zha, Z. Cheng, and M. Liu, *J. Electrochem. Soc.*, **154**, B201 (2007).

20. W. G. Bessler, M.Vogler, H. St¨ormer, D. Gerthsen, A. Utz,A.Weber, and E. I. -Tiffee, *Phys. Chem. Chem. Phys.*, **12**, 13888 (2010).

21. Y.-H. Huang, R. I. Dass, Z.-L. Xing, and J. B. Goodenough, *Science*, **312**, 254 (2006).

22. G. Corre, G. Kim, M. Cassidy, J. M. Vohs, R. J. Gorte, and J. T. S. Irvine, *Chem. Mater.*, **21**, 1077 (2009).

23. S. Sengodan, H. J. Yeo, J. Shin, and G. Kim, *J. Power Sources*, **196**, 3083 (2011).

24. S. Sengodan, J. S. Yoon, M. Y. Yoon, H. J. Hwang, J. Shin, and G. Kim, *ECS Electrochem. Lett.*, **2**, F45 (2013).

25. L. Liu, K. Sun, X. Zhou, X. Li, M. Zhang, and N. Zhang, *Electrochem. Commun.*, **19**, 63 (2012).

26. J. W. Yun, H. C. Ham, H. S. Kim, S. A. Song, S. W. Nam, and S. P. Yoon, *J. Electrochem. Soc.*, **160**, F153 (2013).

27. J. W. Yun, S. P. Yoon, J. Han, S. Park, H. S. Kim, and S. W. Nam, *J. Electrochem. Soc.*, **157**, B1825 (2010).

28. M. Liu, Y. Choi, L. Yang, K. Blinn, W. Qin, P. Liu, and M. Liu, *Nano Energy.*, **1**, 448 (2012).

29. K. D. Kreuer, Annu. Rev. Mater. Res., 33, 333 (2003). 30. H. Zhou, Y. Mao, and S. S. Wong, *J. Mater. Chem.*, **17**, 1707 (2007).

31. S. Sengodan, M. Liu, T. Lim, J. Shin, and G. Kim, *J. Electrochem. Soc.*, **161**, F668 (2014).

32. K. S. Blinn and M. Liu, J. Power Sources, 243, 24 (2013). 33. A. L. Silva and N. C. Heck, *Int. J. Hydrogen Energy*, **40**, 2334 (2015).

List of Publications

1. Donggue Lee,† Hansol Lee,† Ohhun Gwon, **Ohhun Kwon**, Hu Young Jeong, Guntae Kim,* and Sang-Young Lee*. Monolithic Heteronanomat Paper Air Cathodes Toward Origami-Foldable/Rechargeable Zn–Air Batteries. ***J. Mater. Chem. A.***, Just Accepted (2019)
2. Jeongwon Kim, Ohhun Gwon, **Ohhun Kwon**, Javeed Mahmood, Changmin Kim, Yejin Yang, Hansol Lee, Jong Hoon Lee, Hu Young Jeong, Jong-Beom Baek,* and Guntae Kim*. Synergistic Coupling Derived Cobalt Oxide with Nitrogenated Holey Two-Dimensional Matrix as an Efficient Bifunctional Catalyst for Metal-Air Batteries. ***ACS Nano***, 13, 5502-5512 (2019)
3. J. Kim, S. Sengodan, S. Kim, **O. Kwon**, Y. Bu, Guntae Kim*. Proton conducting oxides: A review of materials and applications for renewable energy conversion and storage. ***Renewable and Sustainable Energy Reviews.***, 109 , 606-618 (2019)
4. Nam Khen Oh,† Changmin Kim,† Jungyun Lee, **Ohhun Kwon**, Yunseong Choi, Gwan Yeong Jung, Hyeong Yong Lim, Sang Kyu Kwak,* Guntae Kim,* and Hyesung Park*. *In-situ* local phase-transitioned $MoSe_2$ in $La_{0.5}Sr_{0.5}CoO_{3-\delta}$ heterostructure and stable overall water electrolysis over 1000 hours. ***Nature Communications***, 10 , 1723 (2019)
5. Yunfei bu,† Seona Kim,† **Ohhun Kwon**, Qin Zhong, and Guntae Kim*. A Composite Catalyst Based on Perovskites for Overall Water Splitting in Alkaline Conditions. ***ChemElectroChem.***, 6 , 1520-1524 (2019)
6. Arunchander Asokan, Hansol Lee, Ohhun Gwon, Jeongwon Kim, **Ohhun Kwon**, and Guntae Kim*. Insight into the effect of nickel doping on ZIF-Derived oxygen reduction reaction catalysts for zinc-air batteries. ***ChemElectroChem.***, 6 , 1213-1224 (2019)
7. Sangwook Joo,† **Ohhun Kwon,†** Kyeounghak Kim, Seona Kim, Hyunmin Kim, Jeeyoung Shin, Hu Young Jeong, Sivaprakash Sengodan, Jeong Woo Han, and Guntae Kim. Cation-swapped homogeneous nanoparticles in perovskite oxides for high power density. ***Nature Communications.***, 697 (2019)
8. Donghwi Jeong, Junyoung Kim, **Ohhun Kwon**, Chaehyun Lim, Sivaprakash Sengodan*, Jeeyoung Shin,* and Guntae Kim*. Scandium Doping Effect on a Layered Perovskite Cathode for Low-Temperature Solid Oxide Fuel Cells (LT-SOFCs). ***Applied Science.***, 8, 2217 (2018)
9. Changmin Kim,† Seona Kim,† **Ohhun Kwon**, Jeongwon Kim, and Guntae Kim*. Polypyrrole-assisted Co_3O_4 anchored carbon fiber as a binder-free electrode for seawater batteries. ***ChemElectroChem.***, 5,1-6 (2018)
10. **Ohhun Kwon**, Kyeounghak Kim, Sangwook Joo, Hu Young Jeong, Jeeyoung Shin, Jeong Woo Han, Sivaprakash Sengodan* and Guntae Kim*. Self-assembled alloy nanoparticles in a layered double perovskite as a fuel oxidation catalyst for solid oxide fuel cells. ***Journal of Materials Chemistry A.***, 6, 15947 (2018)

11. Seona Kim, **Ohhun Kwon**, Changmin Kim, Ohhun Gwon, Hu Young Jeong, Ka-Hyun Kim*, Jeeyoung Shin*, and Guntae Kim*. Strategy for Enhancing Interfacial Effect of Bifunctional Electrocatalyst: Infiltration of Cobalt Nano Oxide on Perovskite. ***Adv. Mater. Interfaces.***, 5, 1800123 (2018)
12. Sivaprakash Sengodan, Young-Wan Ju, **Ohhun Kwon**, Areum Jun, Hu Young Jeong, Tatsumi Ishihara, Jeeyoung Shin*, and Guntae Kim*. Self-Decorated MnO Nanoparticles on Double Perovskite Solid Oxide Fuel Cell Anode by *in Situ* Exsolution. ***ACS Sustainable Chem. Eng.***, 5, 9207-9213 (2017)
13. **Ohhun Kwon**, Sivaprakash Sengodan, Kyeounghak Kim, Gihyeon Kim, Hu Young Jeong, Jeeyoung Shin, Young-Wan Ju, Jeong Woo Han, and Guntae Kim*. Exsolution trends and co-segregation aspects of self-grown catalyst nanoparticles in perovskites. ***Nature Communications.***, 8 , 15967 (2017)
14. **Ohhun Kwon**, Sivaprakash Sengodan, Chaehyun Lim, Hu Young Jeong, Jeeyoung Shin, Young-Wan Ju*, and Guntae Kim*. *In Situ* Surface Modification of Ni-YSZ with $BaZrO_3$ for Enhancing the Sulfur Tolerance of Ni-YSZ Anode. ***J. Electrochem. Soc.***, 163, F1055-F1058 (2016)
15. Ohhun Gwon, Changmin Kim, **Ohhun Kwon**, Hu Young Jeong, Heai-Ku Park, Jeeyoung Shin, Young-Wan Ju*, and Guntae Kim*. An Efficient Oxygen Evolution Catalyst for Hybrid Lithium Air Batteries: Almond Stick Type Composite of Perovskite and Cobalt Oxide. ***J. Electrochem. Soc.***, 163, A1893-A1897 (2016)
16. Seona Kim, Areum Jun, **Ohhun Kwon**, Junyoung Kim, Seonyoung Yoo, Hu Young Jeong, Jeeyoung Shin*, and Guntae Kim*. Nanostructured Double Perovskite Cathode With Low Sintering Temperature For Intermediate Temperature Solid Oxide Fuel Cells. ***ChemSusChem.***, 8, 3153-3158 (2015)

Acknowledgement

Completion of this doctoral dissertation was possible with the support of many people. I would like to express my sincere gratitude to all of them.

First of all, I would like to express my gratitude to my advisor, Prof. Guntae Kim, for giving me the opportunity to generous support and guidance for my research work. Without his assistance, this dissertation would not have had the present consecution and quality.

I would also like to appreciate my committee members, Prof. Sang-Young Lee, Prof. Jong-Beom Back, Prof. Hu Young Jeong, and Prof. Jeong Woo Han for their thoughtful insight, encouragement, and valuable time. I was inspired by their valuable advice on the direction and attitude for future research.

Especially, I am sincerely grateful to my great co-advisor, Prof. Hu Young Jeong. He has always provided in-depth and valuable inspiration for my doctoral research. And he has shown me, by his example, what a good scientist (and person) should be.

I also thanks to our group members of "**gunslab**", who helped me during the course of doctoral study: Prof. Sivaprakash Sengodan, Dr. Seonyoung Yoo, Prof. Sihyuk Choi, Dr. Areum Jun, Dr. Junyoung Kim, Dr. Ohhun Gwon, Dr. Seona Kim, Changmin Kim, Chaehyun Lim, Donghwi Jeong, Sangwook Joo, Gihyeon Kim, Jeongwon Kim, Seungtae Lee, Hyunmin Kim, Hansol Lee, Arim Seong, Yejin Yang, Hyojae Hwang, Prof. Jeeyoung Shin, Prof. Young-Wan Ju, Prof. Yunfei Bu, and Dr. Arunchander Asokan. In particular, I would like to thank Prof. Sivaprakash Sengodan and Dr. Junyoung Kim for their advice on designing my doctoral study. Studying for years would have been impossible without them. I wish you all the best for your work and would always be happy to hear good news.

Last but not least, I would like to appreciate my parents, my brother, and all of my family for their endless love, encouragement, and support.